UNIVERSITA' DEGLI STUDI DI PARMA

Dottorato di Ricerca in Ingegneria Geotecnica

Ciclo XXIV

Numerical modelling of electrokinetic processes on a natural soil

Coordinatore

Prof. Alberto Mazzucato

Tutors

Prof. Francesco Colleselli

Prof. Cristina Jommi

Dottorando

Fabio Cattaneo

Gennaio 2012

Fabio Cattaneo
Numerical modelling of electrokinetic processes on a natural soil

e-mail:
fcattaneo@stru.polimi.it

Abstract

A numerical study on modelling electrokinetic processes occurring in a natural soil is presented.

Two numerical procedures preparatory to the study by means of the well-known finite element method are presented. The first procedure is intended to integrate constitutive laws along typical unsaturated testing path. The second procedure is devoted to analyse the most relevant chemical reactions occurring in a soil under an electric field.

Selected results of previous experimental studies are theoretically analysed to define a suitable interpretation framework. Afterwards that an elasto-plastic constitutive model with generalised hardening is proposed. Finally electrokinetic filtration tests are simulated by means of a finite element model.

Sommario

Viene presentato uno studio numerico per la modellazione dei fenomeni elettrocinetici in un terreno naturale.

Vengono proposte due procedure numeriche propedeutiche allo studio mediante il ben noto metodo degli elementi finiti. Una prima procedura permette l'integrazione dei legami costitutivi per la simulazione delle prove geotecniche di laboratorio in campo non saturo. La seconda procedura è volta alla definizione delle reazioni chimiche che avvengono a seguito dell'applicazione di un campo elettrico nei terreni.

I risultati ottenuti da precedenti studi sperimentali sono prima interpretati teoricamente. Viene poi proposto un modello costitutivo elasto-plastico per l'interpretazione delle prove meccaniche. Infine le prove di filtrazione elettrocinetica sono simulate attraverso il metodo degli elementi finiti.

Contents

List of Figures

List of Tables

List of symbols

A_i	$[-]$	chemical activity of the i-th chemical specie
c_i	$[nl^{-3}]$	concentration of the i-th chemical specie
$\bar{c}_i$	$[nl^{-3}]$	concentration of the i-th mineral chemical specie
c_p	[]	specific heat capacity
$\mathbf{D}^{el}$	[]	elasticity stiffness
D_i	$[l^2t^{-1}]$	diffusion coefficient at free solution of the i-th chemical specie
$\mathbf{D}_i^*$	$[l^2t^{-1}]$	effective diffusion coefficient of the i-th chemical specie
e	$[-]$	void ratio
f_i	$[-]$	mass fraction of the i-th chemical specie
F	$[n]$	Faraday constant
g	$[lt^{-2}]$	gravity
$\mathbf{j}$	$[t^{-1}]$	electric current
$\mathbf{J}_i$	$[nt^{-1}]$	flow of the i-th chemical specie
$\mathbf{J}_i^d$	$[nt^{-1}]$	diffusional flux of the i-th chemical specie
$\mathbf{J}_i^e$	$[nt^{-1}]$	migrational flux of the i-th chemical specie
$\mathbf{J}_i^l$	$[nt^{-1}]$	advective flux of the i-th chemical specie
$\mathbf{J}_T$	[]	heat flux
k_e	$[lt^{-1}V^{-1}]$	electroosmotic coefficient
k_e^{rel}	$[-]$	relative electroosmotic coefficient
k_g^{rel}	$[-]$	relative permeability of the gas phase
k_l^{rel}	$[-]$	relative permeability of the liquid phase
m_i^{mol}	$[Mn^{-1}]$	molar mass of the i-th chemical species
m_w	$[M]$	mass of water
m_w^g	$[M]$	mass of water in the gas phase
m_w^l	$[M]$	mass of water in the liquid phase
n	$[-]$	porosity
p_{atm}	$[Fl^{-2}]$	atmospheric pressure
$\mathbf{q}$	$[-]$	vector of internal variables
Q	[]	soil capacity

Q_{gen}	[]	heat generation
R	$[\mathrm{m}FT^{-1}n^{-1}]$	universal gas constant
R_i	$[nl^{-3}t^{-1}]$	molar production rate of the i-th chemical species
R_r^s	$[nl^{-3}t^{-1}]$	sorption reactions rate
R_r^{aq}	$[nl^{-3}t^{-1}]$	aqueous phase reactions rate
R_r^{pd}	$[nl^{-3}t^{-1}]$	precipitation/dissolution reactions rate
s	$[Fl^{-2}]$	suction
Sr	$[-]$	degree of saturation
t	$[t]$	time
T	$[T]$	absolute temperature
$\mathbf{u}$	$[l]$	displacement vector
u_g	$[Fl^{-2}]$	gas pressure
u_g^0	$[Fl^{-2}]$	gas pressure at reference state
u_l	$[Fl^{-2}]$	liquid pressure
$\mathbf{v}_g$	$[lt^{-1}]$	gas phase seepage velocity
$\mathbf{v}_l$	$[lt^{-1}]$	liquid phase seepage velocity
$\mathbf{v}_l^e$	$[lt^{-1}]$	seepage velocity due to electroosmosis
$\mathbf{v}_l^h$	$[lt^{-1}]$	seepage velocity due to Darcy law
z_i	$[-]$	charge of the i-th chemical specie
$\boldsymbol{\delta}$	$[-]$	Kronecker delta
$\boldsymbol{\delta}_{zx}$	$[-]$	direction of the gravity
$\boldsymbol{\varepsilon}$	$[-]$	small strain tensor
$\boldsymbol{\varepsilon}^e$	$[-]$	elastic strain tensor
$\boldsymbol{\varepsilon}^p$	$[-]$	plastic strain tensor
$\boldsymbol{\kappa}$	$[l^2]$	absolute permeability tensor
μ_g	$[Fl^{-2}t]$	gas dynamic viscosity
μ_i	$[l^2t^{-1}V^{-1}]$	ionic mobility of the i-th chemical specie
μ_i^*	$[l^2t^{-1}V^{-1}]$	effective ionic mobility of the i-th chemical specie
μ_l	$[Fl^{-2}t]$	liquid dynamic viscosity
μ_w	$[Fl^{-2}t]$	water dynamic viscosity
ν_{ri}	$[-]$	stechiometric coefficient of the i-th species in teh reaction r
ρ_g	$[Ml^{-3}]$	gas density
ρ_g^0	$[Ml^{-3}]$	gas density at reference state

ρ_l	$[Ml^{-3}]$	liquid density
ρ_s	$[Ml^{-3}]$	density of the solid phase
ρ_w	$[Ml^{-3}]$	water density
$\boldsymbol{\sigma}$	$[Fl^{-2}]$	total stress tensor
$\hat{\boldsymbol{\sigma}}$	$[Fl^{-2}]$	average soil skeleton stress tensor
σ_f	$[\rho]$	electrical conductivity of the pore fluid
σ_s	$[\rho]$	electrical conductivity of the solid particles
σ^*	$[\rho]$	effective electric soil conductivity
$\boldsymbol{\tau}$	$[-]$	tortuosity
Φ	$[V]$	electric potential

1 Introduction

Today waste management and land remediation are becoming fundamental issues. Every year, millions of tonnes of hazardous waste are generated in the world. In recent year waste management focused on reducing the generated waste, not only on handling it. However due to inefficient waste handling techniques and hazardous waste leakage in the past, thousands of sites were contaminated by heavy metals, organic compounds and other hazardous materials (Virkutyte et al., 2002).

Soil remediation and contaminant containment have a definite impact on the quality of groundwater and on the land reuse. Several remediation and containment technologies were proposed in the past. The different technologies can be classified in different ways (see Tab. 1.1 from Shackelford and Jefferis, 2000): according to the location of the remediation process (ex-situ versus in-situ), to the objective of the technology (containment versus treatment) or to the process involved in the technology (i.e., chemical, physical, biological, or thermal). Clearly the widespread types of contaminants and the heterogeneity of soil deposits is such that each proposed technology has an application range (i.e. it deal with some kind of contaminants and site conditions) and an all-purpose technology does not exist.

Table 1.1: Classification of remediation technologies based on soil as the contaminated medium (from Shackelford and Jefferis, 2000).

Soil Removal?	Technology category	Technique Process	Example(s)	Comment(s)
Yes (*ex-situ*)	Containment	Disposal	Landfills	On-site vs. Off-site; New vs. Existing
	Treatment	Chemical	Neutralisation, Solvent extraction	Treated soil may require disposal in a landfill, or may be returned to the site
		Physical	Soil washing, Stabilisation/Solidification, Vitrification	
		Biological	Biopiles, Bioreactors	
		Thermal	Incineration, Vitrification	
No (*in-situ*)	Containment	Pump & Treat	Vertical wells, Horizontal wells	Both passive and active containment are possible. In pump & treat, pumping is used to control hydraulic gradient and collect contaminated water. Treatment is *ex-situ*
		Capping	Traditional covers, Alternative covers, Geochemical covers	
		Vertical barriers	Slurry walls, Grout curtains, Sheet piling, Biobarriers, Reactive barriers	
		Horizontal Barriers	Grout injected liners	
	Treatment	Chemical	Oxidation, Chemical reduction	Technologies indicated with (*) require removal of gas and/or liquid phases and *ex-situ* treatment; both passive and active treatment are possible
		Physical	Soil flushing*, Stabilisation/solidification, Vitrification, Air sparging (AS)*, Soil vapour extraction (SVE)*, Electrokinetics (EK)*	
		Biological	Monitored natural attenuation (MNA), Bioventing, Bioslurping, Biosparging	
		Thermal	Steam injection*, Radio frequency heating (RF)*, vitrification*	

The absence of a leading technology has increased the interest in finding new and innovative techniques for the efficient removal of contaminants from soils (Shackelford and Jefferis, 2000). The demand for innovative and cost effective in-situ remediation technologies stimulated the effort to employ conduction phenomena in soils under electrical field as a remediation technique (Acar and Alshawabkeh, 1993; Lageman et al., 1989a; Pamukcu and Wittle, 1992; Shapiro and Probstein, 1993). Electrokinetic remediation techniques are based on the transport of fluid and mass by two main processes: electroosmosis and electromigration. The former is the movement of the pore fluid as a result of an applied electric potential gradient while the latter is the migration of free ionic species towards the electrode of opposite charge. This technologies has shown to be particularly effective for remediation of fine grained soil, which are characterised by low hydraulic conductivity and electrically charged particles.

1.1 Scope

The present work deals with numerical modelling of electrokinetic processes. Bear and Cheng (2010) define a model as a *selected simplified version of a real system and phenomena that take place within it, which approximately simulates the system's excitation-response relationships that are of interest.* Models play an essential role to support decisions required in the remediation process.

A systematic approach for the assessment and remediation of a contaminant site is usually adopted (Reddy et al., 1999). Figure 1.1 outlines the steps of this approach. The most important aspects of the remediation process are: (1) site characterisation, (2) risk assessment, (3) selection and implementation of a remedial action. The risk assessment stage indicates the level of the risk to human health and environment. Sometimes the natural attenuation process could be sufficient to reduce contaminant and, in this case, the site should be monitored. To support this decision a model of the diffusion of the contaminant in the groundwater is required.

If a risk to human health and environment is present and the natural attenuation process is not sufficient to reduce it, a remedial action must be implemented. Figure 1.1 shows that the remediation process is an iterative process. In particular the choice between different remediation techniques has to be performed. Besides

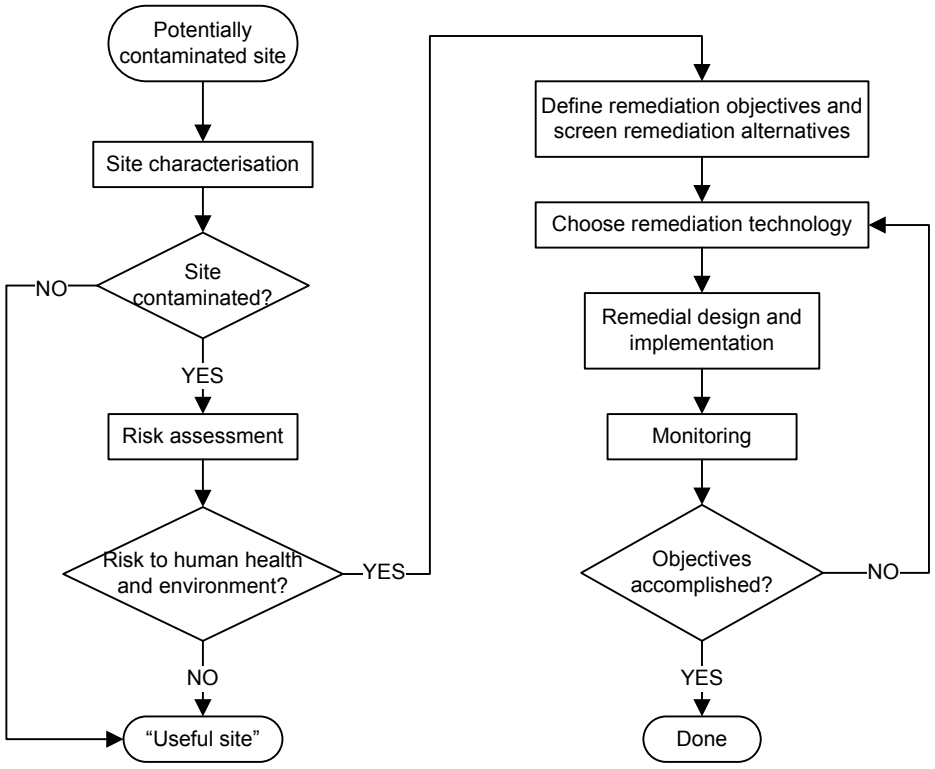

Figure 1.1: Flow chart of remediation process (after Reddy et al., 1999; Shackelford and Jefferis, 2000).

laboratory tests, the evaluation of the effectiveness of a remediation technology could be predicted by numerical models. Numerical models could also helps in the best design for the chosen remediation technology.

The present work is part of a larger study within the PRIN 2006080119-2006 *Studio sperimentale e teorico della applicabilità di processi elettrocinetici per il controllo della propagazione degli inquinanti nei terreni a grana fine* developed by Universities of Perugia, Palermo, Brescia and by Politecnico di Milano. This research project concerns

1. the determination of the electrical conductivity and the electroosmotic permeability of saturated and unsaturated soils by means of laboratory tests;

2. the experimental characterisation of the saturated and unsaturated hydrome-

chanical behaviour of natural and compacted soils suitable for electrokinetic applications;

3. the experimental effects of prolonged electrokinetic treatment on the soil microstructure;

4. the development of a mathematical model of the coupled hydraulic, ionic and electric flow processes;

5. constitutive modelling, within generalised plasticity, of clays suitable for electrokinetic barrier;

6. the numerical implementation, by means of the finite element method, of the mathematical model;

7. the development of a laboratory pilot test in order to validate the theoretical/numerical models.

In particular this work deals with points 4, 5 and 6.

1.2 Organisation of the manuscript

The thesis is divided in eight chapters, whose order is intended to follow the conceptual sequence of the study.

After the first introductive Chapter, Chapter Two concerns electrokinetic phenomena in soils and the principles at the bases of the use of electrokinetics in geotechnical engineering. Also the applications of electrokinetic phenomena in soil mechanics and in environmental geotechnics are presented.

Chapter Three deals with the theoretical development and mathematical formulation of the electrokinetic processes. The coupled flows of fluid, mass, and charge under hydraulic, electric, and chemical concentration gradients are discussed as well as the associated principles of conservation of matter and energy together with the chemical reactions that take place. Since the possible unsaturated state has to be take into account, also the water retention curve is introduced. Finally, the behaviour of the solid skeleton is described.

Chapter Four presents the numerical algorithm to integrate elasto-plastic constitutive laws along typical loading path. The proposed algorithm allows for developing numerical integration routines for the constitutive equations, ready for their straightforward implementation in finite element codes. The most common algorithm used for the integration of constitutive equations are also described.

Chapter Five present a numerical algorithm to integrate chemical reactions at the point volume element. The proposed algorithm allows a first analysis of the chemical reactions involved in the process.

In Chapter Six the available experimental results performed within the PRIN research project are shown. Both mechanical and electrokinetic filtration tests were performed and their results are modelled with the algorithms presented in Chapter Four and Five, respectively. A constitutive model able to reproduce the mechanical behaviour is also described.

In Chapter Seven the electrokinetic tests were modelled using the finite element method and comparison between the experimental and numerical results is performed.

2

Electrokinetics in Geotechnical engineering

The investigation of electroosmosis in soil was started by Reuss (1809). He took two electrodes and put each in a glass tube. The glass tubes were inserted into a saturated clay soil sample, the upper face of which was covered with wax to avoid drainage. Applying a constant electric potential difference between the electrodes Reuss observed a fluid flow towards the cathode. After Reuss, some theoretical studies on electroosmosis were performed in the nineteenth century, but electroosmosis was not applied in engineering until 1930's, when Leo Casagrande started his studies.

The first engineering application of electroosmosis, due to Casagrande's research, was consolidation of soft clays. In the consolidation process, water flows reducing its pore pressure and increasing the effective stress. Electroosmotic flow increases water flow, allowing a faster consolidation process, or inducing it. Starting from Casagrande's studies several theoretical and laboratory studies have been performed on the application of an electric field to improve the mechanical characteristic of soils (e.g. Esrig, 1968; Morris et al., 1985; Wan and Mitchell, 1976).

In the 1980's the studies on electrokinetics shifted to its use in the field of waste management. In particular the use of electrokinetic processes for soil remediation and of electrokinetic barrier to prevent contaminant migration were proposed (Acar

and Alshawabkeh, 1993; Lageman et al., 1989a). Laboratory studies have shown that electrokinetic treatments are successfully in clayey or silty soils for organic and metal contaminants (e.g. Acar and Alshawabkeh, 1996; Hansen et al., 1997; Kim et al., 2000; Li et al., 2000; Mascia et al., 2007). Few field pilot test have been performed showing that electrokinetics is particularly effective in removing metal contaminant (Gent et al., 2004; Ho et al., 1999a,b; Lageman, 1993; Wieczorek et al., 2005).

Electrokinetic processes were also applied to dewater waste sludge (Buijs et al., 1994; Raats et al., 2002; Yuan and Weng, 2003) or to prepare hollow shape clay sample (Talesnick and Frydman, 1990).

In this chapter the aspects related to the application of electrokinetic in soil will be discussed. The aim of this chapter is not to provide a complete review of electrokinetics in soils, but only to recall the main aspects to be reproduced in numerical analysis.

2.1 Electrokinetic in soil

Electrokinetic applications in soil use a low level direct current, of the order of magnitude of mA/cm^2 of soil cross-sectional area, or an electric potential difference of the order of magnitude of V/cm (Acar and Alshawabkeh, 1993). The applied electric field leads to coupled transport phenomena, electrolysis reactions at the electrodes, chemical species migration, adsorption/desorption of chemical species and precipitation/dissolution reactions. In the subsequent sections all these aspects will be discussed.

2.1.1 Electrokinetic phenomena

In soil mechanics soils are traditionally classified by the size of the constituent particles. Gravel, sand, and most of the silty fraction in a soil are composed of bulky, nonclay particles. Clay minerals are formed by sheet of silica and alumina. Different clay minerals (smectite, illite, kaolinite, ...) are characterised by the stacking arrangements of sheets to form layers and the manner in which layers are held together. The presence in the crystal structure of cations other than

that normally found is called isomorphous substitution (Mitchell and Soga, 2005). Isomorphous substitution is the main reason of the negative charge on the surface of clay particles.

In materials such as fine grained soils, where there are charged particles, coupling between electrical and hydraulic flows and gradients can generate four related *electrokinetic phenomena*, listed in Table 2.1 and shown in Figure 2.1. These phe-

Table 2.1: Summary of electrokinetic phenomena.

Phenomena	Electric potential	Liquid phase	Solid Phase
Electroosmosis	applied	flow induced	fixed
Electrophoresis	applied	no flow	movement induced
Streaming Potential	induced	flow applied	fixed
Sedimentation Potential	induced	no flow	movement applied

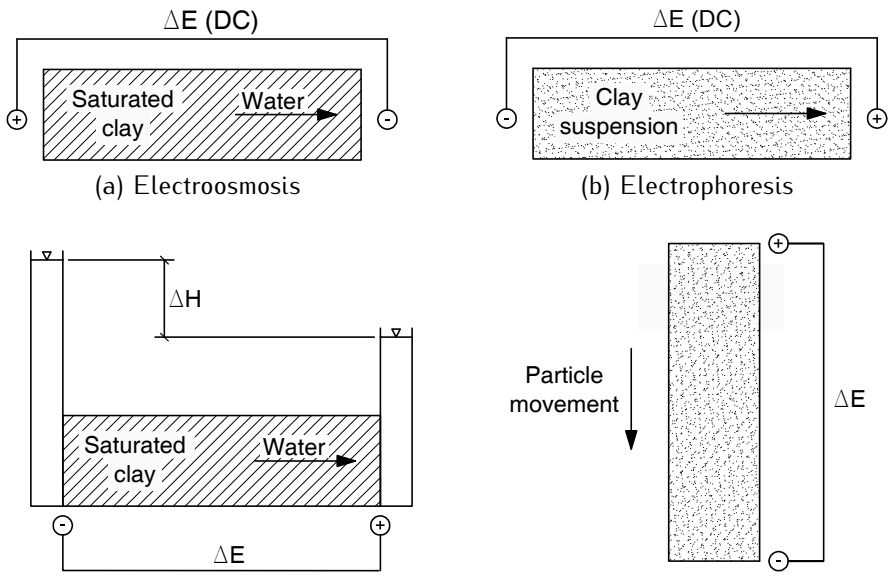

(a) Electroosmosis (b) Electrophoresis

(c) Streaming potential (d) Sedimentation potential

Figure 2.1: Electrokinetic phenomena.

nomena could be classified into two groups by the driving forces (Yeung, 1994). The first group consists of electroosmosis and electrophoresis, in which the liquid phase and the solid phase move relative to the other under the influence of an externally

applied electrical potential. The other group consists of streaming potential and sedimentation potential, in which the relative movement of the liquid or the solid phase to the other induces an electrical potential.

Of the four electrokinetic phenomena the most studied and applied in geotechnical engineering is electroosmosis because of its practical value for transporting water in fine-grained soils. The applications of electrokinetic in soils are described in later sections.

Electroosmosis

Electroosmosis is the movement of a liquid phase relative to a solid phase under the influence of an imposed electric gradient. Because of the imposed electric gradient the ions in the pore fluid are attracted to the electrodes: cations towards the cathode and anions towards the anode. As ion migrate, they carry their water of hydration and exert a viscous drag on the water around them (Mitchell and Soga, 2005). As explained before clay particles are negatively charged, thus there are more cations than anions in the pore fluid, resulting in a water flow toward the cathode.

Several theories have been proposed to explain electroosmosis. Among the others, the model developed by Helmholtz (1879) and refined by Smoluchowski (1914) is one of the earliest, but it is still widely used today. The simplifying assumption of soil pores as capillary tubes is introduced. The capillary is treated as an electrical condenser with charges of one sign on or near the surface of the wall and countercharges concentrated in a layer in the liquid a small distance from the wall (Fig. 2.2). Under these assumptions the Helmholtz-Smoluchowski theory gives an expression of the flow velocity v in the form:

$$v = \left(\frac{\xi D}{\eta} \right) \frac{\Delta E}{\Delta L} , \tag{2.1}$$

where ξ is called *zeta potential*, D and η are the dielectric constant and the viscosity of the pore fluid, respectively.

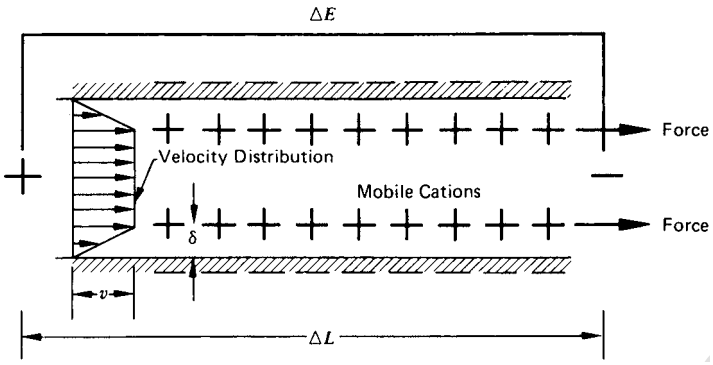

Figure 2.2: Helmholtz-Smoluchowski model for electroosmosis (Mitchell and Soga, 2005).

Electrophoresis

Electrophoresis is the transport of charged particles suspended in a stationary liquid under an electric field. When an electric current is applied to a colloidal suspension, charged particle are attracted to one of the electrodes and repelled from the other. The negatively charged particles will move to the anode while the positively charged particles will move to the cathode.

Streaming potential

Streaming potential is the reciprocal electrokinetic phenomenon of electroosmosis. When a liquid is forced through a porous medium by a hydraulic gradient, an electrical potential difference, called streaming potential, is generated between the opposite ends of the porous medium. Streaming potential is caused by the presence of the double layer, which charges displaces in the direction of the imposed flow. This generates an electrical potential difference that is proportional to the hydraulic flow rate. Streaming potentials up to several tens of millivolts were observed in clays (Mitchell and Soga, 2005).

Sedimentation potential

Sedimentation potential is the reciprocal electrokinetic phenomenon of electrophoresis. The movement of colloidal charged particles in a stationary liquid, as

during gravitational settling, generates an electrical potential difference between the boundaries of the liquid phase. This electrical potential difference is called sedimentation potential and the phenomenon is sometimes known as the Dorn effects. Sedimentation potential is caused by the viscous drag of the liquid phase that retards the movement of the diffuse layer cations relative to the particles.

2.1.2 Electrolysis

Application of electric current through electrodes immersed in water induces the following electrolysis reactions in the immediate vicinity of the electrodes:

$$2\,H_2O_{(l)} - 4\,e^- \longrightarrow O_{2\,(g)} + 4\,H^+ \qquad E^0 = +1.229 \qquad \text{(anode)} \tag{2.2a}$$

$$2\,H_2O_{(l)} + 2\,e^- \longrightarrow 2\,H_{2\,(g)} + 2\,OH^- \qquad E^0 = -0.8277 \qquad \text{(cathode)}\,, \tag{2.2b}$$

where E^0 is the standard reduction electrochemical potential, which is a measure of the tendency of a chemical species to aquire electrons and thereby be reduced. At the electrodes secondary redox reactions may exist depending on their electrochemical potential and on the concentration of available species. For example secondary reactions could involve metals:

$$M^{n+} + ne^- \longrightarrow M \tag{2.3a}$$

$$M(OH)_{n(s)} + ne^- \longrightarrow M + OH^-\,, \tag{2.3b}$$

where M refers to metals.

Water electrolysis decreases the pH at the anode,

$$pH = -\log c_{H^+}\,, \tag{2.4}$$

while at the cathode, according to the water auto ionisation reaction,

$$H_2O \rightleftharpoons H^+ + OH^- \qquad K_w = [H^+][OH^-] \cong 10^{-14}\,, \tag{2.5}$$

the pH increases.

The hydrogen ions produced at the anode migrate towards the cathode. The

transport process of a ion is governed by diffusion, due to concentration gradient, by advective pore fluid flow, due to electroosmosis and to hydraulic head gradient, and by electromigration, due to electrical gradient. The diffusion coefficient, which defines diffusion, and the ionic mobility, which defines the electromigration, of the hydrogen and hydroxyl ions are higher than those of the other ions because hydrogen and hydroxyl ions dissociates and associates rapidly with the water molecules. As a consequence hydrogen and hydroxyl ions controls the chemistry across the soil mass (Acar and Alshawabkeh, 1993). Migration of the hydrogen ions develops an acid front. At the opposite the hydroxyl ions, which are negative charged, develop an alkaline front from the cathode towards the anode. Advance of the acid front is faster than the advance of the base front because:

- the electroosmotic flow direction is opposed to the advancing direction of the base front while it has the same direction of the acid front;
- the diffusion coefficient and the ionic mobility of the hydrogen ion are about 1.76 higher than those of the hydroxil ion.

As a consequence the acid front dominates the chemistry across the soil mass. On the other hand, the buffering capacity of the soil may decrease the water pH. Therefore the effective advance of the acid front is the result of the interaction between the pore water chemistry and the soil buffering capacity.

2.1.3 Effects on metallic contaminant

Changes in the pH affect overall chemical equilibriums present in the soils. In particular the low-pH environment resulting from the acid front inhibits the soil particles capacity to sorb metallic contaminants. Thus a low-pH favours the formation of soluble compounds.

The dissolution/precipitation equilibrium of a metal hydroxide is

$$M(OH)_{n(s)} \longleftrightarrow M^{n+} + nOH^{-} \qquad K_p = [M^{n+}][OH^{-}]^n \,, \tag{2.6}$$

where K_p is the solubility product of the hydroxide. At low pH OH^- vanishes, so, if present, the metal hydroxide dissolutes to restore its solubility product. The metal

ions, which are positively charged, migrate towards the cathode by advective pore fluid flow and by electromigration. When they reach the alkaline front, where there is an excess of OH^-, metal hydroxide precipitates.

2.1.4 Carbonates dissolution/precipitation

Solid particles are formed by a variety of minerals. Silica minerals (e.g., quartz SiO_2) are very stable minerals, more resistant to chemical-physical attack by weathering than other minerals. Carbonates, in the form of calcite ($CaCO_3$), dolomite ($CaMg(CO_3)_2$) and magnesite ($MgCO_3$) are frequently found in soils. They are strongly influenced by the pH: in acid medium carbonates dissolute while in an alkaline medium they precipitate. This behaviour leads to a change in the soil properties, since they are influenced by the minerals that form the solid particles. Gabrieli et al. (2008b) reported changes in void ratio, stiffness and hydraulic conductivity of a natural soil sample due to the dissolution/precipitation of calcite promoted by electrokinetic treatment.

When carbon dioxide (CO_2) dissolves in water, gaseous $CO_{2(g)}$ becomes aqueous $CO_{2(aq)}$, and some of this associates with water to form carbonic acid (H_2CO_3). Most of the aqueous CO_2 remains dissolved as $CO_{2(aq)}$ and only a little fraction (~1/600) reacts with water to give H_2CO_3. This fact makes difficult to formulate a correct description of CO_2 solubility. In order to facilitate the analysis of the chemical balance a convention (Appelo and Postma, 2005) is adopted in which carbon dioxide dissolved in water and carbonic acid are summed up as $H_2CO_3^*$:

$$H_2CO_3^* = CO_{2\,(aq)} + H_2CO_3\ . \tag{2.7}$$

The equilibrium of CO_2, which is interchanged between the gas and the water phases, depends on its pressure. With the above notation it may be written as:

$$CO_{2(g)} + H_2O \rightleftharpoons H_2CO_3^* \qquad K_h = [H_2CO_3^*]/p_{CO_2} \cong 10^{-1.5}\ . \tag{2.8}$$

Carbonic acid is diprotic and it dissociates in two steps: first the dissociation

into bicarbonate (also called hydrogen carbonate) ion (HCO_3^-) takes place,

$$H_2CO_3^* \rightleftharpoons H^+ + HCO_3^- \qquad K_1 = [H^+][HCO_3^-]/[H_2CO_3^*] \cong 10^{-6.3} , \tag{2.9}$$

afterwards the bicarbonate ion dissociates into the carbonate ion (CO_3^{2-}),

$$HCO_3^- \rightleftharpoons H^+ + CO_3^{2-} \qquad K_2 = [H^+][CO_3^{2-}]/[HCO_3^-] \cong 10^{-10.3} . \tag{2.10}$$

The fractions of total dissolved carbonates as a function of pH can be obtained (Fig. 2.3) from the constants of the equilibria of carbonic acid in water, (2.9) and (2.10), and of the water auto ionization equilibrium, (2.5). At low pH, carbonic acid is the predominant species. At 6.3<pH<10.3 the predominant species becomes HCO_3^-, while at high pH CO_3^{2-} prevails.

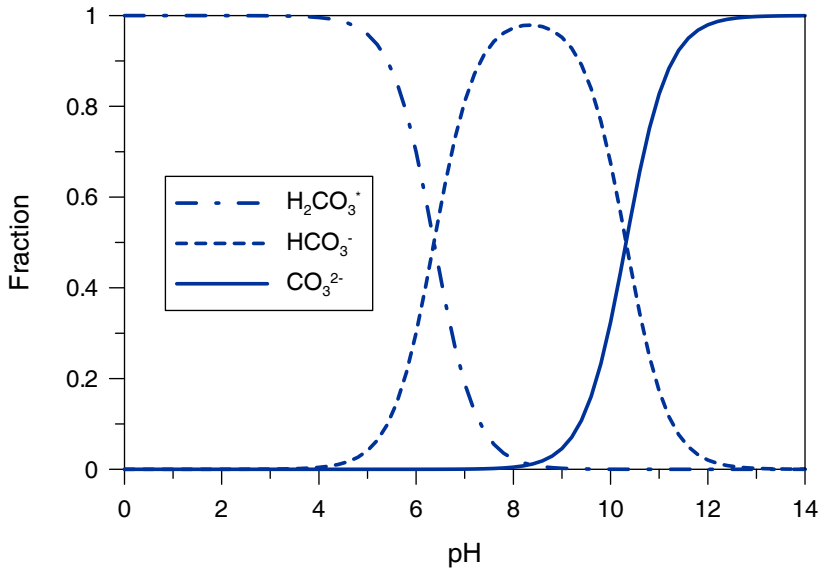

Figure 2.3: Fractions of total dissolved carbonates.

Equilibrium of carbonic acid in water, (2.9) and (2.10), associated to the equilibrium of CO_2 in water, (2.8), and to the water auto ionization equilibrium, (2.5), implies a direct relationship between the CO_2 pressure and the acidity of the water solution. High CO_2 results in a low pH, and basic conditions correspond to modest CO_2 pressures.

Calcite is the most common carbonate present in soils (Mitchell and Soga, 2005)

It is a ionic compound and it dissociates into its constituent ions, calcium (Ca^{2+}) and carbonate:

$$CaCO_3 \rightleftharpoons Ca^{2+} + CO_3^{2-} \qquad K_s = [Ca^{2+}][CO_3^{2-}] \cong 10^{-8.3} \,. \tag{2.11}$$

As shown before, at low pH carbonate ion vanishes, so, if present, calcite has to dissolute to restore its equilibrium. On the contrary, at high pH there is an excess of carbonate and calcite precipitates. Dissolution and precipitation of calcite contributes to the buffering capacity of natural soils.

2.2 Use of electrokinetic in soil mechanics

The first engineering applications of electroosmosis in soil mechanics date in the 1930's, after Leo Casagrande's studies about soil consolidation and dewatering. In his early experiments Casagrande (1949) observed, over different soils, a linear relation between electroosmotic flow and applied current (*Casagrande law*). At that time, the point using electrokinetic in soil mechanics was to increase the soil strength. The general principle applied was to use the electrical gradient to produce a flow of water through the soil and to increase effective stress. Subsequent studies reported successful applications of electroosmosis to stabilise slopes, excavations, foundation piles, embankments and dams (e.g. Bjerrum et al., 1967; Casagrande et al., 1981; Chappel and Burton, 1975; Fetzer, 1967; Finzi and Veder, 1962; Lomizé et al., 1957). In the 1990's the use of electrokinetic treatments was proposed to stabilise the leaning Tower of Pisa (Calabresi et al., 1992; Viggiani and Squeglia, 2003). The idea was to consolidate the clay on the north side of the tower in order to reduce the angle of tilt. Recently coupled use of electroosmosis techniques and geosyntethics has been proposed (Hamir et al., 2001; Jones et al., 2006). In general electroosmosis consolidation is suggested for fine grained soils, although in few cases application to sandy soils has been reported (Rittirong et al., 2008).

Esrig (1968) studied the dependence of pore pressure on the drainage boundary conditions in a theoretical one-dimensional system (incompressible saturated material and uniform electric potential gradient). The possible cases are depicted in Figure 2.4. Esrig suggested that no excess pore pressure will develop if drainage

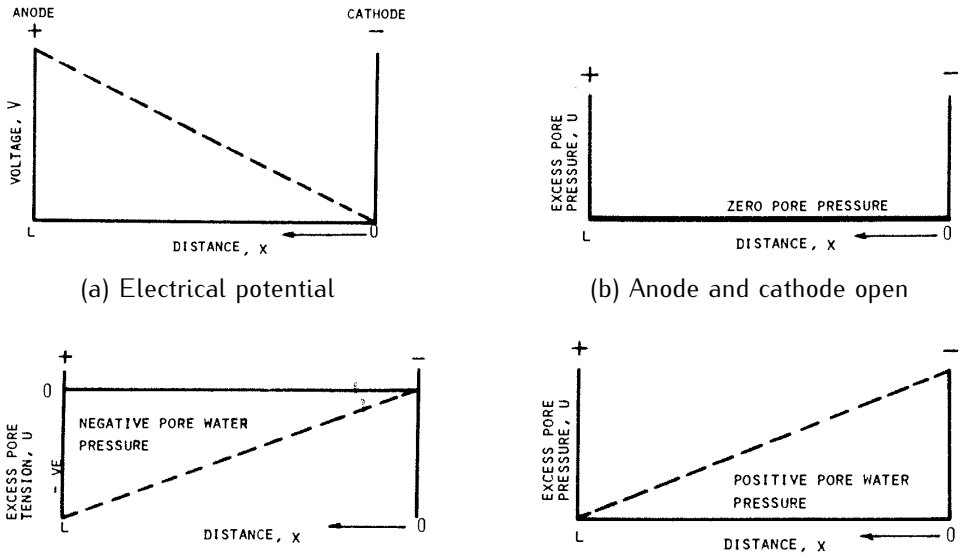

(a) Electrical potential

(b) Anode and cathode open

(c) Anode closed, cathode open

(d) Cathode closed, anode open

Figure 2.4: Pore pressure development in an uniform field (Esrig, 1968).

is allowed at both electrodes (Fig. 2.4b). If no drainage is imposed at the anode then a negative pore pressure will develop at the anode (Fig. 2.4c). The maximum value of negative pressure will be equal to

$$u^{max} = -\frac{k_e}{k_h}\gamma_w V_M, \tag{2.12}$$

where k_e is the electroosmotic permeability coefficient, k_h is the hydraulic conductivity coefficient , γ_w is the water unit weight and V_M is the total potential drop across the sample. The pore pressure increases linearly from its maximum negative value at the anode to zero at the cathode. At the opposite a positive pore pressure will develop if no drainage is imposed at the anode (Fig. 2.4d).

Various solutions for electrokinetic consolidation for different initial and boundary conditions are available (Esrig, 1968; Su and Wang, 2003; Wan and Mitchell, 1976). The solution developed by Wan and Mitchell (1976) refers to the case of one-dimensional consolidation with drained cathode, undrained anode and linearly distributed initial pore pressure,

$$u_0(x) = u_0^{max}\left(\beta - \alpha\frac{x}{L}\right) \ , \tag{2.13}$$

where u_0^{max} is the maximum value of pore pressure, α and β are constants. The solution in terms of normalised pore pressure $U = u/u^{max}$ is

$$U = Z + \sum_{m=0}^{\infty} \frac{2}{M} \left(\beta n - \frac{(-1)^m}{M} (\alpha n + 1) \right) \sin(MZ) \exp\left(-M^2 T\right), \tag{2.14}$$

where $M = (2m+1)\pi/2$, $n = u_0^{max}/u^{max}$ is the ratio between the maximum initial and the maximum final pore pressure, $Z = x/L$ is the dimensionless distance and $T = c_v t/L^2$ is the time constant. The isochrones of normalised pore pressure are shown in Fig. 2.5 for different initial pore pressure distributions.

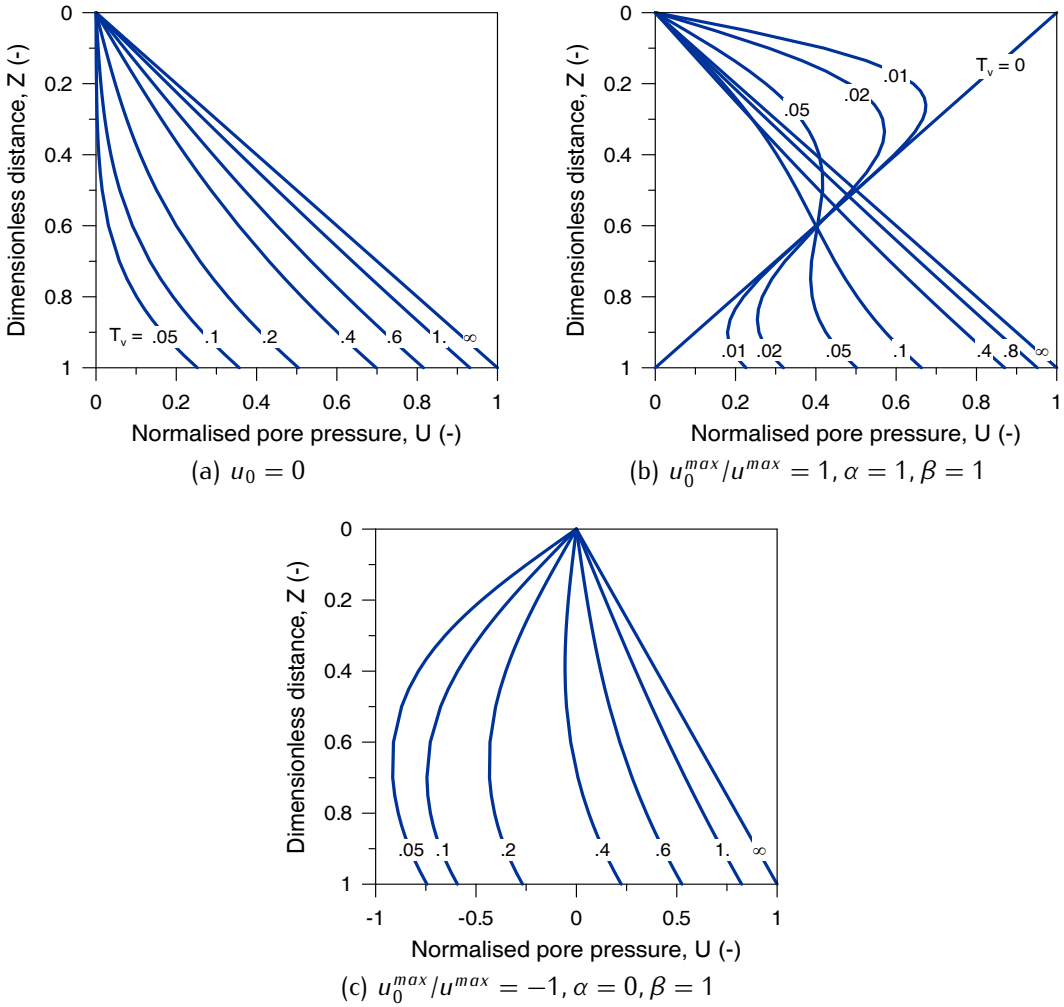

(a) $u_0 = 0$

(b) $u_0^{max}/u^{max} = 1, \alpha = 1, \beta = 1$

(c) $u_0^{max}/u^{max} = -1, \alpha = 0, \beta = 1$

Figure 2.5: Isochrones of the normalised pore pressure.

The second case (Fig 2.5b) describes consolidation after electrode reversal. As described before, in case no drainage is imposed at the cathode no consolidation occurs at the cathode. Consolidation at the cathode could be obtained by reversing the polarities of the electrodes and the drainage conditions after the first equilibrium state is approached (Wan and Mitchell, 1976).

The third case (Fig 2.5c) describes electroosmotic consolidation superimposed on direct loading consolidation. The application of a direct load induces a constant excess pore pressure. The electroosmotic consolidation leads to dissipation of the excess pore pressure in a shorter time. The average degree of consolidation $\bar{U}$ is

$$\bar{U} = \frac{1}{1-\frac{r}{2}} \left(1 - \frac{r}{2} - \sum_{m=0}^{\infty} \frac{2}{M^2} \left(1 - \frac{(-1)^m r}{M} \right) \exp(-M^2 T_v) \right) \tag{2.15}$$

where $r = u^{max}/u_0^{max} = 1/n$. In Figure 2.6 the average degree of consolidation for different values of r is shown.

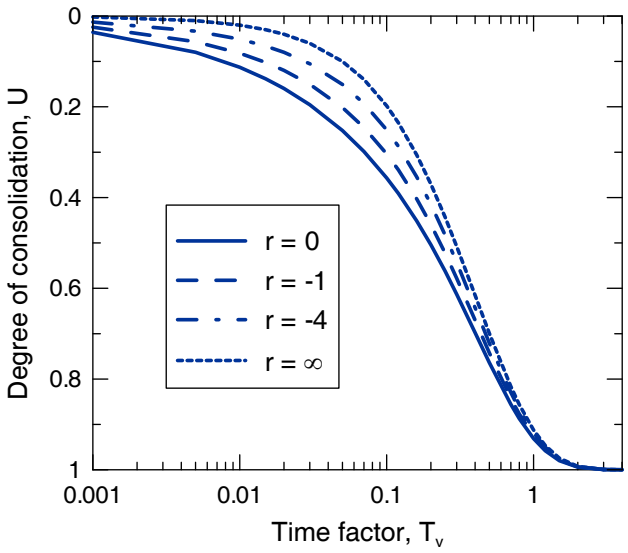

Figure 2.6: Average degree of consolidation.

Although the researches presented in the literature had shown feasibility of electrokinetic in soil mechanics applications, its effects on the physicochemical changes of the soil medium have received limited attention. This is principally due to the complexity of the chemical - mechanical interactions that develop in the

presence of an electrical field and to the high heterogeneity of experimental results.

Following the experimental results of Gabrieli et al. (2008a,b), Tamagnini et al. (2010) focused on the effects of water electrolysis on soil consolidation. The gas generated at the electrodes has a definite impact on the time evolution of the process, affecting the hydraulic, the electro-osmotic and the electrical conduction properties, as well as on the soil skeleton stiffness.

2.3 Use of electrokinetic in environmental engineering

The use of electrokinetic in waste management, which started from mid 1980's, has focused on three main objectives:

- to form a barrier to contaminant;
- to remediate polluted soils;
- to treat sludges.

2.3.1 Electrokinetic barrier

Electrokinetic barriers are designed to counteract contaminant transport due to hydraulic and chemical gradients. In an electrokinetic barrier an electrical potential gradient, opposite to the flow direction, is applied continuously or periodically. The combined effect of electroosmosis and electromigration reduces the contaminant migration. Obviously an electrokinetic barrier is effective if the contaminant movement due to diffusion (v_{diff}) and hydraulic gradient (v_{hydr}) is lower than the movement due to ion migration (v_{ion}) and electroosmosis (v_{elsm}):

$$v_{diff} + v_{hydr} < v_{ion} + v_{elsm} \ . \tag{2.16}$$

Electrokinetic barriers could be used in clay liners (Fig 2.7a) or in groundwater (Fig 2.7b).

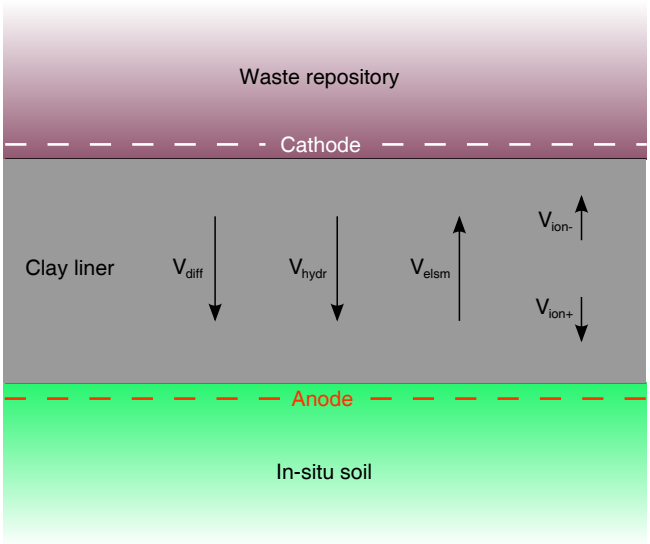

(a) in clay liner

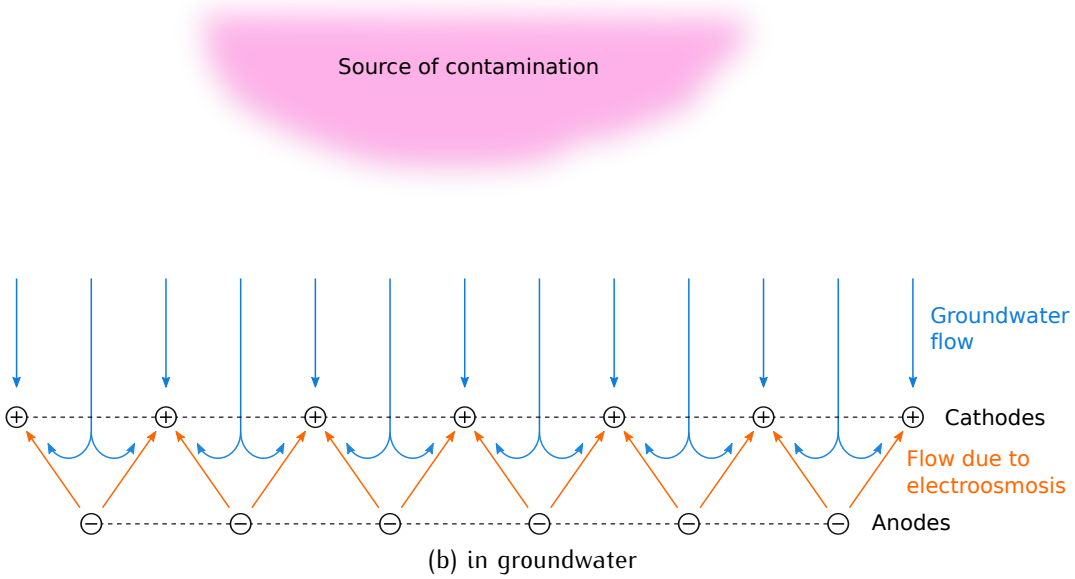

(b) in groundwater

Figure 2.7: Scheme of an electrokinetic barrier.

Clay liners are used in landfills to minimise contaminant migration towards the environment and they are designed to be effective for decades after the closure of the facility. To achieve these goals liners are made of very low permeable clays. However, sustained hydraulic and chemical gradients may result in transport of contaminant through liners on the long term. The application of an electric field improves the clay liner effects in preventing contaminants migration.

Electrokinetic barriers in groundwater modify the flow pattern and thereby they are used to manipulate contaminant plumes. Lageman et al. (1989b) proposed two different arrangements of electrodes for different soils:

- in low permeable soils (< 1 m/year) the lines of electrodes should be placed around the plume. The cathodes are closer to the source of contamination in order to counteract the contaminant migration;

- in relatively high permeable soils (> 1 m/year), where the groundwater flow is remarkable, the electrodes should be placed perpendicular to the direction of the groundwater flow. The anodes are closer to the source of contamination in order to divert the plume, to collect the contaminant around the electrodes and to remove it periodically.

Experimental results shown that electrokinetic barriers may be effective in reducing the transport of cationic and non-ionic species, while transport of anionic species is accelerated (Yeung and Mitchell, 1993); this because the transport of cations due to ion migration has the same direction of the electroosmotic flow, while the electromigration of anions is opposed to the electroosmotic flow. In order to reduce the anions transport Narasimhan and Sri Ranjan (2000) proposed the application of another row of cathodes on the downstream side of the anode.

Design of an electrokinetic barrier requires the study of the changes on the characteristics of the clay due to electrical field. Experimental evidences suggest in fact that also short (few hours) electrokinetic treatments can lead to changes in soil pore distribution (Gabrieli et al., 2008a). Increase in the pore size may increase the hydraulic conductivity of the soil reducing the efficiency of the barrier.

2.3.2 Soil remediation

In Figure 2.8 the classical scheme of electrokinetic soil remediation treatment and of the coccuring related phenomena occurring is shown. As pointed out in paragraph

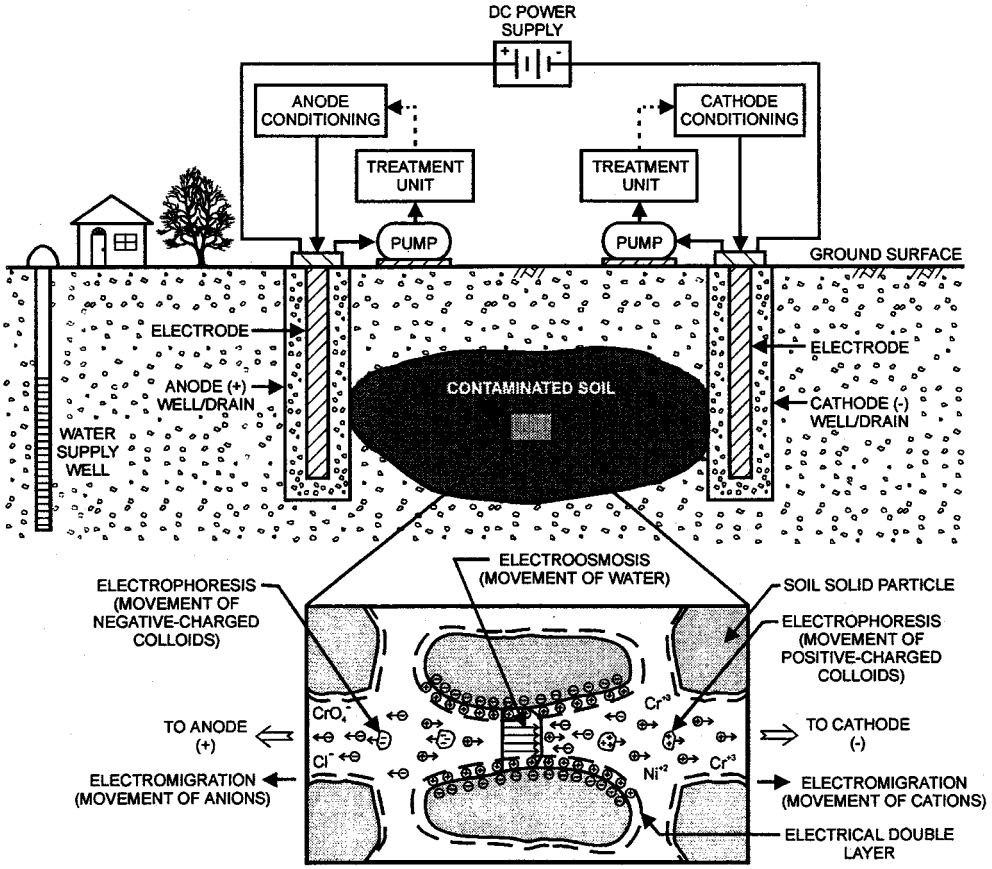

Figure 2.8: Scheme of the *in-situ* electrokinetic soil remediation treatment and related electrokinetic phenomena (from Reddy and Parupudi, 1997).

2.1.3, when an electric field is applied to contaminant soil, migration of charged ions occurs. Positive ions are attracted to the cathode, which is negatively charged, and negative ions move to the anode, which is positively charged. It has been experimentally proved that non-ionic species are transported by advective water flow (Bruell et al., 1992) but, since ionic species are transported by both advective water flow and electromigration, their removing efficiency is lower than the one of the ionic species. In fact the contaminant transport due to electromigration is one

or two orders of magnitude greater than the contaminant transport due to other mechanisms (Reddy and Parupudi, 1997). Therefore the removing efficiency of a contaminant is influenced by the contaminant type, other than by its concentration and by the soil type, as well as by the interfacial chemistry and the conductivity of the soil pore water. Migration of contaminants results in high concentration at the electrodes. Water at the electrodes must then continuously be extracted from the soil and treated.

Efficient removal of metallic contaminant is also influenced by the pH of the soil. As pointed out in paragraph 2.1.3, low-pH environment developing at the cathode inhibits metallic contaminants from being sorbed onto soil particle surfaces and favours the formation of soluble compounds. On the contrary, close to the cathode, where there is an alkaline environment, metal hydroxides precipitate. In order not to reduce removing efficiency, the pH of the soil should be maintained low enough to keep all contaminants in the dissolved phase. To improve removing efficiency Acar et al. (1993) suggest to use enhancement techniques. Acar et al. (1993) also pointed out the characteristics of an ideal enhancement technique:

- *precipitates should be solubilised and/or precipitation should be avoided;*
- *ionic conductivity across the specimen should not increase excessively in a short period of time to avoid a premature decrease in the electroosmotic transport;*
- *the cathode reaction should possibly be depolarised to avoid the generation of hydroxide and its transport into the specimen;*
- *depolarisation will decrease the electrical potential difference across the electrodes, which would result in lower energy consumption;*
- *if any chemical is used, the precipitate of the metal with the new chemical should be perfectly soluble within the pH range attained;*
- *any special chemicals introduced should not result in any increase in toxic residue in the soil mass;*
- *the cost efficiency of the process should be maintained when the cost of enhancement is included.*

A possible enhancement technique is the depolarisation of the cathode reactions by injection of an acid (Acar and Alshawabkeh, 1993). The hydrochloric acid is a strong acid and it is very effective, although it can form chlorine gas because of electrolysis when it reaches the anode. Another concern about the use of hydrochloric acid is potential production of chloride that may increase the soil contamination. The use of acetic acid, a weak acid, it is attractive because is environmentally safe.

Another enhancement technique is the use of a ion-selective membrane at the cathode (Alshawabkeh et al., 1999). The membrane should be permeable to cations and polar compunds and impermeable to anions and nonpolar negatively charged compounds. Moreover it should be chemically resistant to strong oxidizing agents and strong bases.

3

Governing equations

3.1 Coupled flows

Soil is not a homogeneous material. Due to its complexity, in soil four principal flows can be identified: fluid, heat, electrical and chemical. Depending on the specific application, one or more flows have to be taken into account and the others can be neglected. In soil mechanics the flow of the fluid phases, liquid and gas, plays an essential role in problems of seepage, consolidation and stability in unsaturated conditions. As described in Section 2.2 fluid and electrical flows affect electroosmosis. Chemical transport is a major concern in groundwater pollution, waste storage, remediation of contaminated sites and soil stabilisation. Heat flow is important in relation to frost action, construction in permafrost areas and temporary ground stabilisation by freezing (Mitchell and Soga, 2005).

Each of the four principal flows is related to a corresponding driving force:

$$\text{Fluid flow} \qquad q_h = k_h i_h A \qquad \text{Darcy law ,} \tag{3.1a}$$

$$\text{Heat flow} \qquad q_t = k_t i_t A \qquad \text{Fourier law ,} \tag{3.1b}$$

$$\text{Electrical flow} \qquad I = \sigma_e i_e A \qquad \text{Ohm law ,} \tag{3.1c}$$

$$\text{Chemical flow} \qquad J_D = D i_c A \qquad \text{Fick law .} \tag{3.1d}$$

In Equation (3.1) the driving forces are the hydraulic gradient i_h, the thermal gradi-

ent i_t, the electrical gradient i_e and the chemical gradient i_c. The above four laws are often referred to as *direct flows*.

In addition to the direct flows several coupled flows take place because of the presence of the double layer, even when only a driving force is acting. Yeung and Mitchell (1993) summarised the direct and the coupled flows with respect to the driving force (Tab. 3.1). Every flow J_i could be related to the gradient X_j by a law

Table 3.1: Direct and coupled flow phenomena (after Yeung and Mitchell, 1993).

	Hydraulic gradient	Electrical gradient	Chemical gradient	Thermal gradient
Fluid flow	Hydraulic conduction	Electro-osmosis	Normal osmosis	Thermal osmosis
Electric current	Streaming potential	Electric conduction	Membrane potential	Seeback effect
Ion flow	Streaming current	Electrophoresis	Diffusion	Soret effect
Heat flow	Isothermal heat transfer	Peltier effect	Dufour effect	Thermal conduction

of the type

$$J_i = L_{ij} X_j \ . \tag{3.2}$$

The coefficients L_{ii} are the conductivity coefficients defined in Equations (3.1). The other coefficients L_{ij} are called *coupling coefficients*. Quantification of the coupled flow processes could be done with two different approaches, each of them having advantages and limitations.

In the first approach the quantification of a particular flow arises from the observation of experimental results. Within this approach is generally assumed that the others soil properties remain unchanged during the flow process. This assumption may not always be justified. However, when properties are known to vary in a predictable manner, their variations could be taken into account into the quantification problem.

An alternative approach was developed by Yeung and Mitchell (1993). They formulated the equations for the simultaneous flows of water, electricity, cations, and anions under hydraulic, electrical, and chemical gradients using the theory of

irreversible thermodynamics developed by Onsager (1931).

3.2 Liquid flow

Of the four gradients described before the hydraulic and the electric gradients are the only ones taken into account when the electrokinetic problem is studied. Chemicoosmosis can in fact be neglected since it is significant only in presence of large chain molecules and in very active clay deposits.

3.2.1 Darcy's Law

The flow of water in saturated soils is commonly described by Darcy's law. Darcy's law states that the seepage velocity is linearly related to the gradient of the hydraulic head. Extended to unsaturated soils and written in terms of liquid pressure it becomes:

$$\mathbf{v}_l^h = -\frac{\boldsymbol{\kappa} k_l^{rel}}{\mu_l} \left(\nabla u_l + \rho_l g \boldsymbol{\delta}_{zx}\right) \ , \tag{3.3}$$

where $\boldsymbol{\kappa}$ is the absolute permeability tensor, k_l^{rel} is the relative permeability of the liquid phase, μ_l is the liquid dynamic viscosity, u_l is the liquid pressure, ρ_l is the liquid density, g is the gravity and $\boldsymbol{\delta}_{zx}$ is the direction of the gravity. Air and chemical species are dissolved in water, which is the main component of the liquid phase. Therefore the dynamic viscosity and the density of water could be used. Under this approximation the Darcy's law for the liquid phase reads:

$$\mathbf{v}_l^h = -\frac{\boldsymbol{\kappa} k_l^{rel}}{\mu_w} \left(\nabla u_l + \rho_w g \boldsymbol{\delta}_{zx}\right) \ . \tag{3.4}$$

The absolute permeability tensor is a property of the porous medium and it is independent from the wetting fluid. It depends on the pore size distribution, decreasing from coarse to fine grained soils and its value ranges between different orders of magnitude. Because of this dependence, within the same soil the absolute permeability could exhibit variation up to 2 or 3 orders of magnitude as a result of changes in fabric and void ratio (Mitchell and Soga, 2005).

The relative permeability of the liquid phase is an increasing function of the

degree of saturation. It can assume values between 0 and 1.

3.2.2 Electroosmotic flow

Casagrande (1949) observed a linear relation between the electroosmotic flow and the electric gradient in saturated conditions (*Casagrande law*):

$$\mathbf{v}^{eo} = -\boldsymbol{k_e} \nabla \Phi \ , \tag{3.5}$$

where k_e is the electroosmotic coefficient and Φ is the electric potential.

As for the Darcy's law, the Casagrande's Law may be generalised to unsaturated conditions by means of a relative permeability k_e^{rel},

$$\mathbf{v}_l^e = -\boldsymbol{k_e} k_e^{rel} \nabla \Phi \ . \tag{3.6}$$

The relative electroosmotic permeability k_e^{rel} is an increasing function of the degree of saturation.

3.2.3 Total liquid flow

Summing up the contributions of hydraulic and electroosmotic contributions, the total liquid flow reads:

$$\mathbf{v}_l = \mathbf{v}_l^h + \mathbf{v}_l^e = -\frac{\boldsymbol{\kappa} k_l^{rel}}{\mu_w} \left(\nabla u_l + \rho_w g \boldsymbol{\delta}_{zx}\right) - \boldsymbol{k_e} k_e^{rel} \nabla \Phi \ . \tag{3.7}$$

3.3 Gas flow

Flow of the gas phasemay be described by a generalised Darcy's Law as a function of the gradient of the gas head:

$$\mathbf{v}_g = -\frac{\boldsymbol{\kappa} k_g^{rel}}{\mu_g} \left(\nabla u_g + \rho_g z \boldsymbol{\delta}_{zx}\right) \ , \tag{3.8}$$

where k_g^{rel} is the relative permeability of the gas phase, μ_g is the gas dynamic viscosity, ρ_g is the gas density and u_g is the gas pressure.

Assuming the gas phase to behave as an ideal gas, its density is related by on gas pressure by the ideal gas law:

$$\rho_g = \rho_g^0 \frac{u_g + p_{atm}}{u_g^0 + p_{atm}} \ , \tag{3.9}$$

where p_{atm} is the atmospheric pressure, ρ_g^0 and u_g^0 are the gas density and pressure for the reference state, respectively.

The gas phase is a mix of different gas, therefore its properties are an average of the properties of its constituents. Due to chemical reactions the composition of the gas phase may change. However, since the dynamic viscosities of different gas have the same order of magnitude, a mean constant value can be assumed.

3.4 Chemical species flow

Flow of a chemical species is the result of different gradients. In electrokinetic processes the flow is due to electric, chemical and hydraulic gradients. The electric gradient causes the movement of charged species, and this process is called electromigration.

3.4.1 Fick's law

Diffusive flow is driven by chemical potential gradients, but for most applications chemical concentration gradients can be used. Fick's law can be adopted to describe diffusion phenomena like flow of a chemical species due to its concentration gradient:

$$\mathbf{J}_i^d = -D_i \nabla c_i \ , \tag{3.10}$$

where D_i and c_i are the diffusion coefficient and the concentration of the chemical species, respectively. Equation (3.10) refers to the flow of a chemical species in free solution at infinite dilution. The diffusion coefficient for different ions are available in most electrochemistry handbooks and references. Diffusion in soil is slower than diffusion in free solution. The main reasons for this fact are the presence of the solid particles in the REV that reduces the cross-sectional area for flow and the tortuous

migration flow path around particles. When diffusion take place in a porous medium the Fick's law is rewritten as:

$$\mathbf{J}_i^d = -\mathbf{D}_i^* \nabla c_i \ . \tag{3.11}$$

$\mathbf{D}_i^*$ is referred as *effective diffusion coefficient* (Shackelford and Daniel, 1991) and it takes into account the porosity and the tortuosity of the porous medium:

$$\mathbf{D}_i^* = D_i \boldsymbol{\tau} n Sr \ , \tag{3.12}$$

where $\boldsymbol{\tau}$ is a second rank symmetric tensor and it represents the tortuosity of the porous medium. In Equation (3.12) nSr represents the volumetric water fraction and it accounts for the reduction in the area active in the transport.

In an isotropic porous medium the tortuosity tensor may be represented as $\tau\mathbf{I}$, where $\mathbf{I}$ is the identity matrix. There is not a unique definition of tortuosity. Some authors (e.g. Li and Gregory, 1974) define tortuosity as the length of the path followed by a particle divided by the length of the direct path, so it is grater than 1. Other authors (e.g. Alshawabkeh and Acar, 1996) refer to tortuosity as the inverse of the previous definition, using it as a retarding factor. In this work the latter definition has been chosen. Shackelford and Daniel (1991) summarise τ values for different soil types taken from literature. The reported values of τ span over a wide range for different soils.

3.4.2 Advective flow

Advective flow results from the movement of the liquid phase, which drags the molecules of the dissolved species:

$$\mathbf{J}_i^l = c_i \mathbf{v}_l \ . \tag{3.13}$$

3.4.3 Electromigration

Electric gradient to will cause migration of ionic species according to the equation:

$$\mathbf{J}_i^e = -nSr\boldsymbol{\tau}\mu_i c_i \nabla \Phi \ , \tag{3.14}$$

where μ_i is its ionic mobility at infinite dilution and Φ is the electric potential.

Ionic mobility is given a sign such that anions, which are negative charged, migrate towards the cathode while cations, positively charged, move towards the anode. Ionic mobility is not derived on an experimental base. It is estimated applying the *Nerst-Townsend-Einstein equation* (Atkins, 1982). Since the Nerst-Townsend-Einstein equation is written for infinite dilution, the assumption that it holds also in the pore fluid has to be introduced. Therefore, the ionic mobility of the i-th specie is estimated as:

$$\mu_i = \frac{z_i D_i F}{RT} \ , \tag{3.15}$$

where z_i is the electric charge of the chemical species, F is the Faraday's constant equal to 96485 C/mol electrons, R is the universal gas constant equal to 8.3144 J/Kmol, and T is the absolute temperature. Introducing Equation (3.12) into Equation (3.15) results in the definition of the *effective ionic mobility*:

$$\mu_i^* = \frac{z_i D_i^* F}{RT} = n\boldsymbol{\tau} Sr \frac{z_i D_i F}{RT} = n\boldsymbol{\tau} Sr \mu_i \ . \tag{3.16}$$

Eventually, the flux due to electromigration reads:

$$\mathbf{J}_i^e = -\mu_i^* c_i \nabla\Phi \ . \tag{3.17}$$

3.4.4 Total flow

The total mass flow of the i-th chemical species is the sum of the mechanisms described before:

$$\mathbf{J}_i = \mathbf{J}_i^d + \mathbf{J}_i^l + \mathbf{J}_i^e = \\ - \mathbf{D}_i^* \nabla c_i - c_i \frac{\boldsymbol{\kappa} k_l^{rel}}{\mu_w} \left(\nabla u_l + \rho_w g \boldsymbol{\delta}_{zx}\right) - c_i \left(\boldsymbol{k_e} k_e^{rel} + \mu_i^*\right) \nabla\Phi \ . \tag{3.18}$$

In Figure 3.1 the effects of the different transport mechanism of the chemical species are shown. Since advective flow (due to electroosmosis and hydraulic gradient) acts from anode to cathode, it will enhance the transport of the cationic

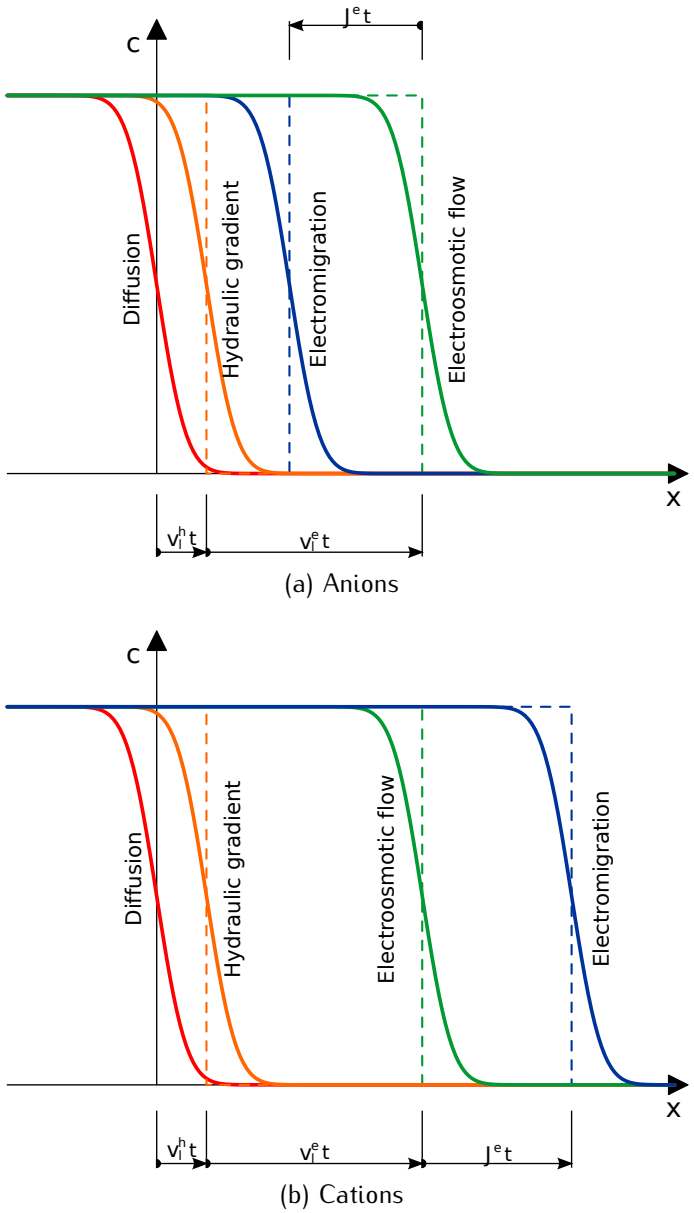

Figure 3.1: Comparison of different chemical flow processes.

species, which migrates from the anode to the cathode, and retards that of the anionic species, which migrates from the cathode to the anode.

Electrically driven chemical flow is relatively less important in high permeability soils and more important in soils with lower κ. In fact, in a clay having a hydraulic conductivity of about 10^{-9} m/s, the chemical flow due to a potential gradient of the

order of 1 V/m is bigger than that due to advective flow under a unit hydraulic gradient. At the opposite, advective transport, due to hydraulic gradient, is the dominant process for soils having a hydraulic conductivity greater than 10^{-7} m/s and for non-charged chemical species.

The contribution of diffusion to the chemical flow is usually negligible compared to electromigration. In fact the chemical flow due to a potential gradient of the order of 1 V/m is equal to a flow due to a chemical gradient of the order of 1 mol/m^3/cm. Chemical gradients of this order of magnitude are typical of an advancing front. Advancing front is limited in space, therefore its contribution to total flux is negligible. Nonetheless the diffusion process has to be taken into account in order to reproduce the advancing front.

3.5 Electric current

3.5.1 Ohm's law

Electric current density due to electric potential gradient is provided by the Ohm's law,

$$\mathbf{j} = -\sigma^* \nabla \Phi \,, \tag{3.19}$$

where σ^* is the *effective electric soil conductivity* and Φ is the electric potential.

The effective electric conductivity is a primary result of electrokinetic laboratory tests. It is defined as the ratio between the potential drop ΔV between two section of the sample and their distance Δx:

$$\sigma^* = \frac{\Delta V}{\Delta x} \,, \tag{3.20}$$

In a porous medium current flows through different paths (Fig. 3.2):

- through solid particles, under the hypothesis that solid particles are interconnected;
- through fluid flow.

The soil-water system may therefore be sketched as three electrical resistors in parallel (Fig. 3.2b). When two electrical resistors are connected in parallel the

conductivity of the circuit is the sum of the conductivity of the resistors, hence the effective conductivity of the soil-water system is:

$$\sigma^* = \sigma_s + nSr\tau\sigma_f \ , \tag{3.21}$$

where σ_s and σ_f are the electrical conductivity of the solid particles and of the pore fluid, respectively. The electrical conductivity of the pore fluid depends on the concentration of the chemical species:

$$\sigma_f = \sum_{i=1}^{N} z_i F \mu_i c_i \tag{3.22}$$

where F is the Faraday's constant.

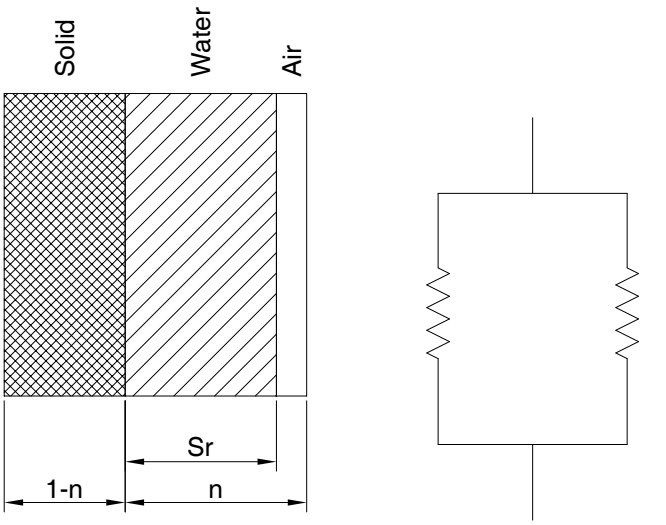

(a) Path

(b) Analogy with the electrical circuit.

Figure 3.2: Soil electrical conductivity.

3.5.2 Diffusional charge flux

Ion diffusion results in a charge flux. This flow may be evaluated using Faraday's law of equivalence of mass flow and charge flow:

$$\mathbf{j}^d = \sum_{i=1}^{N} z_i F \mathbf{J}_i^d \ . \tag{3.23}$$

Substituting Equation (3.11) in the previous one gives for the diffusional charge flux:

$$\mathbf{j}^d = -\sum_{i=1}^{N} z_i F \mathbf{D}_i^* \nabla c_i \ . \tag{3.24}$$

3.6 Continuity equations

The generic continuity equation could be summarised as:

$$input = output + accumulation + generation. \tag{3.25}$$

The Eulerian approach it states that the amount of a quantity inside any region can change by the amount that flows in or out across the boundary or by the amount of the same quantity generated inside the region. The amount that flows across the boundaries is due to the mechanisms described before.

Any continuity equation can be expressed in an *integral form*, which applies to a finite region, or in a *differential form*, which applies to an infinitesimal region (called *representative elementary volume*, REV). In this section only the differential form will be described. The integral form, which is the base of the formulation of the finite element method, will be developed from the differential form in Chapter 7.

3.6.1 Water mass balance

In the pores water is present both in its liquid and gaseous phases (superscript l and g respectively). The total water mass contained in a representative volume

element of an unsaturated soil is:

$$m_w = m_w^l + m_w^g \ . \tag{3.26}$$

The water mass present in the liquid phase, m_w^l, is:

$$m_w^l = nSr\rho_w \ , \tag{3.27}$$

where n is the soil porosity and ρ_w is the water density.

The water mass in the gas phase, m_w^g, is calculated using the psychrometric laws and depends on the temperature and on the gas and liquid pressures. However the ratio between the water mass in the gas and in the liquid phases does not depend on the water retention curve (Fig. 3.3). Compared to m_w^l, in most cases m_w^g is negligible ($m_w^g \approx 10^{-5}\, m_w^l$). m_w^g becomes significant when the degree of saturation is very low, like in case the residual water content is reached (Fig. 3.3). It is worth noting that the ratio between water mass in the gas and in the liquid phase does not differ much for different water retention curves, even if the curves are very different one to the other.

Therefore, the water mass balance reads:

$$\frac{\partial(nSr\rho_w)}{\partial t} + \nabla \cdot (\rho_w \mathbf{v}_l) + R_w = 0 \ , \tag{3.28}$$

where n is the porosity, Sr is the degree of saturation, ρ_w is the water density, $\mathbf{v}_l$ is the seepage velocity of the liquid phase and R_w is the source term.

The source term describes the contribution of possible sinks. In this context, a sink term may be associated to chemical reactions. Nonethless, in soil mechanics water acts as a solvent, so the water mass production due to chemical reactions is negligible compared to the total water mass. For this reason the source term in the water mass balance can be neglected.

3.6.2 Chemical species mass balance

Since the molecular mass of any chemical specie is constant, the continuity equation of the chemical species could be written in terms of number of moles instead of in

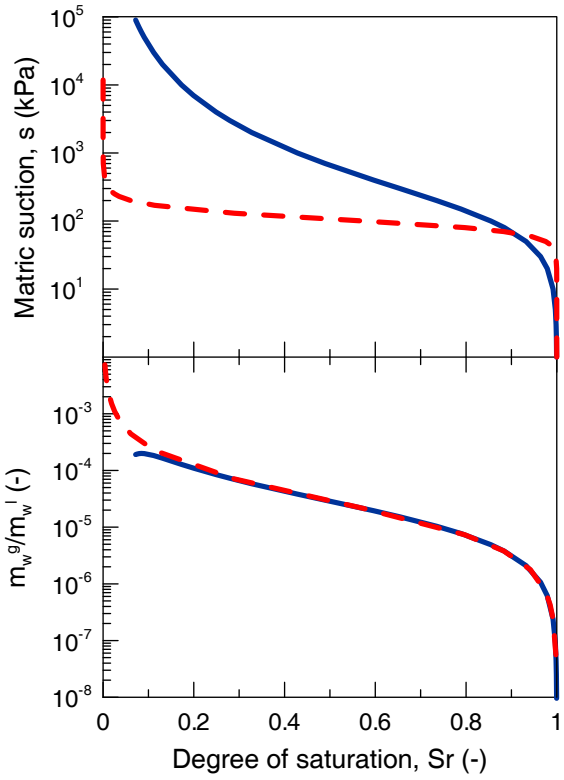

Figure 3.3: Ratio between water mass in the gas and in the liquid phase.

terms of mass. Namely the variation of the number of moles is equal to the number of moles inflowing into the control volume and to the number of moles generated from chemical reactions.

Except water, the mass balance of which was described before, in soils chemical species are present in three different forms: dissolved in the liquid phase, as a fraction of the gas phase or as a part of the solid phase. It is convenient to treat the three form separately. The presence of chemical specie in different forms (dissolved in the liquid phase or part of the solid and the gaseous phase) leads to complex behaviour involving heterogeneous equilibria like the dissolution/precipitation of calcite described in Section 2.1.4.

Aqueous chemical species

Chemical equilibria depend on chemical activity. However the equilibrium constants are usually expressed in terms of molar concentrations for dissolved chemical species and in terms of partial pressures for gaseous species. Therefore, it is convenient to write the mass balance in terms of molar concentration, which is defined as the ratio between the number of moles of solute and the volume of the mixture.

In terms of molar concentration the balance of the i-th aqueous chemical specie reads:

$$\frac{\partial(nSrc_i)}{\partial t} + \nabla \cdot \mathbf{J}_i + nSrR_i = 0 \ , \tag{3.29}$$

where $\mathbf{J}_i$ is the molar flux of the i-th chemical specie, n is the soil porosity, c_i is the concentration of the i-th chemical specie and R_i is its molar production rate due to chemical reactions.

Gaseous chemical species

When a gas interact with a liquid, part of the gas dissolves into the liquid phase according to Henry's law:

$$c_{i(d)} = H_i p_i \ , \tag{3.30}$$

where $c_{i(d)}$ is the concentration of the i-th chemical specie dissolved in the liquid phase, H_i is its coefficient of solubility and p_i is its partial pressure in the gas phase. Thus the mass of the gas specie, m_i, in the pores is:

$$m_i = m_i^d + m_i^g \ , \tag{3.31}$$

where the superscript d and g refer to the dissolved and gaseous mass, respectively. Assuming that the law of perfect gas holds (Vanuat et al., 1997), the balance of the gaseous species i is:

$$\frac{\partial(n\rho_i(1-(1-h_i)Sr))}{\partial t} + \nabla \cdot \left(\mathbf{v}_g + h_i \mathbf{v}_l\right) + nSrm_i^{mol}R_i = 0 \ , \tag{3.32}$$

where ρ_i is the *partial density* of specie i, p_i and m_i^{mol} are its partial pressure and its molar mass respectively, and the degree of saturation, Sr, depends on the pressure of the gas phase, $u_g = \sum_i p_i$. The definition of the partial density ρ_i results from the law of perfect gas:

$$\rho_i = x_i m_i^{mol} \rho_g \ , \tag{3.33}$$

where x_i is the molar fraction of the specie i in the gas phase.

Mineral chemical species

There is not an unique way to treat mineral chemical species. Herein, the solid concentration $\bar{c}$, defined as the number of moles in the REV, is introduced. Therefore the mass balance for mineral species reads:

$$\frac{\partial \bar{c}_i}{\partial t} + nSrR_i = 0 \ . \tag{3.34}$$

Usually mineral species are expressed in terms of mass fraction of the solid phase. The relation between the solid concentration and the mass fraction is:

$$f_i = \bar{c}_i \frac{m_i^{mol}}{\rho_s(1-n)} \ , \tag{3.35}$$

where m_i^{mol} is the molar mass of the species and ρ_s is the density of the solid phase.

3.6.3 Electric charge balance

The balance of the electric charge reads:

$$\frac{\partial Q}{\partial t} + \nabla \cdot \mathbf{j} = 0 \ , \tag{3.36}$$

where Q is the soil capacity and $\mathbf{j}$ is the current density. Neglecting the electrical capacitance of the soil, the balance of the electric charge reduces to a steady-state equation,

$$\nabla \cdot \mathbf{j} = 0 \ , \tag{3.37}$$

which is the classical Laplace equation. Equation (3.37) does not depend explicitly on time and it is not directly coupled to the other variables. Coupling results from the effective electric conductivity σ^*, which depends on the degree of saturation and on the concentration of the ions dissolved in the liquid phase.

3.6.4 Heat Equation

The amount of internal energy Q_H inside a volume is:

$$Q_H = \left(c_p^s \rho_s (1-n) + c_p^l \rho_l n Sr + c_p^g \rho_g n (1-Sr)\right) T \ , \tag{3.38}$$

where c_p^s, c_p^l and c_p^g are the specific heat capacities of the solid, liquid and gas phase and T is the absolute temperature. The energy balance reads:

$$\frac{\partial Q_H}{\partial t} + \nabla \cdot \mathbf{J}_T + Q_{gen} = 0 \ , \tag{3.39}$$

where $\mathbf{J}_T$ is the heat flux and Q_{gen} is the heat generation.

In electrokinetic process the heat is generated by the electric current. This effect is known as *Joule's effect*, which describes the heat generated by an electric current flowing through a conductor.

3.7 Water retention curve

The relationship between the quantity of water present in the void space and the capillary pressure is called *water retention curve* (WRC), since it measures the amount of water retained in the soil by the capillary pressure (Bear and Cheng, 2010). In soil mechanics it is usually written in terms of degree of saturation, Sr, and suction, $s := u_g - u_l$:

$$Sr = Sr(s) \ . \tag{3.40}$$

Experimental data (e.g. Airò Farulla et al., 2011; Gallipoli et al., 2003b; Kawai et al., 2000; Ng and Pang, 2000; Tarantino and Tombolato, 2005) shows that the WRC depends on soil chemo-physical properties and on void ratio.

An idealised representation of the water retention curve is shown in Figure 3.4.

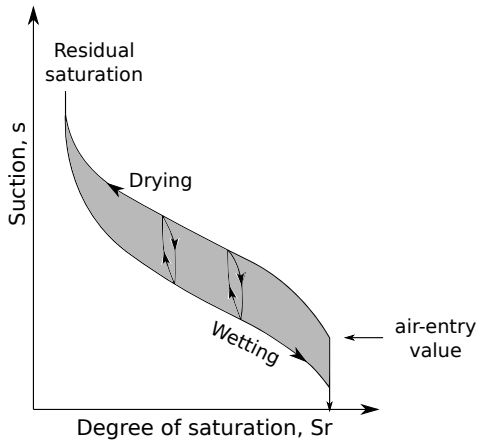

Figure 3.4: Water retention curve.

The possible hydraulic states, described by the couple (s, Sr), are bounded by two main curves. The upper curve is called *main drying curve*, since it is the results of a drying path. At the opposite, the lower curve is named *main wetting curve*. The two curves have a similar shape and they bound a hysteritic domain. Any point located between the main drying and wetting curves belongs to a scanning curve. Experimental results (e.g Topp, 1971) showed that the scanning curves present a loop, which is due to capillary hysteresis. However these loops imply very little variation in degree of saturation, so they may be neglected. The hysteretic behaviour can be attributed mainly to the geometric non-uniformity of individual pores, resulting from the so-called "ink bottle" effect, and to the variation in liquid-solid contact angle during drying or wetting process. However recently Kohgo (2008), Miller et al. (2008) and Nuth and Laloui (2008) pointed out that the WRC hysteresis is also a consequence of soil deformability, not only of the effects listed above.

Traditionally the WRC is divided into four domains (Bear, 1972): the complete saturation in liquid water, the funicular state, the pendular state and the residual state (Fig. 3.5a). The boundaries for each of these states depend on the number of fluid phases filling the porous media and on the nature of each phase (Nuth and Laloui, 2008). When the soil is completely saturated, air is present only dissolved

in the liquid phase. Increasing the matrix suction gas bubbles appear, when the so-called *air entry value* of suction is reached. The air entry value is defined as the value of suction that causes desaturation of the largest pores (Vanapalli et al., 1999). In the funicular state both gaseous and liquid phases are continuous, i.e. a continuous path can be traced through each phases. The pendular state appears at low saturation, and it is the transition between the funicular and the residual states. Characteristic of the pendular state is that the continuity of each phase is not ensured. At the residual state the liquid phase vanishes and water is adsorbed into solid grains.

Romero et al. (1999) suggested to divide the WRC in two regions (Fig. 3.5b). At low suction values, the amount of water stored in the soil is high enough to saturate the pores inside the aggregates ("intra-aggregate pores" or "micropores") and to partly fill the pores between the aggregates ("inter-aggregate pores" or "macropores'). In the latter region, capillary storage mechanisms dominate, which clearly depend on the characteristic dimensions of interconnected macropores, hence on porosity. At high suction values the adsorptive storage mechanisms, where water with lower mobility is held inside the intra-aggregate pores, dominate. Thus in this region the influence of void ratio is negligible and the main curves coincide.

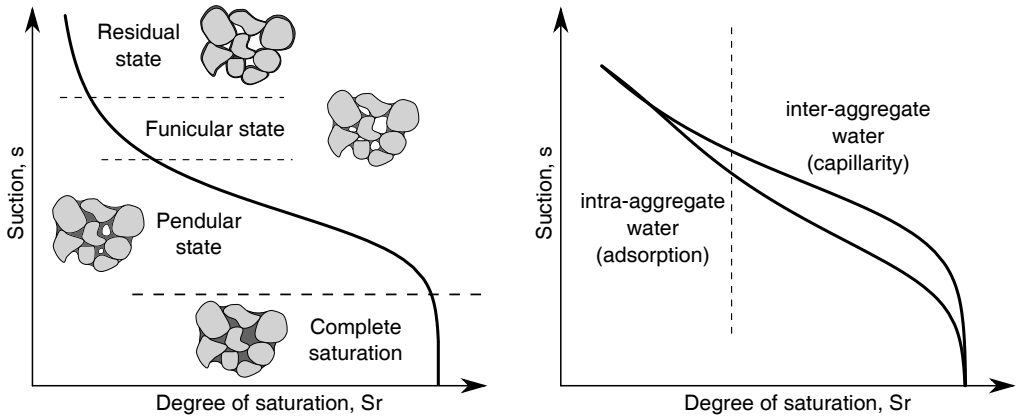

(a) After Bear (1972) (b) After Romero et al. (1999)

Figure 3.5: Subdivision of the water retention curve.

Different shapes for the water retention curve have been proposed in the literature (e.g. Brooks and Corey, 1966; van Genuchten, 1980). The main curves can be

described adopting different values of the parameters of these shapes. With this approach the WRC is independent from the mechanical behaviour. In the last few years different models for the WRC which take into account the dependence on the void ratio have been proposed (e.g. Gallipoli et al., 2003b; Nuth and Laloui, 2008; Romero et al., 2011). These models provide evidence of strong coupling with the mechanical behaviour.

3.8 Reaction rate

The possible reactions in soils could be classified in three different types:

- sorption reactions (surface complexation and ion exchange), R_r^s;
- aqueous phase reactions, R_r^{aq};
- precipitation/dissolution reactions, R_r^{pd}.

Two approaches have been developed and used in the literature to describe chemical reactions: instantaneous equilibrium approach and kinetics approach. In instantaneous equilibrium reactions, be it sorption, precipitation/dissolution, or aqueous phase reactions, species concentrations are assumed to reach equilibrium instantaneously, whereby in kinetic reactions concentrations are assumed to depend explicitly from time and change before matching chemical equilibrium (Alshawabkeh, 2001).

3.8.1 Sorption reactions

The following general term has been considered for sorption evaluation:

$$R_i^s = \frac{\rho}{n}\frac{\partial s_i}{\partial t} = \frac{\rho}{n}\frac{\partial s_i}{\partial c_i}\frac{\partial c_i}{\partial t} \tag{3.41}$$

where ρ is the bulk dry density of the soil defined as the ratio between the mass of the solid particles of the soil and its total volume, s_i is the adsorbed concentration of the component j per unit mass of the soil solids. The reversible term ($\partial s_i/\partial t$) is often used to describe the sorption rate. The equilibrium partitioning between the

adsorbed phase and the aqueous phase of the chemical components are commonly measured under controlled temperature and applied pressure. The resulting relations between s_i and c_i are called adsorption isotherms. Several equilibrium models (linear, Freundlich, and Langmuir models) have been used to describe sorption of heavy metals on soils. Assuming instantaneous equilibrium in sorption reactions and linear isotherms,

$$\frac{\partial s_i}{\partial c_i} = K_{di} \tag{3.42}$$

where K_{di} is called the distribution coefficient, K_d, of species i. A retardation factor, R_{di}, may be introduced in modeling species transport accounting for linear sorption as,

$$R_{di} = 1 + \frac{\rho K_{di}}{n} \tag{3.43}$$

The retardation factor of species i, R_{di}, define the relative rate of transport of a nonsorped species to that of a sorped species. For a nonsorped species, $R_{di} = 1$.

Simple isotherm sorption models ignore the potential effects of variations in pH, solute composition and ionic strength, redox potential, or processes such as competitive adsorption. Alternative, more robust (and complicated) sorption models include ion- or ligand-exchange, mass action models, and surface complexation models as described by Bethke (1996); Davis and Kent (1990); Kirkner and Reeves (1988); Langmuir (1997); Stumm and Morgan (1995); Yeh and Tripathi (1989).

3.8.2 Aqueous reactions

Consider a chemical system containing N^d dissolved species and N^r aqueous reactions. The reactions taking place in the system can be written in the general form (Lichtner, 1985):

$$\nu_{ri} A_i \rightleftharpoons 0 \ , \tag{3.44}$$

where ν_{ri} is the stechiometric coefficient of the i-th specie in the reaction r and A_i denotes the chemical symbol of the i-th specie.

A chemical system is in equilibrium when the Gibbs free-energy is minimum. This condition is expressed by the *the mass action law* between the chemical

species involved in a chemical reaction. The law of mass action implies that:

$$K_r^{aq} \prod_{i=1}^{N^d} c_i^{\nu_{ri}} = 0 \,, \tag{3.45}$$

where K_r^{aq} is the equilibrium constant for the r-th aqueous reaction. Equation (3.45) can be written in a more convenient form as

$$\log K_r^{aq} + \nu_{ri} \log c_i = 0 \,. \tag{3.46}$$

Therefore, the molar production rate for the i-th species due to aqueous reactions is the sum of the rates R_r of the reactions r to which the specie takes part:

$$R_i^{aq} = \nu_{ri} R_r^{aq} \,. \tag{3.47}$$

3.8.3 Precipitation/Dissolution reactions

In this work only reactions where ions react to form a solid precipitate of a single mineral species or where a mineral species dissolves into its constituent ions will be taken into account. Under this assumption the r-th precipitation/dissolution reaction refers to the m-th mineral specie. The reaction can be written as

$$\bar{A}_m \rightleftharpoons \nu_{mi} A_i \,, \tag{3.48}$$

where $\bar{A}_m$ denotes the chemical symbol of the m-th mineral specie and ν_{mi} is the stechiometric coefficient of the i-th dissolved specie in the precipitation/dissolution reaction.

Production of the precipitate will not occur until the solution is saturated. Therefore, the law of mass action is written as,

$$K_m^{sp} \geq \prod_i c_i^{\nu_{mi}}, \tag{3.49}$$

where K_m^{sp} is the solubility product equilibrium constant for mineral m. Following the same previous formulations, the total rate of production of component i due to

precipitation/dissolution reactions, R_i^{pd}, reads,

$$R_i^{pd} = \sum_{m=1}^{N_m} v_{mi} R_m^{pd} \ , \tag{3.50}$$

where R_m^{pd} is the rate of production of mineral m.

3.9 Preservation of electrical neutrality

Electroneutrality is preserved considering mass flow and mass balance of each chemical species (Eqs. 3.18 and 3.29) and transport and balance of electric charge (Eqs. 3.24 and 3.37).

For a unit volume of soil, the rate of change in the electric charge equals the total rate of change of chemical species concentrations multiplied by their charge and Faraday's constant. Preservation of electrical neutrality requires that the total change in electric charge per unit volume equals zero:

$$\sum_i z_i F \frac{\partial n Src_i}{\partial t} = 0 \ . \tag{3.51}$$

The rate of change in the electric charge in a volume of soil is due to the change of the concentration of the chemical species:

$$\sum_i z_i F \frac{\partial n Src_i}{\partial t} = \sum_i z_i F \nabla (J_i) + \sum_i z_i F n Sr R_i \ . \tag{3.52}$$

Chemical reactions are electrically neutral if sorption and redox reactions are not taken into account:

$$\sum_i z_i R_i = 0 \ . \tag{3.53}$$

This is clear if the following chemical reaction is considered

$$A \rightleftharpoons mB^{+l} + lC^{-m} \ , \tag{3.54}$$

one mole of A will produce m moles of B^{+l} and l moles of C^{-m}. The total change in

B^{+l} concentration times its charge is m moles of $B^{+l} \cdot (+l) = ml$. The total change in C^{+m} concentration times its charge is l moles of $C^{-m} \cdot (-m) = -ml$. Therefore, the total change in each one concentration times its charge is $ml - ml = 0$.

If a fluid is electrically neutral its movement does not change the electric charge:

$$\sum_i z_i c_i v_l = 0 \,. \tag{3.55}$$

Assuming that the electric charge flux is due only to the Ohm's law and to ion diffusion, and that the electrical capacitance of the soil particles is null, the balance of electric charge becomes

$$\nabla(-\sigma^* + \sum_i z_i F J_i^d) = 0 \,. \tag{3.56}$$

Substituting Equation (3.11) and assuming that the electrical conductivity is due only to the ions in the pore soil fluid:

$$\nabla(-\sum_i F z_i u_i^* c_i \nabla\Phi - \sum_i z_i F D_i^* \nabla c_i) = 0 \,. \tag{3.57}$$

Substituting Equations (3.18), (3.53), (3.55) and (3.57) into Equation (3.52) results in

$$\sum_i z_i F \frac{\partial n S r c_i}{\partial t} = 0 \,. \tag{3.58}$$

3.10 Balance of linear momentum

The balance of linear momentum (also referred as the *Cauchy's equation of equilibrium*) reads:

$$\nabla \cdot \boldsymbol{\sigma} + \mathbf{b} = 0 \,, \tag{3.59}$$

where $\boldsymbol{\sigma}$ is the total stress tensor and $\mathbf{b}$ is the load vector.

In unsaturated conditions, soil skeleton behaviour is assumed to be governed by the *average soil skeleton stress* $\boldsymbol{\sigma} := \hat{\boldsymbol{\sigma}} + (Sr\, u_l + (1 - Sr) u_g)\boldsymbol{\delta}$, as defined by

Jommi (2000). Substituting this definition into Equation (3.59):

$$\nabla \cdot \hat{\boldsymbol{\sigma}} - \nabla(Sr\, u_l + (1 - Sr)u_g) + \mathbf{b} = 0 \,. \tag{3.60}$$

Equation (3.60) is the balance of linear momentum for an unsaturated porous medium. It is worth noting that in Equation (3.60) the second term is a genralised seepage force, accounting for the action of both the liquid and the gas phase on the solid skeleton. The generalised seepage force, together with the gravity force $\mathbf{b}$, determines the distribution of the effective stress in the porous medium.

The hypothesis of "small strain" is introduced, so that the current and the reference configurations of the material body are assumed to be coincident. Under this hypothesis the definition of strain is:

$$\boldsymbol{\varepsilon} := -\frac{1}{2}\left(\nabla \mathbf{u} + (\nabla \mathbf{u})^T\right) \,, \tag{3.61}$$

where the minus sign is due to the soil mechanics convention, where traction stresses are negative while compressive stresses are positive.

3.11 Stress–strain behaviour

Equilibrium and compatibility equations apply for all solid continua.

The equations ruling the behaviour of a specific material are called *constitutive equations*. For an elastic material the constitutive equations provide a relationship between effective stress and strain:

$$\hat{\boldsymbol{\sigma}} = \sigma(\hat{\boldsymbol{\sigma}}, \boldsymbol{\varepsilon}) \,. \tag{3.62}$$

Different constitutive equations have been proposed in the literature. The most used in soil mechanics are those based on the theory of elasticity or on the theory of plasticity. In this section only the general framework of these theories will be described. The constitutive equations used in the numerical simulations will be described in Section 6.4, after the description of the experimental results in Section 6.2.

3.11.1 Elasticity

Elasticity describes a reversible behaviour: when an elastic material is unloaded strain are totally recovered. Therefore the stress state depends only on the strain state and the constitutive equation is a one-to-one relationship, which can be inverted.

Elastic models:

- linear elasticity. First introduced by Hooke. $\hat{\boldsymbol{\sigma}} = \mathbf{D}^{el}\boldsymbol{\varepsilon}$;
- hyperelasticity (e.g. Borja et al., 1997). Definition of an elastic potential Ψ, $\hat{\boldsymbol{\sigma}} = \frac{\partial^2 \Psi}{\partial \boldsymbol{\varepsilon} \otimes \partial \boldsymbol{\varepsilon}}$;
- hypoelasticity;

Although elastic models have a simple formulation, in some cases they are able to reproduce the experimental behaviour with good accuracy.

3.11.2 Generalised plasticity

Elasto-plastic models based on critical state formulation appear to have been successful in describing many of the most important mechanical aspects of the behaviour of geomaterials because they contain features such as hardening, softening and pressure sensitivity typical in soils (Borja, 1991). The assumption that the behaviour of the soil skeleton is governed by the average soil skeleton has been introduced before. In the literature different elasto-plastic models for unsaturated soils using the average soil skeleton stress were proposed (e.g. Gallipoli et al., 2003a; Jommi and di Prisco, 1994; Romero and Jommi, 2008; Tamagnini, 2004).

In this section the framework of generalised plasticity will be described following the notation introduced by Tamagnini et al. (2002). In the framework of generalised plasticity the following assumptions are introduced:

- the material state is completely described by the (effective) stress tensor $\hat{\boldsymbol{\sigma}}$ and by a vector of *internal variables* $\mathbf{q}$, that describe the effect of strain history and *coupled variables* $\mathbf{Y}$ (e.g. temperature, chemical bonding, saturation) on material response;

- adopting a linear kinematic description, the strain rate is decomposed additively in an elastic, reversible part, $\dot{\boldsymbol{\varepsilon}}^e$, and a plastic, irreversible part, $\dot{\boldsymbol{\varepsilon}}^p$:

$$\dot{\boldsymbol{\varepsilon}} = \dot{\boldsymbol{\varepsilon}}^e + \dot{\boldsymbol{\varepsilon}}^p \ ; \tag{3.63}$$

- for all possible values of $\mathbf{q}$, the stress states $\boldsymbol{\sigma}$ is constrained to belong to the convex set

$$\mathbb{E}_\sigma := \{(\boldsymbol{\sigma}, \mathbf{q}) | f(\boldsymbol{\sigma}, \mathbf{q}) \leq 0\} \ , \tag{3.64}$$

  where f is a convex scalar function called *yield function*. The interior of $\mathbb{E}_\sigma$ is called *elastic domain*, while its boundary $\partial\mathbb{E}_\sigma$ is called *yield surface*;

- inside the elastic domain the material behave elastically:

$$\dot{\boldsymbol{\sigma}} = \mathbf{D}^{el}(\dot{\boldsymbol{\varepsilon}} - \dot{\boldsymbol{\varepsilon}}^e) \ , \tag{3.65}$$

  where $\mathbf{D}^{el}$ is the fourth-order elastic stiffness tensor;

- plastic strains are defined prescribing a general non associated flow rule

$$\dot{\boldsymbol{\varepsilon}}^p = \dot{\lambda}\mathbf{Q} \ , \qquad \mathbf{Q} := \frac{\partial g}{\partial \boldsymbol{\sigma}}, \tag{3.66}$$

  where $g(\boldsymbol{\sigma}, \mathbf{q})$ is a scalar function called *plastic potential* and λ is a non-negative scalar called *plastic multiplier*. The plastic multiplier must satisfy the *Kuhn-Tucker conditions*:

$$\dot{\lambda} \geq 0 \ , \qquad f(\boldsymbol{\sigma}, \mathbf{q}) \leq 0 \ , \qquad \dot{\lambda} f(\boldsymbol{\sigma}, \mathbf{q}) = 0 \ , \tag{3.67}$$

  stating that plastic deformations may occur only for states on the yield surface. In addition to the Khun-Tucker condditions, the plastic multiplier must satisfy the *consistency condition*

$$\dot{\lambda}\dot{f}(\boldsymbol{\sigma}, \mathbf{q}) = 0 \ , \tag{3.68}$$

  which forces the state of the material to lie on the yield surface when plastic loading occurs ($\dot{f} = 0$ if $\dot{\lambda} > 0$).

- the evolution of the internal variables $\mathbf{q}$ is provided by the following *generalised hardening law*:

$$\dot{\mathbf{q}} = \dot{\lambda}\mathbf{h}(\boldsymbol{\sigma}, \mathbf{q}, \mathbf{Y}) + \dot{\mathbf{Y}}\boldsymbol{\eta}(\boldsymbol{\sigma}, \mathbf{q}, \mathbf{Y}) \ , \tag{3.69}$$

  where $\mathbf{h}$ and $\boldsymbol{\eta}(\boldsymbol{\sigma}, \mathbf{q})$ are *hardening functions* of the state of the material and of the variables $\mathbf{Y}$. The hardening functions are also independent from plastic strains.

According to Equations (3.63), (3.66), (3.67) and (3.69), the evolution of the state variables $(\boldsymbol{\sigma}, \mathbf{q})$ is governed by the following system of ordinary equations:

$$\dot{\boldsymbol{\sigma}} = \mathbf{D}^{el}\left(\dot{\boldsymbol{\varepsilon}} - \dot{\lambda}\frac{\partial g}{\partial \boldsymbol{\sigma}}\right) \tag{3.70a}$$

$$\dot{\mathbf{q}} = \dot{\lambda}\mathbf{h}(\boldsymbol{\sigma}, \mathbf{q}, \mathbf{Y}) + \dot{\mathbf{Y}}\boldsymbol{\eta}(\boldsymbol{\sigma}, \mathbf{q}, \mathbf{Y}) \tag{3.70b}$$

From the consistency condition $\dot{\lambda}\dot{f} = 0$, the constitutive Equation (3.65) and the flow rule (3.66), the following expression for the plastic multiplier in terms of $\dot{\boldsymbol{\varepsilon}}$ is obtained:

$$\dot{\lambda} = \frac{1}{K_p}\left\langle \frac{\partial f}{\partial \boldsymbol{\sigma}} \cdot \mathbf{D}^{el}\dot{\boldsymbol{\varepsilon}} + \left(\frac{\partial f}{\partial \mathbf{q}} \cdot \boldsymbol{\eta}\right)\dot{\mathbf{Y}} \right\rangle \ , \tag{3.71}$$

where $\langle x \rangle := (x + |x|)/2$ is the ramp function, provided that:

$$K_p := \frac{\partial f}{\partial \boldsymbol{\sigma}} \cdot \mathbf{D}^{e}\frac{\partial g}{\partial \boldsymbol{\sigma}} - \frac{\partial f}{\partial \mathbf{q}} \cdot \mathbf{h} > 0. \tag{3.72}$$

4

Numerical integration of elastic–plastic hydro–mechanical constitutive laws for unsaturated soils

Due to high non-linearity of the constitutive behaviour of soils subjected to the coupled action of mechanical, hydraulic, electric and chemical actions, elasto-plasticity with generalised hardening is often mandatory for the analysis of problems at the finite scale. Numerical tools are already mandatory to integrate these laws along typical experimental path. Elastoplastic constitutive model for unsaturated soils presents strong coupling between hydraulic and mechanical behaviour and involves high non-linearities.

In this Chapter a driver for the numerical integration of elastic–plastic hydro–mechanical constitutive laws for unsaturated soils at the representative volume element level will be presented. The formulation of the numerical driver is conceived to allow for a straightforward implementation of the routines developed for the integration of the non linear constitutive laws into classical finite element codes. The most common schemes of the integration routine are also reviewed.

4.1 Integration of Unsaturated load paths

In geotechnical laboratory testing, stress $\boldsymbol{\sigma}$ and strain $\boldsymbol{\varepsilon}$ (derived from imposed forces and displacements) may be the mechanical control variables. As for the fluid phases, mass, m_w and m_a, or pressure, u_l and u_g, variations can be imposed. Any combination of the previous quantities may characterise a specific laboratory test. From the numerical viewpoint, a standard integration procedure would imply possible mixed control of static ($\boldsymbol{\sigma}$, u_l, u_g) and kinematic ($\boldsymbol{\varepsilon}$, m_w, m_a) variables. Partitioning consequently the constitutive matrix would lead to a "direct" formulation for the unknown variables of the specific problem under consideration. As the driver was conceived to test integration routines ready for their implementation in typical finite elements codes, where displacements and fluid pressures are adopted as primary variables, a strain-pressure driven approach was preferred. Therefore, the input variables for the integration routines are always strain and fluid pressure increments, for any loading path. The final values of fluid masses and stresses are the dependent variables to be found iteratively.

Let vector $\mathbf{c}$ collect the controlling (driving) variables and vector $\mathbf{s}$ the dependent ones:

$$\mathbf{c} := \begin{bmatrix} \boldsymbol{\varepsilon} \\ u_l \\ u_g \end{bmatrix} \qquad \mathbf{s} := \begin{bmatrix} \boldsymbol{\sigma} \\ m_w \\ m_a \end{bmatrix} , \tag{4.1a, b}$$

and let $n+1$ be a time step bounded by t_n and t_{n+1}. Both driving and dependent variables, $\mathbf{c}$ and $\mathbf{s}$, are assumed to be completely known at time t_n. The system of equations describing the generic laboratory constraints during the time step $n+1$ can be formally written as Bardet and Choucair (1991):

$$\boldsymbol{\Sigma}\Delta\mathbf{s} + \boldsymbol{\Gamma}\Delta\mathbf{c} = \Delta\bar{\mathbf{V}} . \tag{4.2}$$

Matrices $\boldsymbol{\Gamma}$ and $\boldsymbol{\Sigma}$ are constant during the load path, and can be partitioned as:

$$\boldsymbol{\Gamma} := \begin{bmatrix} \mathsf{E} & 0 & 0 \\ 0 & \Gamma_l & 0 \\ 0 & 0 & \Gamma_g \end{bmatrix} \qquad \boldsymbol{\Sigma} := \begin{bmatrix} \mathsf{S} & 0 & 0 \\ 0 & \Sigma_w & 0 \\ 0 & 0 & \Sigma_a \end{bmatrix} . \tag{4.3}$$

Matrices $\mathbf{E}$ and $\mathbf{S}$ define the mechanical constraints of the test in the same way as proposed by Bardet and Choucair (1991), but involving total stress instead of effective stress. The other non-zero terms refer to fluid phases: for example, if the pressure of the liquid phase is imposed $\Gamma_l = 1$ and $\Sigma_w = 0$, while if the water mass increment is imposed $\Sigma_w = 1$ and $\Gamma_l = 0$. The constraints for the gas phase, Γ_g and Σ_a, are defined in similar way.

In unsaturated soil mechanics different constitutive stresses maybe adopted in the formulation of constitutive laws. Imposing the mechanical constraints on total stress and adopting an explicit formulation for the constraints on the fluid phases make the driver able to handle different choices for constitutive stresses.

4.1.1 Soil behaviour

As said before, the formulation proposed is able to integrate models for unsaturated soils defined in terms of any constitutive stress variables, provided they were written as a function of total stress, fluid pressures and degree of saturation:

$$\tilde{\boldsymbol{\sigma}}_k := f_k\left(\boldsymbol{\sigma}, u_l, u_g, Sr\right) \qquad k = 1, \cdots, m \ , \tag{4.4}$$

where $\tilde{\boldsymbol{\sigma}}_k$ is one of the m constitutive stresses adopted by the model chosen.

In Paragraph 3.10 it has been assumed that the *average soil skeleton stress* $\hat{\sigma}_{ij} := (\sigma_{ij} - u_g\delta_{ij}) + Sr(u_g - u_l)\delta_{ij}$ (Jommi, 2000) may be adopted as a convenient constitutive stress. So the total stress increment could be written as:

$$\Delta\sigma_{ij} = \sigma_{ij}^{n+1} - \sigma_{ij}^{n} = \hat{\sigma}_{ij}^{n+1} + (Sr^{n+1}u_l^{n+1} + (1 - Sr^{n+1})u_g^{n+1})\delta_{ij} - \sigma_{ij}^{n} \ . \tag{4.5}$$

Equation (4.5) contains the effective stress at the end of the increment, $\hat{\boldsymbol{\sigma}}^{n+1}$, which can be calculated by one of the integration algorithms presented in the literature (Borja and Lee, 1990; Sloan, 1987, e.g.). A review of the most common integration algorithms is presented in Section 4.2.

In Paragraph 3.7 the properties of the water retention curve were reviewed. According to most of the models for water retention curve proposed in the literature (Gallipoli et al., 2003b; Nuth and Laloui, 2008; Romero et al., 2011, e.g.), the degree of saturation at the end of the step and its increment in the step depend on the

pressure of the fluid phases, u_l and u_g, and on the void ratio e:

$$Sr^{n+1} = Sr(Sr^n, \Delta u_g, \Delta u_l, \Delta \boldsymbol{\varepsilon}) \tag{4.6a}$$

$$\Delta Sr = Sr^{n+1} - Sr^n \ . \tag{4.6b}$$

4.1.2 Water mass balance

The mass balance of water were discussed in Paragraph 3.6.1. Neglecting water in the gaseous phase, the water mass contained in the volume element of unsaturated soil is

$$m_w = nSr\rho_w \ . \tag{4.7}$$

The corresponding increment is:

$$\Delta m_w = n^{n+1} Sr^{n+1} \rho_w^{n+1} - m_w^n \ , \tag{4.8}$$

which is a function only of the driving variables taking into account that the density of water ρ_w depends on the liquid pressure:

$$\rho_w^{n+1} = \rho_{w0} \exp\left(\frac{u_l^{n+1} - u_{l0}}{B_w} \right) , \tag{4.9}$$

where th subscript 0 denotes the reference state.

4.1.3 Air mass balance

Taking into account that in the pores air is present both in the gaseous and in the liquid phase (consider air as a unique chemical species, for details see Paragraph 3.6.2), the total air mass is:

$$m_a = (1 - (1 - h)Sr)n\rho_a \ , \tag{4.10}$$

and its increment reads:

$$\Delta m_a = (1 - (1 - h)Sr^{n+1})n^{n+1}\rho_a^{n+1} - m_a^n \ , \tag{4.11}$$

where the air density is

$$\rho_a^{n+1} = \rho_{a0} \frac{u_g^{n+1} + p_{atm}}{u_{g0} + p_{atm}} \,. \tag{4.12}$$

If the atmospheric pressure is adopted as reference state, Equation (4.12) becomes

$$\rho_a^{n+1} = \rho_{a0} \frac{u_g^{n+1} + p_{atm}}{p_{atm}} \,. \tag{4.13}$$

4.1.4 Solution strategy

Substituting Equations (4.5), (4.8) and (4.11) in Equation (4.2), the system of governing non-linear equations is obtained, which can be solved by Newton's method. Newton's method provides quadratic convergence rate, if the initial guess $\mathbf{x}_0$ is sufficiently close to the solution $\mathbf{x}^*$ and the Jacobian matrix is not singular (Quarteroni et al., 2007). The solution at the end of the step $n+1$ is found by iteration, starting from an initial guess $\mathbf{c}^0 = 0$ until the theoretical condition $\mathbf{R} = 0$ is reached, according to Algorithm 4.1 .

Algorithm 4.1: Solution procedure of the equation at the point volume

1. SET $i = 0$ and $\Delta \mathbf{c}^i = \mathbf{0}$
2. REPEAT
3. COMPUTE increment of the degree of saturation

$$Sr^{n+1,i} = Sr(u_w^{n+1,i} - u_a^{n+1,i}, \Delta\boldsymbol{\varepsilon}^i) \qquad \Delta Sr^i = Sr^{n+1,i} - Sr^n$$

4. COMPUTE effective stresses $\hat{\boldsymbol{\sigma}}^{n+1,i} = f(\Delta\boldsymbol{\varepsilon}^i, \Delta Sr^i)$
5. COMPUTE fluid phase densities

$$\rho_w^{n+1,i} = \rho_w^0 \exp\left(\frac{u_l^{n+1,i} - u_l^0}{B_w}\right) \qquad \rho_a^{n+1,i} = \rho_a^0 \frac{u_g^{n+1,i} + p_{atm}}{u_g^0 + p_{atm}} \,.$$

6. Static variables increment is calculated

$$\Delta\boldsymbol{\sigma}^{n+1,i} = \Delta\hat{\boldsymbol{\sigma}}^{n+1,i} + (Sr_n \Delta u_w^{n+1,i} + (1 - Sr^n)\Delta u_a^{n+1,i} - (u_a^n - u_w^n)\Delta Sr^i)\mathbf{1}$$

$$\Delta m_w = n^{n+1,i} Sr^{n+1,i} \rho_w^{n+1,i} - m_w^n$$

$$\Delta m_a = (1-(1-h)Sr^{n+1,i})n^{n+1,i}\rho_a^{n+1,i} - m_a^n \ .$$

7. update kinematic variables

$$\Delta \mathbf{c}^{i+1} = \Delta \mathbf{c}^i - \left(\mathbf{\Sigma} \left. \frac{\partial \Delta \mathbf{s}}{\partial \Delta \mathbf{c}} \right|^{n+1,i} + \mathbf{\Gamma} \right)^{-1} \mathbf{R} \ .$$

8. UNTIL $\mathbf{R} = \mathbf{\Sigma}\Delta \mathbf{s}^i + \mathbf{\Gamma}\Delta \mathbf{c}^i - \Delta \bar{\mathbf{V}} \neq \mathbf{0}$
9. update kinematic and static variables $\mathbf{c}^{n+1} = \mathbf{c}^n + \Delta \mathbf{c}^{n+1,i} \qquad \mathbf{s}^{n+1} = \mathbf{s}^n + \Delta \mathbf{s}^{n+1,i}$

With reference to the complete scheme, reported in the following as Algorithm 4.1, at step 7 derivatives of the static variables increment respect to the kinematic variables increments have to be evaluated:

$$\frac{\partial \Delta \mathbf{s}}{\partial \Delta \mathbf{c}} = \begin{bmatrix} \dfrac{\partial \Delta \boldsymbol{\sigma}}{\partial \Delta \boldsymbol{\varepsilon}} & \dfrac{\partial \Delta \boldsymbol{\sigma}}{\partial \Delta u_l} & \dfrac{\partial \Delta \boldsymbol{\sigma}}{\partial \Delta u_g} \\ \dfrac{\partial \Delta m_w}{\partial \Delta \boldsymbol{\varepsilon}} & \dfrac{\partial \Delta m_w}{\partial \Delta u_l} & \dfrac{\partial \Delta m_w}{\partial \Delta u_g} \\ \dfrac{\partial \Delta m_a}{\partial \Delta \boldsymbol{\varepsilon}} & \dfrac{\partial \Delta m_a}{\partial \Delta u_l} & \dfrac{\partial \Delta m_a}{\partial \Delta u_g} \end{bmatrix} . \tag{4.14}$$

Derivation of the terms in Equation (4.14) is shown in Appendix A. Note that, from Equation (4.5),

$$\frac{\partial \Delta \boldsymbol{\sigma}}{\partial \Delta \boldsymbol{\varepsilon}} = \frac{\partial \Delta \hat{\boldsymbol{\sigma}}}{\partial \Delta \boldsymbol{\varepsilon}} - s\boldsymbol{\delta}\frac{\partial \Delta Sr}{\partial \Delta \boldsymbol{\varepsilon}} \tag{4.15}$$

and, since $\hat{\boldsymbol{\sigma}}^{n+1} = \hat{\boldsymbol{\sigma}}^n + \Delta \hat{\boldsymbol{\sigma}}$, it follows that

$$\frac{\partial \Delta \hat{\boldsymbol{\sigma}}}{\partial \Delta \boldsymbol{\varepsilon}} = \frac{\partial \Delta \hat{\boldsymbol{\sigma}}}{\partial \Delta \boldsymbol{\varepsilon}} + \frac{\partial \Delta \hat{\boldsymbol{\sigma}}}{\partial \Delta Sr}\frac{\partial \Delta Sr}{\partial \Delta \boldsymbol{\varepsilon}} \ . \tag{4.16}$$

The derivatives of $\Delta \hat{\boldsymbol{\sigma}}$ with respect to $\Delta \boldsymbol{\varepsilon}$ and ΔSr are the tangent consistent moduli as defined by Simo and Taylor (1985).

Introduction of dissolved gas in Equation (4.10), besides providing a more correct description of the physical transfer mechanisms, avoids singularity of the matrix (4.14) for $Sr = 1$ (Vanuat et al., 1997). In this way the algorithm proposed is able to simulate naturally the transition from the saturated to the unsaturated condition.

It is worth noting that the structure of the routines which provide the integration of the constitutive laws (steps 3 and 4 of Solution procedure at the point volume) is the same as that adopted in the solution of boundary value problems with a classical displacement-pressure based finite element approach. Therefore, at the end of the model development stage, they can be transferred to FE codes in a straightforward way.

4.2 Integration of elasto–plastic constitutive equations

In a boundary value problem the load path is divided into step. Let $n+1$ be a time step bounded by t_n and t_{n+1}. The state of the material ($\hat{\boldsymbol{\sigma}}_n$, $\mathbf{q}_n$, $\boldsymbol{\varepsilon}_n$, $\boldsymbol{\varepsilon}^p_n$, Sr_n) is assumed to be completely known at time t_n. The unknowns $\hat{\boldsymbol{\sigma}}_{n+1}$, $\mathbf{q}_{n+1}$ and $\boldsymbol{\varepsilon}^p_{n+1}$ must be determined, given the assigned increments $\Delta\boldsymbol{\varepsilon}$ and ΔSr.

The most common approaches for the integration of elastoplastic constitutive equations (3.65)-(3.67) can be summarized as:

- explicit methods (e.g Jakobsen and Lade, 2002; Sloan, 1987; Sloan et al., 2001);
- implicit (backward Euler) methods (e.g. Borja, 2004; Borja and Lee, 1990; Tamagnini et al., 2002);
- θ-methods (e.g. Ortiz and Popov, 1985)].

Common to these algorithms is the calculation strategy based on an initial trial solution, calculated by a fully elastic prediction obtained freezing the plastic flow (i.e. $\lambda^{trial} = 0$). The trial elastic solution is checked against an initial yield surface, in which the internal variables have been already updated for degree of saturation changes.

4.2.1 Explicit method

For this class of methods, the trial elastic state is obtained with an explicit approach freezing the plastic flow and taking into account the variation of Sr. If the trial stress point is located inside the yield surface, $f^{trial} \leq 0$, the strain increment is

truly elastic and the trial stress state corresponds to the true stress state. If the Kuhn-Tucker conditions are violated, the strain increment is, totally or partially, plastic. In this case, a plastic integration step must be performed, updating the stress and the hardening parameters.

Elastic Predictor

Assuming that the step is completely elastic, the trial state is calculated with an explicit approach

$$\hat{\boldsymbol{\sigma}}_{n+1}^{trial} = \hat{\boldsymbol{\sigma}}_n + \Delta\hat{\boldsymbol{\sigma}}_{n+1}^{trial} = \hat{\boldsymbol{\sigma}}_n + \mathbf{D}^e \Delta\boldsymbol{\varepsilon} \tag{4.17a}$$

$$\mathbf{q}_{n+1}^{trial} = \mathbf{q}_n + \Delta Sr\, \boldsymbol{\eta}(\hat{\boldsymbol{\sigma}}_n, \mathbf{q}_n, Sr_n)\ . \tag{4.17b}$$

If $f_{n+1}^{trial} := f(\hat{\boldsymbol{\sigma}}_{n+1}^{trial}, \mathbf{q}_{n+1}^{trial}) \leq 0$, the trial state satisfies the Kuhn-Tucker conditions (3.67) and it coincides with the converged solution in the step. Otherwise, if $f_{n+1}^{trial} > 0$, a plastic integration step must be performed.

Intersection with yield surface

In the latter case, at the beginning of the step the stress state can be strictly inside the yield locus, i.e. $f_n < 0$. Thus the intersection with the trial yield surface must be found before starting the plastic integration step. The problem of finding the stress and the internal variables at the yield surface intersection reduces to the determination of the scalar quantity α which satisfies the equation

$$f(\hat{\boldsymbol{\sigma}}_n + \alpha \mathbf{D}^e \Delta\boldsymbol{\varepsilon}, \mathbf{q}_n + \alpha \Delta Sr\boldsymbol{\eta}) = 0\ . \tag{4.18}$$

A value of $\alpha = 0$ indicates that $f_n = 0$ at the beginning of the step, while $\alpha = 1$ means that the step is purely elastic.

Note the role of the increment of degree of saturation into the calculation of the intersection with the yield surface. Consider the case where the strain increment is zero while the degree of saturation increment reduces the yielding surface, so that the stress point state will eventually fall outside (Figure 4.1). In this case a part of the increment, such that stress lies on the yield surface, does not produce plastic strain. The elastic part of the increment is the same for strain and degree

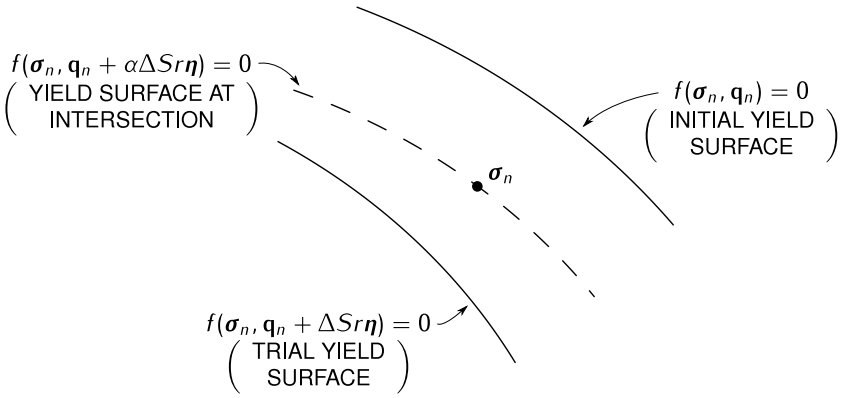

Figure 4.1: Intersection due to degree of saturation.

of saturation (Figure 4.2).

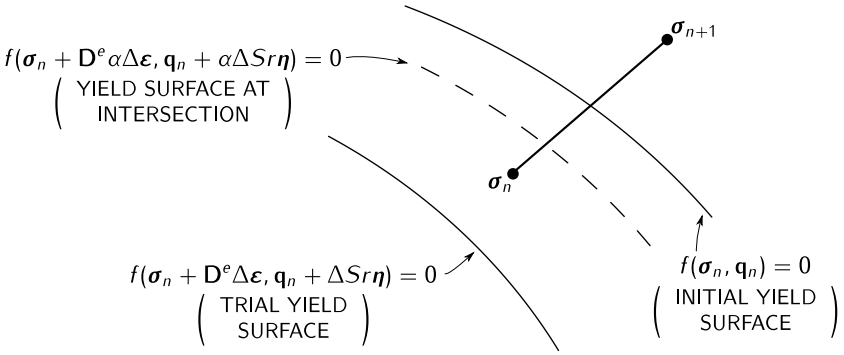

Figure 4.2: Intersection with yield surface.

In general, Equation (4.18) is non-linear with respect to the variable α and can be solved by several numerical methods, e.g. bisection, Regula-falsi, secant and Newton-Raphson. The former two algorithms are unconditionally convergent and confine the solution to lie within a specified interval, that in this case is $0 < \alpha < 1$. Secant and Newton-Raphson schemes have a more rapid convergence rate than bisection and regula-falsi, but the absence of any constraint for α can cause divergence of the method. In this work the Regula-falsi method has been adopted. It proceeds by producing a sequence of shrinking intervals that all contain the zero of the function and, despite of computational cost similar to the secant method, it is characterised by a linear convergence rate (Quarteroni et al., 2007). The Regula-falsi algorithm used to solve Equation (4.18) is detailed in Algorithm 4.2 .

Algorithm 4.2: Regula-Falsi scheme for finding the yield point.

1. SET $j = 0$, $BOT^0 = 0 \rightarrow F^0_{BOT} = f(\hat{\boldsymbol{\sigma}}_n, \mathbf{q}_n)$, $UPP^0 = 1 \rightarrow F^0_{UPP} = f(\hat{\boldsymbol{\sigma}}^{trial}_{n+1}, \mathbf{q}^{trial}_{n+1})$
2. REPEAT
3. COMPUTE α^j as
$$\alpha^j = \frac{UPP^j \cdot F^j_{BOT} - BOT^j \cdot F^j_{UPP}}{F^j_{BOT} - F^j_{UPP}} .$$
4. COMPUTE the yield function $f^j = f(\hat{\boldsymbol{\sigma}}_n + \mathbf{D}^e \alpha^j \Delta\boldsymbol{\varepsilon}, \mathbf{q}_n + \alpha^j \Delta S r \boldsymbol{\eta})$
5. IF $F^j_{BOT} \cdot f^j > 0$ THEN
6. $BOT^{j+1} = \alpha^j \quad \rightarrow \quad F^{j+1}_{BOT} = f^j$
7. $UPP^{j+1} = UPP^j$
8. ELSE
9. $BOT^{j+1} = \alpha^j \quad \rightarrow \quad F^{j+1}_{BOT} = f^j$
10. $UPP^{j+1} = BOT^j \quad \rightarrow \quad F^{j+1}_{UPP} = F^j_{BOT}$
11. UNTIL $f^j = 0$

Plastic integration step

Stress and internal variables on the yield surface become the initial values at the beginning of the plastic integration step, which consists in solving the non-linear system of ordinary differential equations (3.65) and (3.69). The strain and degree of saturation increments to consider in this step are

$$\begin{aligned} \Delta\boldsymbol{\varepsilon}^{ep} &:= (1-\alpha)\Delta\boldsymbol{\varepsilon} \\ \Delta S r^{ep} &:= (1-\alpha)\Delta S r \end{aligned} . \tag{4.19}$$

Several methods have been proposed to integrate the non linear constitutive laws. All of them require a sub-stepping procedure, to limit the integration error. Among them, the algorithms belonging to the Runge-Kutta's class, with automatic substepping and error control, have proven to be reliable and efficient (Sloan et al., 2001). The basic idea of this class of algorithms is to modify the substep size by comparing two different order estimates of the problem solution. The Runge-Kutta-Dormand-Prince algorithm was chosen here. The procedure outlined in Algorithm 4.3 was implemented to integrate the plastic step.

Algorithm 4.3: Plastic extension

1. SET pseudo-time $T = 0$
2. REPEAT
3. $\Delta T = 1 - T$.
4. REPEAT
5. FOR $i = 1$ to p DO
6. COMPUTE stresses and internal variables of the stage i

$$\hat{\boldsymbol{\sigma}}^i = \hat{\boldsymbol{\sigma}}_n + \sum_{k=0}^{i-1} \beta_{ik} \Delta \hat{\boldsymbol{\sigma}}^k \qquad \mathbf{q}^i = \mathbf{q}_n + \sum_{k=0}^{i-1} \beta_{ik} \Delta \mathbf{q}^k$$

7. COMPUTE plastic multiplier $\Delta\lambda^{i+1}$

$$\Delta\lambda^{i+1} = \frac{1}{K_p}(\mathbf{P} \cdot \mathbf{D}^e \Delta T \Delta \boldsymbol{\varepsilon}^{ep} + \mathbf{W}\boldsymbol{\eta} \Delta T \Delta S r^{ep}) \quad \text{with} \quad K_p = \mathbf{P} \cdot \mathbf{D}^e \Delta T \mathbf{Q} - \mathbf{W}\mathbf{h}$$

where $\mathbf{P}$,$\mathbf{D}^e$,$\mathbf{W}$,$\boldsymbol{\eta}$ and $\mathbf{h}$ are evaluated using $\hat{\boldsymbol{\sigma}}^i$ and $\mathbf{q}^i$.

8. $\Delta\hat{\boldsymbol{\sigma}}^{i+1} = \mathbf{D}^e(\Delta T \Delta \boldsymbol{\varepsilon}^{ep} - \Delta\lambda^{i+1}\mathbf{Q})$
9. $\Delta\mathbf{q}^{n+1} = \Delta\lambda^{i+1}\mathbf{h} + \Delta T \Delta S r^{ep}\boldsymbol{\eta}$
10. COMPUTE stresses of the two RK methods: $\tilde{\hat{\boldsymbol{\sigma}}}_{n+1} = \hat{\boldsymbol{\sigma}}_n + c_i \Delta\hat{\boldsymbol{\sigma}}^i$, $\bar{\hat{\boldsymbol{\sigma}}}_{n+1} = \hat{\boldsymbol{\sigma}}_n + \bar{c}_i \Delta\hat{\boldsymbol{\sigma}}^i$
11. COMPUTE internal variables of the two RK methods: $\tilde{\mathbf{q}}_{n+1} = \mathbf{q}_n + c_i \Delta\mathbf{q}^i$, $\bar{\mathbf{q}}_{n+1} = \mathbf{q}_n + \bar{c}_i \Delta\mathbf{q}^i$
12. COMPUTE relative error:

$$\xi = \max_j \left(\frac{\|\tilde{\hat{\boldsymbol{\sigma}}}_{n+1} - \bar{\hat{\boldsymbol{\sigma}}}_{n+1}\|}{\|\tilde{\hat{\boldsymbol{\sigma}}}_{n+1}\|}, \frac{|\tilde{q}^j_{n+1} - \bar{q}^{n+1}_j|}{|\tilde{q}^j_{n+1}|} \right)$$

13.

$$\Delta T = \Delta T \cdot 0.9 \left(\frac{\xi}{TOL} \right)^{1/p}$$

14. UNTIL $\xi < TOL$
15. $\hat{\boldsymbol{\sigma}}_{n+1} = \tilde{\hat{\boldsymbol{\sigma}}}_{n+1}$
16. $\mathbf{q}_{n+1} = \tilde{\mathbf{q}}_{n+1}$
17. $Sr_{n+1} = Sr_n + \Delta T \Delta S r^{ep}$

18. $T = T + \Delta T$
19. Check if the stress state lie on the yield surface. If not, a yield surface drift correction is necessary.
20. `UNTIL` $T \neq 1$

Tables 4.1 and 4.2 report the Butcher's matrices for the Runge-Kutta-Fehlberg and the Runge-Kutta-Dormand-Prince methods, respectively.

Table 4.1: Butcher's matrix for Runge-Kutta-Fehlberg method (Stoer and Bulirsch, 2002).

k	β_{k0}	β_{k1}	β_{k2}	c_k	$\bar{c}_k$
0	-	-	-	$\frac{214}{891}$	$\frac{533}{2106}$
1	$\frac{1}{4}$	-	-	$\frac{1}{33}$	0
2	$-\frac{189}{800}$	$\frac{729}{800}$	-	$\frac{650}{891}$	$\frac{800}{1053}$
3	$\frac{214}{891}$	$\frac{1}{33}$	$\frac{650}{891}$	-	$-\frac{1}{78}$

Correction for yield surface drift

When an explicit algorithm is adopted, the plastic extension does not force the stress state to lie on the yield surface. The constraint $f_{n+1} = 0$ has to be checked at the end of the integration step, and, in the case it is violated, consistency must be restored. There are several methods that can be adopted to this aim (e.g. Jakobsen and Lade, 2002; Sloan, 1987).

Due to its simplicity, a slight modification of the method proposed by Sloan (1987) has been adopted. With reference to Figure 4.3, the point B indicates the state of the material at the end of the plastic explicit integration, that is not necessarily located on the yield surface $f(\hat{\boldsymbol{\sigma}}_B, \mathbf{q}_B) = 0$. Point C represents the state of the material after the correction. The final stress state is modified in order to restore the consistency condition assuming that the internal variables $\mathbf{q}_B$ remain constant during the correction process. In order to obtain a direction consistent to

Table 4.2: Butcher's matrix for Runge-Kutta-Dormand-Prince method (Sloan et al., 2001).

k	β_{k0}	β_{k1}	β_{k2}	β_{k3}	β_{k4}	c_k	$\bar{c}_k$
0	-	-	-	-	-	$\frac{31}{540}$	$\frac{19}{216}$
1	$\frac{1}{5}$	-	-	-	-	0	0
2	$\frac{3}{40}$	$\frac{9}{40}$	-	-	-	$\frac{190}{297}$	$\frac{1000}{2079}$
3	$\frac{3}{10}$	$-\frac{9}{10}$	$\frac{6}{5}$	-	-	$-\frac{145}{108}$	$-\frac{125}{216}$
4	$\frac{226}{72}$	$-\frac{25}{27}$	$\frac{880}{729}$	$\frac{55}{729}$	-	$\frac{351}{220}$	$\frac{81}{88}$
5	$-\frac{181}{270}$	$\frac{5}{2}$	$-\frac{266}{297}$	$-\frac{91}{27}$	$\frac{189}{55}$	$\frac{1}{20}$	$\frac{5}{56}$

the previous plastic deformation, the correction is applied along a direction which is normal to the plastic potential. To this aim, a scalar β can be found so that

$$f(\hat{\boldsymbol{\sigma}}_C, \mathbf{q}_B) = 0\,, \qquad \hat{\boldsymbol{\sigma}}_C = \hat{\boldsymbol{\sigma}}_B + \beta \left.\frac{\partial g}{\partial \hat{\boldsymbol{\sigma}}}\right|_B\,, \tag{4.20}$$

where $\hat{\boldsymbol{\sigma}}_B$ is the stress state at the end of the explicit integration procedure, and $\hat{\boldsymbol{\sigma}}_C$ is the final corrected stress state, satisfying the consistency condition, for the given internal variables. Equations (4.20) define a single non-linear equation of the form $F(\beta) = 0$, that may be solved iteratively. Since there is not a known interval where β lies, Regula-falsi method can not applied. Therefore a Newton-Raphson strategy has been adopted.

4.2.2 Implicit method

Following Tamagnini et al. (2002), the classical elastic–plastic operator split (Borja and Lee, 1990) of the original problem (OR) may be extended to generalised hardening rules, dependent on both the plastic strains and the degree of saturation, as the sum of an elastic predictor (EP) and a plastic corrector (PC):

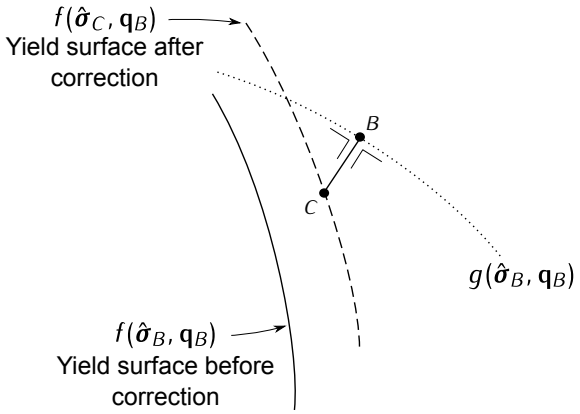

Figure 4.3: Sloan correction.

OR	=	EP	+	PC
$\dot{\boldsymbol{\varepsilon}}^e = \dot{\boldsymbol{\varepsilon}}^{tot} - \dot{\lambda}\mathbf{Q}$		$\dot{\boldsymbol{\varepsilon}}^e = \dot{\boldsymbol{\varepsilon}}^{tot}$		$\dot{\boldsymbol{\varepsilon}}^e = -\dot{\lambda}\mathbf{Q}$
$\dot{\mathbf{q}} = \dot{\lambda}\mathbf{h} + \dot{S}r\boldsymbol{\eta}$		$\dot{\mathbf{q}} = \dot{S}r\boldsymbol{\eta}$		$\dot{\mathbf{q}} = \dot{\lambda}\mathbf{h}$

First, the elastic-plastic predictor problem is solved and a trial elastic state is obtained. Then, the constraint $f^{trial} \leq 0$ is checked, and if it is violated, the trial state is taken as the initial condition for the plastic corrector problem. Otherwise the trial state coincides with the converged solution in the step.

Elastic predictor

Like in explicit methods, the first stage is to predict an elastic trial solution. Trial values are calculated solving the elastic predictor problem:

$$\hat{\boldsymbol{\sigma}}^{trial}_{n+1} = \sigma(\hat{\boldsymbol{\sigma}}_n, \Delta\boldsymbol{\varepsilon}^{tot}) \tag{4.21a}$$

$$\mathbf{q}^{trial}_{n+1} = \mathbf{q}_n + \Delta Sr\boldsymbol{\eta}(\hat{\boldsymbol{\sigma}}^{trial}_{n+1}, \mathbf{q}^{trial}_{n+1}(Sr_{n+1})). \tag{4.21b}$$

Equation (4.21b) must be solved by iteration, and a suitable accurate procedure must be envisaged, as the accuracy of the elastic prediction affects significantly the final accuracy of the integration, as the results presented in the following will demonstrate. A closed form evaluation of $\mathbf{q}^{trial}_{n+1}$ is strongly suggested, when the function $\boldsymbol{\eta}$ is sufficiently simple to be integrated analytically, especially for large increments of the degree of saturation.

Plastic corrector

If $f_{n+1}^{trial} > 0$ the trial state lies outside the yield locus, and consistency needs to be restored. As mentioned before the trial state is the initial condition for the following system:

$$\begin{cases} \Delta\boldsymbol{\varepsilon}^{e} = \Delta\boldsymbol{\varepsilon}^{tot} - \Delta\lambda_{n+1} \left.\dfrac{\partial g}{\partial \hat{\boldsymbol{\sigma}}}\right|_{n+1} \\ \mathbf{q}_{n+1} = \mathbf{q}_{n+1}^{trial} + \Delta\lambda_{n+1}\mathbf{h}(\hat{\boldsymbol{\sigma}}_{n+1}, \mathbf{q}_{n+1}) \\ f(\hat{\boldsymbol{\sigma}}_{n+1}, \mathbf{q}_{n+1}) = 0 \end{cases} \tag{4.22}$$

where the unknowns are $\Delta\boldsymbol{\varepsilon}^{e}$, $\mathbf{q}_{n+1}$ and $\Delta\lambda_{n+1}$. The system (4.22) is non-linear and is solved via Newton's method (Algorithm 4.4).

Algorithm 4.4: Newton's method for plastic correction

1. $i = 0$: $\Delta\boldsymbol{\varepsilon}^{e,0} = \Delta\boldsymbol{\varepsilon}^{tot}, \quad \mathbf{q}^{0} = \mathbf{q}_{n+1}^{trial}, \quad \Delta\lambda_{n+1}^{0} = 0$
2. `REPEAT`
3. $\hat{\boldsymbol{\sigma}}_{n+1}^{i} = \hat{\boldsymbol{\sigma}}_{n} + \mathbf{D}^{e}\Delta\boldsymbol{\varepsilon}^{e,i}$
4. $\mathbf{R}_{\varepsilon}^{i} = \Delta\boldsymbol{\varepsilon}^{tot} - (\Delta\boldsymbol{\varepsilon}^{e,i} + \Delta\lambda_{n+1}^{i} \left.\dfrac{\partial g}{\partial \hat{\boldsymbol{\sigma}}}\right|_{n+1}^{i})$
5. $\mathbf{R}_{q}^{i} = \mathbf{q}_{n+1}^{trial} + \Delta\lambda_{n+1}^{i}\mathbf{h}(\hat{\boldsymbol{\sigma}}_{n+1}^{i}, \mathbf{q}_{n+1}^{i}) - \mathbf{q}_{n+1}^{i}$
6. $f^{i} = f(\hat{\boldsymbol{\sigma}}_{n+1}^{i}, \mathbf{q}_{n+1}^{i})$
7. Find update at iteration i

$$\delta\mathbf{x}^{i} = -\left[\left.\frac{\partial \mathbf{R}}{\partial \mathbf{x}}\right|^{i}\right]^{-1}\mathbf{R}^{i}$$

8. Update state variables and plastic multiplier

$$\mathbf{x}^{i+1} = \mathbf{x}^{i} + \delta\mathbf{x}^{i}$$

9. `UNTIL` $\|\mathbf{R}_{\varepsilon}^{i}\| < TOL \cdot \left\|\boldsymbol{\varepsilon}^{e,trial}\right\|$, $\left\|\mathbf{R}_{q}^{i}\right\| < TOL \cdot \left\|\mathbf{q}^{trial}\right\|$, $f^{i} < TOL$

Step 7 of Algorithm 4.4 requires the solution of a linear system. However, by observing that the last equation (the constraint condition) of the solving system (4.22) does not depend directly on the plastic multiplier λ, the linear system of

equation to be solved can be reduced in size via static condensation. Let:

$$\mathbf{x}_{n+1} := \left\{ \begin{array}{c} \Delta\boldsymbol{\varepsilon}^e \\ \mathbf{q}_{n+1} \\ \Delta\lambda_{n+1} \end{array} \right\} := \left\{ \begin{array}{c} \tilde{\mathbf{x}}_{n+1} \\ \Delta\lambda_{n+1} \end{array} \right\} \tag{4.23}$$

The residual vector at the iteration i is partitioned like the unknowns and is defined as:

$$\mathbf{R}^i := \left\{ \begin{array}{c} \mathbf{R}^i_\varepsilon \\ \mathbf{R}^i_q \\ f^i_{n+1} \end{array} \right\} := \left\{ \begin{array}{c} \Delta\boldsymbol{\varepsilon}^{tot} - \Delta\lambda^i_{n+1} \left.\dfrac{\partial g}{\partial \hat{\boldsymbol{\sigma}}}\right|^i_{n+1} - \Delta\boldsymbol{\varepsilon}^{e,i} \\ \mathbf{q}^i_{n+1} - \mathbf{q}^{trial}_{n+1} - \Delta\lambda^i_{n+1}\mathbf{h}(\hat{\boldsymbol{\sigma}}^i_{n+1}, \mathbf{q}^i_{n+1}) \\ f^i_{n+1} \end{array} \right\} := \left\{ \begin{array}{c} \tilde{\mathbf{R}}^i \\ f^i_{n+1} \end{array} \right\} \tag{4.24}$$

the tangent operator can be evaluated as

$$\frac{\partial \mathbf{R}}{\partial \mathbf{x}} := \left[\begin{array}{cc} -\mathbf{A} & -\mathbf{U} \\ \mathbf{V} & 0 \end{array} \right] \tag{4.25}$$

where

$$\mathbf{A} := \left[\begin{array}{cc} \mathbf{I} + \Delta\lambda \dfrac{\partial^2 g}{\partial\hat{\boldsymbol{\sigma}}\partial\hat{\boldsymbol{\sigma}}}\mathbf{D}^e & \Delta\lambda \dfrac{\partial^2 g}{\partial\hat{\boldsymbol{\sigma}}\partial\mathbf{q}} \\ \Delta\lambda \dfrac{\partial \mathbf{h}}{\partial\hat{\boldsymbol{\sigma}}}\mathbf{D}^e & -\mathbf{I} + \Delta\lambda \dfrac{\partial \mathbf{h}}{\partial\mathbf{q}} \end{array} \right] \tag{4.26}$$

$$\mathbf{U} := \left[\begin{array}{c} \dfrac{\partial g}{\partial\hat{\boldsymbol{\sigma}}} \\ \mathbf{h} \end{array} \right] \tag{4.27}$$

$$\mathbf{V} := \left[\begin{array}{cc} \dfrac{\partial f}{\partial\hat{\boldsymbol{\sigma}}}\mathbf{D}^e & \dfrac{\partial f}{\partial\mathbf{q}} \end{array} \right] \tag{4.28}$$

Due to the zero in (4.25) the system at iteration i can be rewritten as

$$\mathbf{A}^i_{n+1}\delta\tilde{\mathbf{x}}^i_{n+1} + \mathbf{U}^i_{n+1}\delta\Delta\lambda^i_{n+1} = \tilde{\mathbf{R}}^i_{n+1} \tag{4.29a}$$

$$\mathbf{V}^i_{n+1}\delta\tilde{\mathbf{x}}^i_{n+1} = -f^i_{n+1} \tag{4.29b}$$

that can be solved in two stages. First Equation (4.29a) is solved for $\delta\tilde{\mathbf{x}}^i_{n+1}$

$$\delta\tilde{\mathbf{x}}^i_{n+1} = (\mathbf{A}^i_{n+1})^{-1}\left(\tilde{\mathbf{x}}^i_{n+1} - \mathbf{U}^i_{n+1}\delta\Delta\lambda^i_{n+1}\right) \tag{4.30}$$

substituting in Equation (4.29b) the change in plastic multiplier is

$$\delta\Delta\lambda^i_{n+1} = \frac{f^i_{n+1} + \mathbf{V}^i_{n+1}(\mathbf{A}^i_{n+1})^{-1}\tilde{\mathbf{R}}^i_{n+1}}{\mathbf{V}^i_{n+1}(\mathbf{A}^i_{n+1})^{-1}\mathbf{U}^i_{n+1}} \tag{4.31}$$

that can be used to compute $\delta\tilde{\mathbf{x}}^i_{n+1}$ by Equation (4.30).

Tangent Consistent Matrix

If the trial state is inside or on the yield locus the consistent tangent coincides with the elastic tangent stiffness:

$$\frac{\partial\Delta\hat{\boldsymbol{\sigma}}}{\partial\Delta\boldsymbol{\varepsilon}} = \mathbf{D}^e_{n+1} = \frac{\partial\sigma(\hat{\boldsymbol{\sigma}}_n, \Delta\boldsymbol{\varepsilon})}{\partial\Delta\boldsymbol{\varepsilon}} \tag{4.32}$$

For an elastic process the term describing the explicit dependency of the constitutive law on the degree of saturation is null.

Differentiating the first two component of Equation (4.22):

$$d\Delta\boldsymbol{\varepsilon}^e_{n+1} = d\Delta\boldsymbol{\varepsilon}^{tot} - d\Delta\lambda\mathbf{Q}_{n+1} - \lambda d\mathbf{Q}_{n+1} \tag{4.33a}$$

$$dq_{n+1} = d\Delta\lambda\mathbf{h}_{n+1} + \lambda d\mathbf{h}_{n+1} \tag{4.33b}$$

where

$$d\mathbf{Q}_{n+1} = \frac{\partial\mathbf{Q}_{n+1}}{\partial\hat{\boldsymbol{\sigma}}_{n+1}}\frac{\partial\hat{\boldsymbol{\sigma}}_{n+1}}{\partial\Delta\boldsymbol{\varepsilon}^e_{n+1}}d\Delta\boldsymbol{\varepsilon}^e_{n+1} + \frac{\partial\mathbf{Q}_{n+1}}{\partial\mathbf{q}_{n+1}}d\mathbf{q}_{n+1} \tag{4.34a}$$

$$d\mathbf{h}_{n+1} = \frac{\partial\mathbf{h}_{n+1}}{\partial\hat{\boldsymbol{\sigma}}_{n+1}}\frac{\partial\hat{\boldsymbol{\sigma}}_{n+1}}{\partial\Delta\boldsymbol{\varepsilon}^{el}_{n+1}}d\Delta\boldsymbol{\varepsilon}^{el}_{n+1} + \frac{\partial\mathbf{h}_{n+1}}{\partial\mathbf{q}_{n+1}}d\mathbf{q}_{n+1} \tag{4.34b}$$

Equation (4.33) can be written in compacted form:

$$\mathbf{A}d\tilde{\mathbf{x}} = \mathbf{T}d\Delta\boldsymbol{\varepsilon}^{tot} - \Delta\lambda\mathbf{U} \tag{4.35}$$

where $\mathbf{T}$ is a projection matrix given by

$$\mathbf{T} = [\,\mathbf{I} \quad \mathbf{0}\,] \tag{4.36}$$

The increment in the plastic multiplier associated with a change of plastic strains can be determined by differentiating the consistency condition $f = 0$ (the last component of Equation (4.22)):

$$df = \frac{\partial f}{\partial \hat{\boldsymbol{\sigma}}} d\hat{\boldsymbol{\sigma}} + \frac{\partial f}{\partial \mathbf{q}} d\mathbf{q} = \frac{\partial f}{\partial \hat{\boldsymbol{\sigma}}} \mathbf{D}^e d\Delta\boldsymbol{\varepsilon}^e_{n+1} + \frac{\partial f}{\partial \mathbf{q}} d\mathbf{q} = \mathbf{P}^T \mathbf{D}^e d\Delta\boldsymbol{\varepsilon}^e_{n+1} + \mathbf{W} d\mathbf{q} = \mathbf{V} d\tilde{\mathbf{x}} = 0 \tag{4.37}$$

Solving Equation (4.35) for $d\tilde{\mathbf{x}}$ and substituting the result in Equation (4.37), the following expression is obtained for $d\Delta\lambda$:

$$d\Delta\lambda = \frac{\mathbf{V}\mathbf{A}^{-1}\mathbf{T}}{\mathbf{V}\mathbf{A}^{-1}\mathbf{U}} d\Delta\boldsymbol{\varepsilon}^{tot} \tag{4.38}$$

and this, in turn, provides the following expression, where $d\tilde{\mathbf{x}}$ is a function of $d\Delta\boldsymbol{\varepsilon}^{tot}$

$$d\tilde{\mathbf{x}} = \left[\mathbf{A}^{-1} - \frac{\mathbf{A}^{-1}\mathbf{U}\mathbf{V}\mathbf{A}^{-1}}{\mathbf{V}\mathbf{A}^{-1}\mathbf{U}}\right] \mathbf{T} d\Delta\boldsymbol{\varepsilon}^{tot} \tag{4.39}$$

from which the differential of the elastic strain increment is obtained by multiplying $\mathbf{T}^T$

$$d\Delta\boldsymbol{\varepsilon}^e = \mathbf{T}^T \left[\mathbf{A}^{-1} - \frac{\mathbf{A}^{-1}\mathbf{U}\mathbf{V}\mathbf{A}^{-1}}{\mathbf{V}\mathbf{A}^{-1}\mathbf{U}}\right] \mathbf{T} d\Delta\boldsymbol{\varepsilon}^{tot} = \boldsymbol{\Xi} d\Delta\boldsymbol{\varepsilon}^{tot} \tag{4.40}$$

Matrix $\boldsymbol{\Xi}$ is the ratio between $d\Delta\boldsymbol{\varepsilon}^{el}$ and $\Delta\boldsymbol{\varepsilon}^{tot}$, so that, finally

$$\frac{\partial \Delta\hat{\boldsymbol{\sigma}}}{\partial \Delta\boldsymbol{\varepsilon}^{tot}} = \mathbf{D}^{el}\boldsymbol{\Xi}\,. \tag{4.41}$$

The tangent matrix due to changes in the degree of saturation is derived in the same way followed for the tangent matrix relative to the strain increment. So, the first two components of Equation (4.22) are differentiated, but this time

$$d\mathbf{q}^{trial}_{n+1} = d\Delta S r \boldsymbol{\eta}_{n+1} \qquad d\Delta\boldsymbol{\varepsilon}^{tot} = 0 \tag{4.42}$$

are set. Therefore,

$$d\Delta\boldsymbol{\varepsilon}^{el}_{n+1} = -d\Delta\lambda\mathbf{Q}_{n+1} - \Delta\lambda d\mathbf{Q}_{n+1} \tag{4.43a}$$

$$dq_{n+1} = d\mathbf{q}^{trial}_{n+1} + d\Delta\lambda\mathbf{h}_{n+1} + \Delta\lambda d\mathbf{h}_{n+1} \tag{4.43b}$$

in compacted form become

$$\mathsf{A}d\tilde{\mathbf{x}} = \mathsf{N}d\Delta Sr - \Delta\lambda\mathsf{U} \tag{4.44}$$

where N is given by

$$\mathsf{N}^T = [\,0 \quad \boldsymbol{\eta}\,] \tag{4.45}$$

Following the same procedure as used before (differentiation of the consistency condition, substitutions) the following expression for the tangent matrix can be obtained

$$\frac{\partial\Delta\hat{\boldsymbol{\sigma}}}{\partial\Delta Sr} = \mathsf{D}^{el}\mathsf{T}^T\left[\mathsf{A}^{-1} - \frac{\mathsf{A}^{-1}\mathsf{U}\mathsf{V}\mathsf{A}^{-1}}{\mathsf{V}\mathsf{A}^{-1}\mathsf{U}}\right]\mathsf{N} \tag{4.46}$$

4.2.3 θ-METHOD

A more general class of integration algorithm is the so-called θ-method. This class is subdivided in trapezoidal and midpoint rule. Like both previous method, explicit and implicit, an initial trial solution is calculated first, by a fully elastic prediction, which is checked against an initial trial yield surface, in which the internal variables have already been updated for the change in the degree of saturation. The elastic prediction is followed by a plastic problem, where plastic strain occur. The various θ-methods differ one from the other by the choice for the direction of plastic strain in the plastic correction stage.

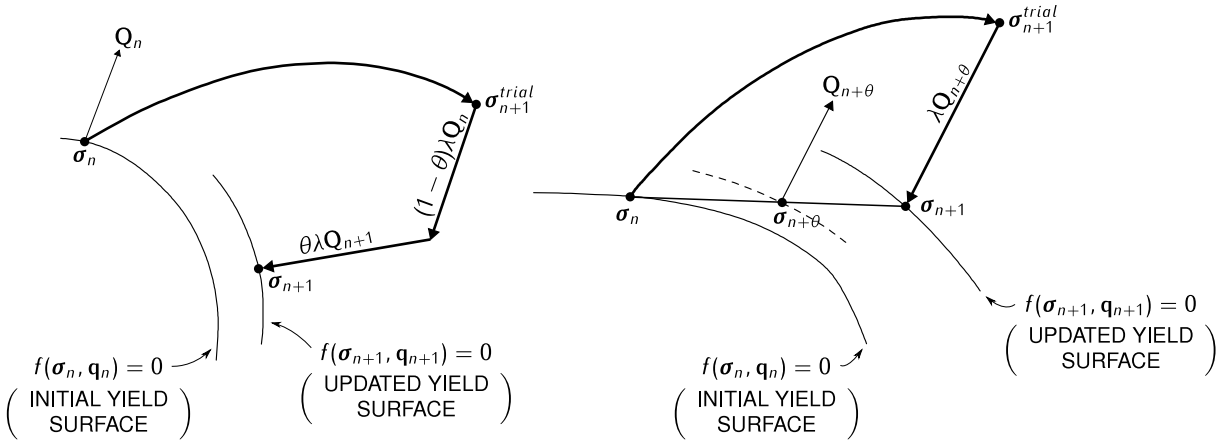

(a) Generalised trapezoidal rule (b) Generalised midpoint rule

Figure 4.4: Geometric interpretation of the θ-method.

5

Solution strategies for the reactive system

In Chapter 2 relevant chemical reactions occurring in electrokinetic treatments were described. Some of them occur due to the physical and chemical complexity of natural soils. This fact can result in non linear and non intuitive responses. A fundamental understanding of the reaction processes is required to quantify the geochemical evolution of natural soil systmes and to assess the benefits of electrokinetic remediation techniques. Finite element analysis requires a lot of computational time to be performed because of the strong coupling between the governing equations presented in Chapter 3. So screening of the most important chemical reactions and preliminary evaluation of their effects is an preliminary step to analyse the solution of a multicomponent reactive transport problem.

In this Chapter a driver for the numerical integration of the chemical species mass balance equation at the representative element volume will be presented. It is a useful tool to get an evaluation of the chemical reactions, and hence of the chemical species, which have to be included into the numerical model.

5.1 Representative element volume balance

In a batch reactor the balance of the chemical species i (dissolved, mineral or gaseous) becomes:

$$\int_\Omega \frac{\partial s_i}{\partial t}\, d\Omega + \int_\Gamma \bar{J}_i\, d\Gamma + \int_\Omega R_i\, d\Omega = 0\,, \tag{5.1}$$

where s_i is the amount of the species (concentration for dissolved specie and pressure for gaseous specie) and the second term represents the imposed flux across the boundary of the batch reactor. Equation (5.1) could be written as

$$\frac{\partial s_i}{\partial t} + f_i + R_i = 0\,, \tag{5.2}$$

where $f_i := \int_\Gamma \bar{J}_i\, d\Gamma / \int_\Omega\, d\Omega$.

A *Representative Element Volume* (REV) of soil could be considered as a batch reactor, where Equation (5.1) holds, if the assumption of constant saturation of the REV has been introduced. Unfortunately in porous media possible unsaturated states, due to the gas generated by chemical reactions, have to be taken into account.

In Section 3.6.2 the mass balance equations of the different chemical species have been described. In this Section they will be summarised with reference to the REV approach:

- mass balance of the dissolved species i (Eq. 3.29) becomes:

$$\frac{\partial (n Sr c_i)}{\partial t} + n Sr R_i + f_i = 0\,; \tag{5.3}$$

- assuming that the law of perfect gas holds, the balance of gaseous species i (Eq. 3.32) is:

$$\frac{\partial (n \rho_i (1 - (1 - h_i) Sr))}{\partial t} + n Sr m_i^{mol} R_i = 0\,; \tag{5.4}$$

- the mass balance of mineral species results from Equation (3.34):

$$\frac{\partial \bar{c}_i}{\partial t} + n Sr R_i = 0\,. \tag{5.5}$$

5.2 Mathematical description of reaction systems

The reactions taking place in the system, the general form of which has been defined in Section 3.8 (Eqs. (3.44) and (3.48) for aqueous and dissolution/precipitation, respectively), can be written in compacted form has:

$$\mathbf{S}\,\mathbf{A} \rightleftharpoons \mathbf{0}\ , \tag{5.6}$$

where the matrix $\mathbf{S}$ contains the stoichiometric coefficients ν_{ij} of the N_r reactions and $\mathbf{A}$ is the vector of the N_s chemical species. Fast reactions (i.e. chemical equilibrium reactions) are characterised by the mass action law (3.46),

$$\mathbf{S}_e \log[\mathbf{A}] = \log \mathbf{K}\ , \tag{5.7}$$

where the matrix $\mathbf{S}_e$ contains the stoichiometric coefficients ν_{ij} of the N_e equilibrium reactions, $[\mathbf{A}]$ is the vector of the activity of the N_s chemical species and the vector $\mathbf{K}$ contains the equilibrium constants of the equilibrium reactions. Stoichiometry of the N_k slow (kinetic) reactions is contained in the kinetic stoichiometric matrix $\mathbf{S}_k$.

The reaction rate of kinetic reactions, $\mathbf{r}_k$, is defined as the amount of reactants evolving to products per unit time (Molins et al., 2004) and it can be written as a function of all concentrations:

$$\mathbf{r}_k = f(\mathbf{c})\ . \tag{5.8}$$

Since $N_s > N_r$, N_r activities, called secondary species ($\mathbf{A}_2$), can be computed from the $N_s - N_r$ remaining activities of the so-called primary species $[\mathbf{A}]_1$. Therefore stoichiometric matrix $\mathbf{S}$ could be subdivided in two parts: $\mathbf{S} = [\mathbf{S}_1 \quad \mathbf{S}_2]$ and the activity of the secondary species can be written as function of the activity of the primary species:

$$\log[\mathbf{A}_2] = \mathbf{S}_1^* \log[\mathbf{A}_1] + \log \mathbf{K}^*\ , \tag{5.9}$$

where $\mathbf{S}_1^* := -(\mathbf{S}_2)^{-1}\mathbf{S}_1$ and $\log \mathbf{K}^* := (\mathbf{S}_2)^{-1} \log \mathbf{K}$. Different sets of primary and secondary species are possible, provided the sets are chosen in such a way that $\mathbf{S}_2$ is a full ranked matrix (Saaltink et al., 1998).

Some species have a unity activity (e.g. minerals and water if concentrations

of dissolved species are sufficiently small). For these N_c species $\log[\mathbf{A}_c] = 0$. Therefore the number of primary species could be reduced following the work of Saaltink et al. (1998). First the primary species are split into N_c dependent primary species, $\mathbf{A}_{1d}$, and $N_s - N_e - N_c$ independent primary species, $\mathbf{A}_{1i}$:

$$\mathbf{A}_1 := \begin{bmatrix} \mathbf{A}_{1i} \\ \mathbf{A}_{1d} \end{bmatrix} . \tag{5.10}$$

The secondary species are divided into N_c constant activity specie, $\mathbf{A}_{2c}$, and the $N_r - N_c$ other secondary species, $\mathbf{A}_{2o}$:

$$\mathbf{A}_2 := \begin{bmatrix} \mathbf{A}_{2o} \\ \mathbf{A}_{2c} \end{bmatrix} . \tag{5.11}$$

The vector $\mathbf{K}^*$ is split like $\mathbf{A}_2$:

$$\mathbf{K}^* := \begin{bmatrix} \mathbf{K}^*_o \\ \mathbf{K}^*_c \end{bmatrix} . \tag{5.12}$$

Therefore the matrix $\mathbf{S}^*_1$ is divided:

$$\mathbf{S}^*_1 := \begin{bmatrix} \mathbf{S}^*_{io} & \mathbf{S}^*_{ic} \\ \mathbf{S}^*_{do} & \mathbf{S}^*_{dc} \end{bmatrix} . \tag{5.13}$$

This subdivision allows writing the primary dependent and the other secondary species as a function of the primary independent species,

$$\log[\mathbf{A}_{1d}] = -(\mathbf{S}^*_{dc})^{-1}\mathbf{S}^*_{ic} \log[\mathbf{A}_{1i}] - (\mathbf{S}^*_{dc})^{-1} \log \mathbf{k}^*_c \tag{5.14a}$$

$$\log[\mathbf{A}_{2o}] = \left(\mathbf{S}^*_{io} - \mathbf{S}^*_{do}(\mathbf{S}^*_{dc})^{-1}\mathbf{S}^*_{ic}\right) \log[\mathbf{A}_{1i}] - \mathbf{S}^*_{do}(\mathbf{S}^*_{dc})^{-1} \log \mathbf{k}^*_c + \log \mathbf{k}^*_0 , \tag{5.14b}$$

and to write the mass of action law (5.7) without the constant activity species:

$$\log[\mathbf{A}'_2] = \mathbf{S}'_e \log[\mathbf{A}_{1i}] + \log \mathbf{K}' \tag{5.15}$$

The terms in Equation (5.15) are defined as:

$$\mathbf{A}_2' := \begin{bmatrix} \mathbf{A}_{1d} \\ \mathbf{A}_{2o} \end{bmatrix} , \tag{5.16a}$$

$$\mathbf{S}_e' := \begin{bmatrix} -(\mathbf{S}_{dc}^*)^{-1}\mathbf{S}_{ic}^* \\ \mathbf{S}_{io}^* - \mathbf{S}_{do}^*(\mathbf{S}_{dc}^*)^{-1}\mathbf{S}_{ic}^* \end{bmatrix} , \tag{5.16b}$$

$$\mathbf{K}' := \begin{bmatrix} -(\mathbf{S}_{dc}^*)^{-1}\log\mathbf{K}_c^* \\ -\mathbf{S}_{do}^*(\mathbf{S}_{dc}^*)^{-1}\log\mathbf{K}_c^* + \log\mathbf{K}_o^* \end{bmatrix} . \tag{5.16c}$$

5.3 Porosity change

Dissolution/precipitation reactions change the mineral content of solid grains, resulting in change of soil porosity.

The volume of the solid grains V_s is the sum of the volume V_i of minerals:

$$V_s = \sum V_i = \sum \frac{m_i}{\rho_i} = \sum \frac{m_i^{mol} n_i}{\rho_i} , \tag{5.17}$$

where ρ_i is the density of mineral i, m_i^{mol} is its molar mass and n_i is its number of moles in the volume V_{TOT}. Substituting the latter relationship into the definition of soil porosity, the expression of porosity as a function of the mineral content is obtained:

$$n = \frac{V_v}{V_{TOT}} = 1 - \frac{V_s}{V_{TOT}} = 1 - \sum \frac{m_i^{mol}}{\rho_i}\bar{c}_i , \tag{5.18}$$

where $\bar{c}_i$ is the solid concentration defined in Paragraph 3.6.2. Therefore, the change in porosity due to change in mineral content is

$$\Delta n = n^{n+1} - n^n = -\sum \frac{m_i^{mol}}{\rho_i}(\bar{c}_i^{n+1} - \bar{c}_i^n) . \tag{5.19}$$

5.4 Solution strategy

Many efforts have been dedicated to solve the multicomponent reactive problem.

The *Direct Substitution Approach* (DSA) consists in substituting chemical equilibrium equations into the balance equations, which leads to a fully coupled system of equations. Different formulations were proposed in the literature. The elimination strategy developed by Saaltink et al. (1998) has been proved to reduce the computational costs of DSA. This strategy reduces the number of equations to be solved removing the constant activity species like minerals. However this strategy does not allow to compute their variations. Another disadvantage of this strategy, usually not pointed out, is that it can not handle vanighing species. To avoid these problems, the elimination strategy usually is used in combination with a kinetic formulation for dissolution/precipitation reactions (e.g. Saaltink et al., 2004; Steefel and MacQuarrie, 1996).

Opposite to the DSA, the fully kinetic approach does not take advantage from the reduction of the equations. Even where equilibrium reactions need to be included, however, it is possible to use a fully kinetic formulation. Several authors simulated systems with both fast and slow reactions using a fully kinetic approach (Mayer et al., 2002). The principal advantage of the fully kinetic approach is that it obviates the need to solve the set of *Differential Algebraic Equations* (DAE) which characterise mixed equilibrium-kinetic systems solved by the DSA.

The reaction rate of a homogeneous reaction may be expressed using the *principle of microscopic reversibility* or *detailed balancing* (Lasaga, 1981, 1984; Morel and Hering, 1993). This principle can be applied both to aqueous inorganic reactions and to dissolution/precipitation reactions, e.g. the carbonates system. It holds in reality only where elementary reaction mechanisms are involved (Lasaga, 1984). For an elementary reaction,

$$\mathrm{A} + \mathrm{B} \underset{k^b}{\overset{k^f}{\rightleftharpoons}} \mathrm{C} \,, \tag{5.20}$$

the reaction rate can be written as the difference between the forward rate,

$$R^f = k^f[\mathrm{A}][\mathrm{B}] \,, \tag{5.21}$$

and the backward rate,

$$R^b = k^b[\mathrm{C}] \,, \tag{5.22}$$

where [A], [B] and [C] are the activities of the species A, B and C respectively, and k^f and k^b are the forward and the reverse rate constant, respectively. For a dilute species the activity may be substituted with concentration, so the reaction rate reads

$$R = k^f c_A c_B - k^b c_C \ . \tag{5.23}$$

Where this approach is used to approximate equilibrium reactions, it is immaterial what the actual absolute values of the forward and reverse rate constants are, as long as they are chosen in the proper ratio $k^f/k^b = K^{eq}$. Thus for the r-th reaction it results in

$$R_r = k_r^f \left(\prod_{j|\nu_{jr}>0} (c_j)^{\nu_{jr}} - \frac{1}{K_r^{eq}} \prod_{j|\nu_{jr}<0} (c_j)^{-\nu_{jr}} \right) \ . \tag{5.24}$$

The forward reaction rate k_r^f has to be sufficiently large such that local equilibrium is attained during the time scale of interest. However, the system will better behave numerically if the rate constants are chosen so that they are sufficiently but not excessively large (Steefel and MacQuarrie, 1996).

For the m-th precipitation/dissolution reaction it results in

$$R_m = \begin{cases} 0 & \text{if } \bar{c}_m = 0, IAP_m < 0 \\ k_m^f \left(1 - \dfrac{IAP_m}{K_m^{sp}}\right) & \text{otherwise} \end{cases} \ . \tag{5.25}$$

where $IAP_m = \prod c_i^{\nu_{mi}}$ is the *Ion Activity Product*. This approach has been widely applied to mineral dissolution and precipitation (Aagaard and Helgeson, 1982; Lasaga, 1984), although the actual mechanism involved in the dissolution will tend to change the formulation.

Since the reactions rates are defined by Equations (5.24) and (5.25), Equations (5.3),(5.4) and (5.5) form a system of differential equations where the unknowns are the concentrations of the dissolved species, c_i, the partial pressures of the gaseous species, p_i, and the concentration of the mineral species, $\bar{c}_i$. This set of differential equations is discretised in time by a Backward Euler method:

$$nSr^{n+1} c_i^{n+1} - nSr^n c_i^n + nSr^{n+1} R_i^{n+1} \Delta t + f_i \Delta t = 0 \ , \tag{5.26a}$$

$$n\rho_i^{n+1}(1-(1-h_i)Sr^{n+1}) - n\rho_i^n(1-(1-h_i)Sr^n) + nSr^{n+1}m_i^{mol}R_i^{n+1}\Delta t = 0\ , \tag{5.26b}$$

$$\bar{c}_i^{n+1} - \bar{c}_i^n + nSr^{n+1}R_i^{n+1}\Delta t = 0\ . \tag{5.26c}$$

Newton's method is the most common choice to solve systems of nonlinear equations of the type (5.26). However, its convergence may fail to occur in any neighbourhood of the solution if its derivative is not continuous (the function is not C^1 in the neighbourhood of the solution). Equation (5.25) posseses non continuum derivatives respect to the concentrations of mineral species, hence Newton's method can not be applied. In order to handle this problem a splitting procedure was introduced (Algorithm 5.1). First the concentrations of the dissolved species and the partial pressure of the gaseous species are computed solving their mass balance together with the reaction rates and the expression of the WRC by means of Newton's method. Afterwards, the mass balance of the mineral species is solved.

Algorithm 5.1: Solution procedure of the equation at the point volume

1. SET $i = 0$ and $\mathbf{s}^{n+1,i} = \mathbf{s}^n$, where $\mathbf{s} := [\,\mathbf{c}\ \mathbf{p}\,]$.
2. REPEAT
3. COMPUTE pressure of the gas phase: $u_g^{n+1,i} = \sum_j^{N_g} p_j^{n+1,i} - p_j^{ref}$
4. COMPUTE degree of saturation: $Sr^{n+1,i} = Sr(u_g^{n+1,i})$
5. COMPUTE partial density of the gaseous species: $\rho_g = \rho_g^0 \frac{p_g^{n+1,i}}{p_{atm}}$
6. COMPUTE reaction rates

$$R_r^{n+1,i} = k_r^f \left(\prod_{j|\nu_{jr}>0} (s_j^{n+1,i})^{\nu_{jr}} - \frac{1}{K_r^{eq}} \prod_{j|\nu_{jr}<0} (s_j^{n+1,i})^{-\nu_{jr}} \right)$$

7. COMPUTE mass balance of dissolved and gaseous species

$$Res_d = nSr^{n+1,i}c_d^{n+1,i} - nSr^n c_d^n + nSr^{n+1,i}R_d^{n+1,i}\Delta t + f_d\Delta t$$

$$Res_g = n\rho_g^{n+1,i}(1-(1-h_g)Sr^{n+1,i}) - n\rho_g^n(1-(1-h_g)Sr^n) + nSr^{n+1,i}m_g^{mol}R_g^{n+1,i}\Delta t$$

8. update of concentrations and pressures:

$$\mathbf{s}^{n+1,i+1} = \mathbf{s}^{n+1,i} - \left[\frac{\partial \mathbf{Res}}{\partial \mathbf{s}} \Big|^{n+1,i} \right]^{-1} \mathbf{Res}$$

9. UNTIL $\mathbf{Res} \neq \mathbf{0}$
10. COMPUTE the concentration of mineral species: $\bar{c}_m^{n+1} = \bar{c}_m^n + nSr^{n+1} R_m^{n+1} \Delta t$
11. update porosity

$$n^{n+1} = n^n - \sum_i^{N_m} \frac{m_i^{mol}}{\rho_i} (\bar{c}_i^{n+1} - \bar{c}_i^n)$$

However the splitting procedure may lead to negative concentration of the mineral species. To avoid this problem an adaptive time stepping procedure, based on the chord method was introduced. This procedure is summarised in Algorithm 5.2 .

Algorithm 5.2: Automatic substepping

1. SET $\beta = 0$
2. REPEAT
3. SET $j = 0 : \alpha^0 = 1 - \beta, \mathbf{s}^0 = \mathbf{s}^n$
4. REPEAT
5. solve the step with $\alpha^j \Delta t \rightarrow c_i^{n+1,j}, p_i^{n+1,j}$
6. COMPUTE the concentration of mineral species

$$\bar{c}_m^{n+1,j} = \bar{c}_m^n + nSr^{n+1,j} R_m^{n+1,j} \alpha^j \Delta t$$

7. reduce the step size

$$\alpha^{j+1} = \frac{\bar{c}_m^{n+1,j} - \bar{c}_m^n}{nSr^{n+1,j} R_m^{n+1,j} \alpha^j \Delta t}$$

8. UNTIL $\bar{c}_m^{n+1,j} < 0$
9. $\beta = \beta + \alpha$
10. update aqueous and gaseous species $c_i^{n+1} = c_i^{n+1,j}$, $p_i^{n+1} = p_i^{n+1,j}$
11. update mineral species $\bar{c}_m^{n+1} = \bar{c}_m^{n+1,j}$

12. update porosity

$$n^{n+1} = n^n - \sum_i^{N_m} \frac{m_i^{mol}}{\rho_i} (\bar{c}_i^{n+1} - \bar{c}_i^n)$$

13. `UNTIL` $\beta = 1$

6

Experimental tests modelling

Within the PRIN research project, different laboratory test programs were developed, the results of which will be reviewed in this Chapter. The experimental data are used to calibrate the numerical model.

At first the results of oedometric tests performed at the Università di Palermo will be shown. The goal of this tests was the characterisation of the mechanical behaviour in unsaturated conditions. These tests will be reproduced at the *Volume Point Element* by means of the numerical procedure outlined in Chapter 4.

Afterwards, the results of electrokinetic filtration tests performed at the Soil Mechanics Laboratory of the Politecnico di Torino will be shown. The results of electrokinetic filtration tests will be compared with the numerical results of the finite element model in Chapter 7. In this Chapter the results of the tests will be interpreted by means of the simple numerical procedure outlined in Chapter 5 in order to define the most important involved chemical reactions. The sample dismounted from one filtration test was cut in slices and each slice was subjected to an oedometric tests. Two additional tests were performed on untreated soil as reference for the behaviour of the natural soil. These latter tests were also performed to compare the effects of the different samples preparation procedures adopted at Università di Palermo and at the Politecnico di Torino. The results will be shown in Section 6.4, where also the comparison with the prediction of the constitutive model will be discussed.

All these tests were performed on the same soil. The soil treated is a natural clay from Scanzano (PA, Italy). Due to its low permeability and its mechanical properties it is suitable as core material in earth dams and as barrier in waste isolation fills. For this reason in the early '60 it was adopted in the construction of the cores of the Scanzano and Rossella Dams near to Palermo (Airò Farulla and Jommi, 2005). It is a medium active silty clay, with a moderate calcite content, comparable to that of many common natural soils. Its relevant properties are summarised in Table 6.1.

Table 6.1: Physical properties of Scanzano clay.

Index Property	Value
% clay	85
% silt	15
Limit liquid, w_L(%)	58
Plasticity Index, I_p	0.30
Specific gravity, G_s	2.78
Activity, A	0.88
Calcite mass fraction, $CaCO_3$(%)	15.1

6.1 Water retention curve

The water retention curve (WRC) of Scanzano clay was investigated by the research group at the Soil Mechanics Laboratory of Università di Palermo (Airò Farulla et al., 2011, 2007) by means of numerous tests.

Two experimental techniques were combined in order to explore the retention properties in a wide range of suction. Vapour equilibrium technique was used to impose total suction in the range $2 \div 110$ MPa, whereas axis translation technique was applied to control matric suction in the range $10 \div 800$ kPa. Suction values lower than 2 MPa were controlled by means of the axis translation technique (air overpressure method) in two suction controlled oedometers.

The dependence of the WRC on the void ratio has been pointed out in Section 3.7, and it has been confirmed by the experimental data presented in Figure 6.1a. Nevertheless, as a first approximation, in the following it will be assumed

that the water storage capacity of the soil investigated can be described by a unique hysteretic retention curve in the suction-degree of saturation plane. As the dependence of the WRC on volumetric strains is disregarded, the retention properties of the soil samples may be described by means of data coming from different data sets (Figure 6.1).

Water retention data may be fitted to a van Genuchten (1980) expression for the degree of saturation, Sr, as a function of suction, s:

$$Sr = \left(\frac{1}{1 + (\alpha s)^n} \right)^m \tag{6.1}$$

Parameters n, m and α describe the shape of the retention functions. Hysteresis is introduced by defining two different sets of parameters for the main drying branch and the main wetting branch of the retention domain, respectively (Fig. 6.1b).

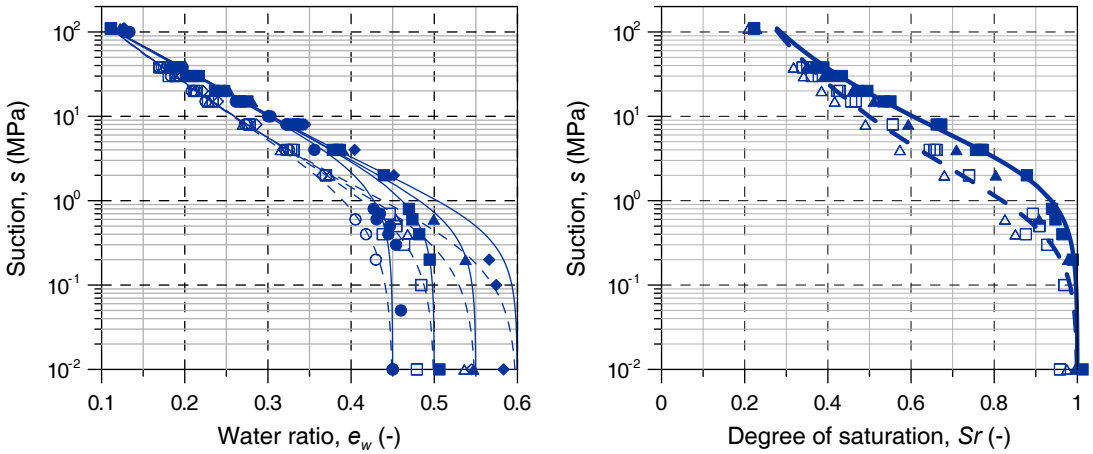

(a) void (b) saturation

Figure 6.1: Water retention curve.

Inside the domain delimited by the main wetting and the main drying branches, the hydraulic behaviour is assumed to be reversible, with a simple linear relationship between suction and degree of saturation. The slope of the scanning curves, $\partial Sr/\partial s = \kappa_s$, is given a constant value. Fitted parameters for the description of the water retention domain of Scanzano clay are listed in Table 6.2.

Table 6.2: Parameters of the retention curves according to Equation (6.1).

Parameter	Drying Branch	Wetting Branch	Scanning Curves
n	1.339	1.254	-
m	0.253	0.203	-
$1/\alpha$ (MPa)	2.519	0.664	-
κ_s (1/MPa)	-	-	0.02

6.2 Mechanical tests

The research group at the Soil Mechanics Laboratory of the Università di Palermo performed different tests in order to study the behaviour of Scanzano Clay under mechanical loads.

The samples were prepared following two different procedures. For both procedures the samples were prepared starting from the air-dried clay ground with a rubber pestle.

The partially unstructured clay samples were prepared starting from the material passing at N° 4 ASTM sieve (4.75 mm). Distilled water was added to a target water content of 0.15-0.17. The soil was then compacted dynamically with a modified Proctor procedure to the target density $\gamma_d = 16.7 \div 17.6$ kN/m^3. Samples had a void ratio of about $e_0 = 0.55$, resulting in a degree of saturation $Sr_0 \simeq 0.75$.

The reconstituted clay samples were prepared starting from the material passing at 2 mm sieve. A slurry at $1.1 \div 1.4$ times the liquid limit of the clay was prepared. The preparation was concluded by a one dimensionally consolidation of the slurry up to a vertical stress of 200 kPa. After preparation the samples were saturated and they had a void ratio of about $e_0 = 0.95$ and a water content $w_0 = 0.347$.

6.2.1 Unsaturated oedometric tests

The controlled-suction oedometer used for unsaturated soil testingwas designed at the the Geotechnical Laboratory of the UPC. It is equipped with a ceramic disk with 1.5 MPa nominal air entry value. Suction is applied by means of the axis translation technique, keeping air pressure constant, $u_a = 1000$ kPa, and varying the applied water pressure, u_w.

Starting from the as-compacted state, suction and a vertical load of 50 kPa were applied. Samples were then subjected to one-dimensional compression increasing the vertical load in steps up to a final value of 1600 kPa. The load steps follow a geometric progression (50-100-200-400-800-1600). Samples were then unloaded following the same loading steps. Results of the tests are depicted in Figure 6.2. The soil stiffness, both in the virgin compression branch and in the unloading steps,

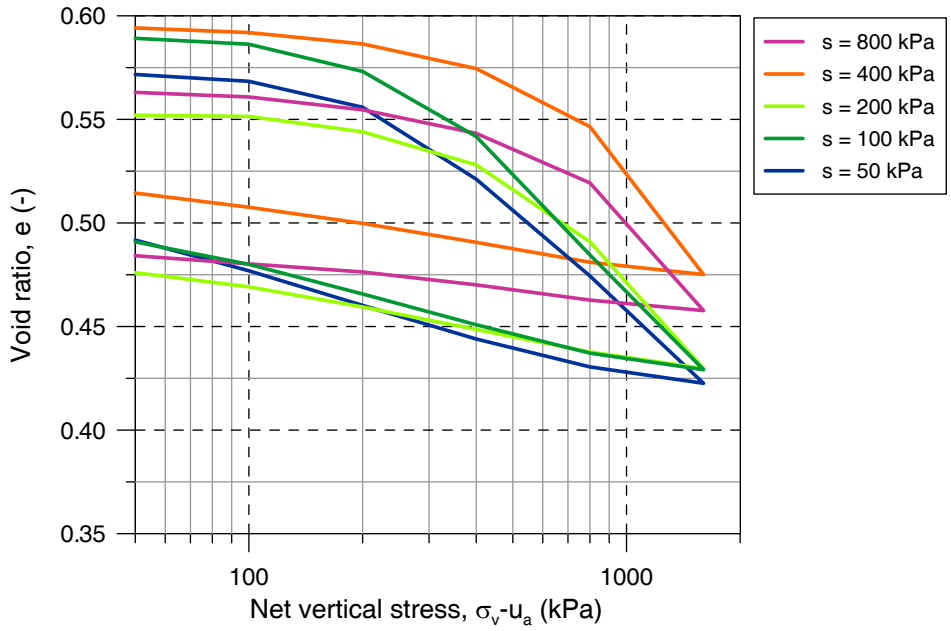

Figure 6.2: Oedometric tests at constant suction.

increases with increasing suction. Also the preconsolidation stress increases with increasing suction.

6.2.2 Triaxial tests

The controlled-suction triaxial apparatus is based on a classic Bishop & Wesley-type triaxial cell (Bishop and Wesley, 1975). The axial and lateral stress are applied using the axial loading ram and the confining water pressure as in conventional triaxial cells. Suction is applied by means of the axis translation technique. Air pressure is imposed at the top of the specimen, where there is a porous stone with

a low air entry value, while water pressure is imposed at the bottom, where a porous stone with high air entry value is placed. Volume change of the specimen is measured using the double wall cell system.

Consolidated undrained triaxial tests

Rosone (2011) performed consolidated undrained triaxial tests on reconstituted clay samples (Figs. 6.3-6.4). Four of the 14 tests were performed on overconsolidated

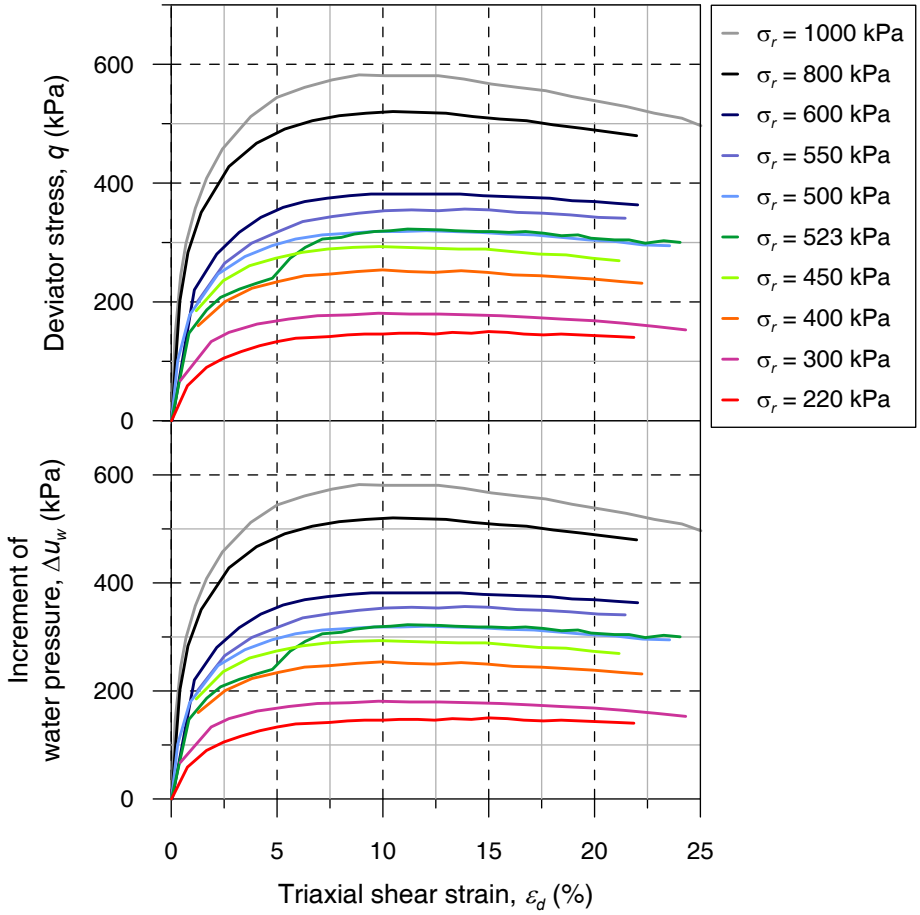

Figure 6.3: Undrained triaxial tests performed on NC samples.

samples (Fig. 6.4). Three of these overconsolidated samples were prepared by one dimensionally consolidation from slurry up to a vertical stress of 800 kPa instead of 200 kPa. As expected, the normally consolidated samples have a definite harden-

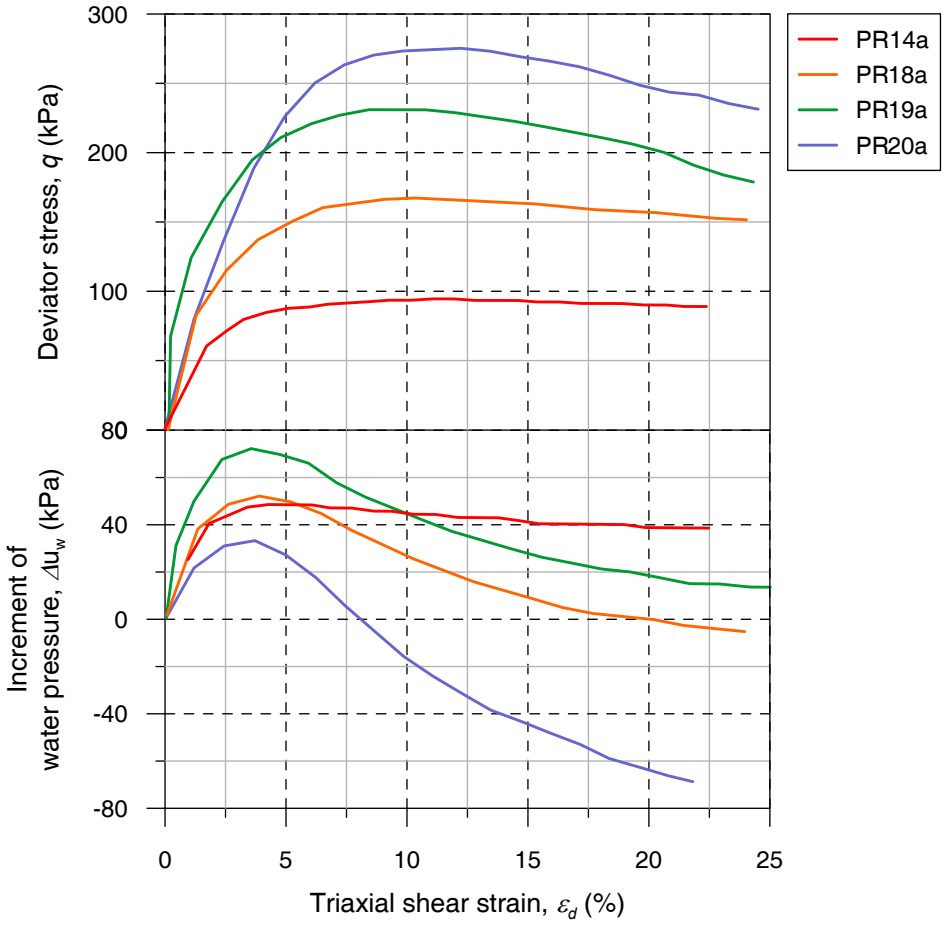

Figure 6.4: Undrained triaxial tests performed on OC samples.

ing behaviour throughout. On the contrary heavy overconsolidated samples show softening behaviour after peak.

The envelope of the critical states defines the *critical state line* (CSL) of Scanzano clay (Fig. 6.5), which is described by the classical equations

$$v = \Gamma - \lambda \log p' \tag{6.2a}$$

$$q = Mp' \,, \tag{6.2b}$$

where $\Gamma = 2.481$, $\lambda = 1.1405$ and $M = 0.902$.

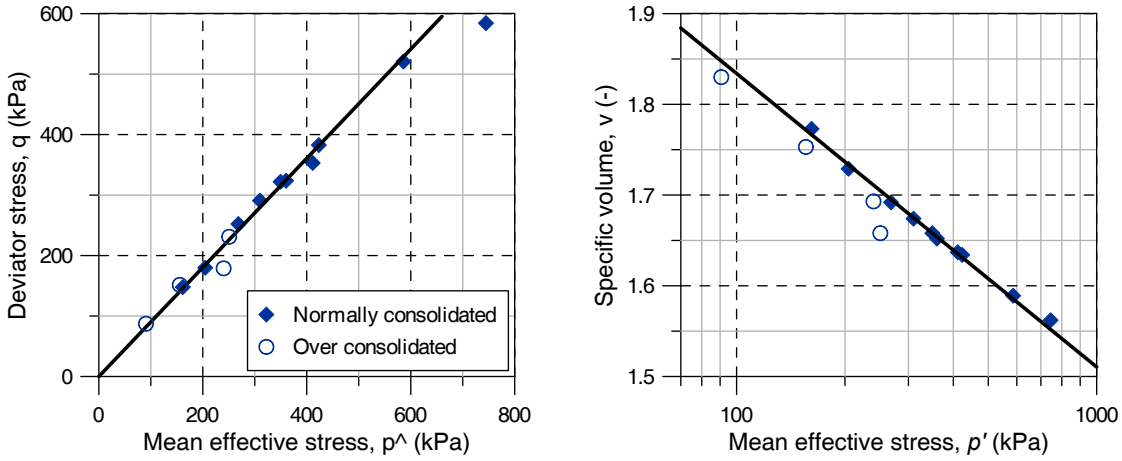

Figure 6.5: Critical state envelope.

Constant suction triaxial tests

Triaxial tests at constant suction were performed on the partially unstructured clay. In Figure 6.6 the loading paths are depicted. After preparation, the samples were mounted in the triaxial cell and they were all subjected to the same initial stress path. Isotropic loading up to a net mean stress of 50 kPa were performed and a matric suction of 50 kPa was imposed. Afterwards the suction of some samples was increased to 100 and 200 kPa. An isotropic loading stage up to $p'' = 100-200$ kPa was performed before shearing at constant suction (Fig. 6.6).

It is interesting to note that the critical states of this tests lie on the same line defined for saturated conditions (Fig. 6.8), if the results are elaborated in terms of $\hat{p}$.

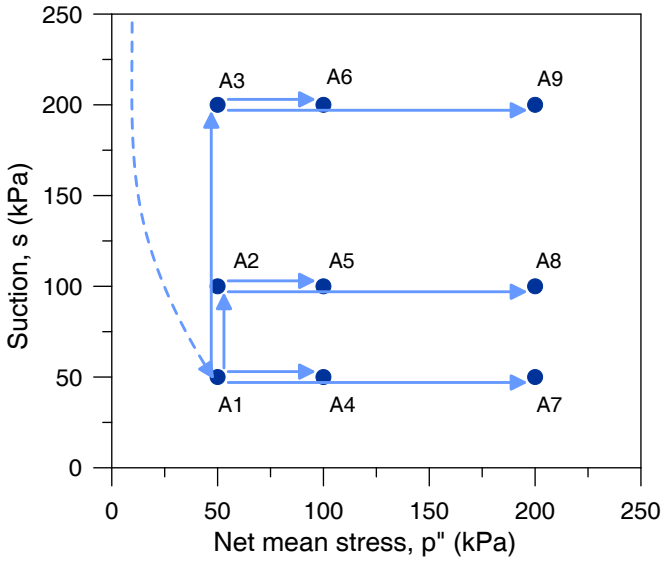

Figure 6.6: Triaxial tests at constant suction: loading paths.

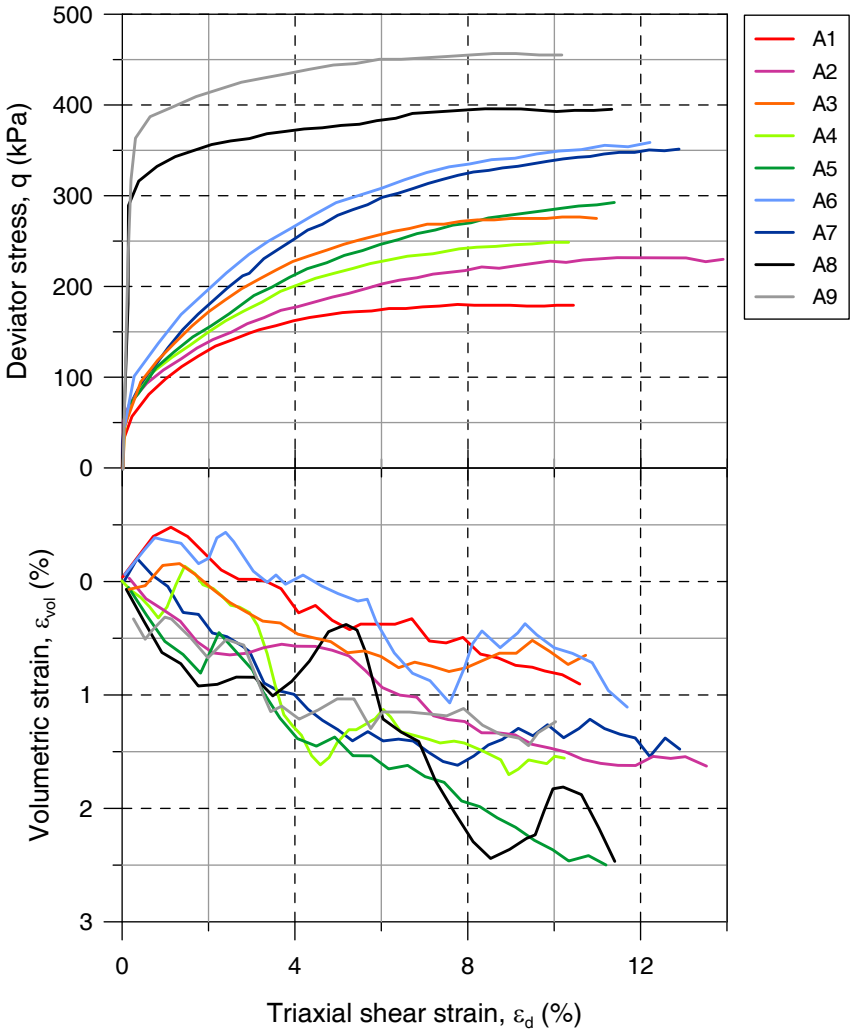

Figure 6.7: Triaxial tests at constant suction: experimental results.

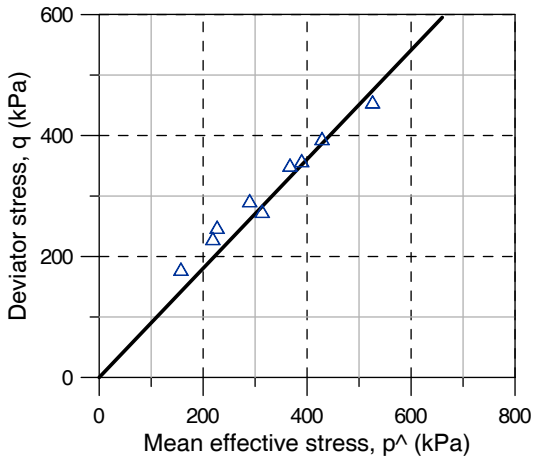

Figure 6.8: Triaxial tests at constant suction: envelope of critical states.

6.3 Electrokinetic filtration tests

Gabrieli (2010) performed electrokinetic filtration tests at the Soil Mechanics Laboratory of the Politecnico di Torino.

The experimental filtration cell used in the investigation was designed by Musso (2000) and it is sketched in Figure 6.9. Two reservoirs separate the soil sample from the electrodes, allowing the gas produced by electrodes reactions to leave the cell without entering the soil.

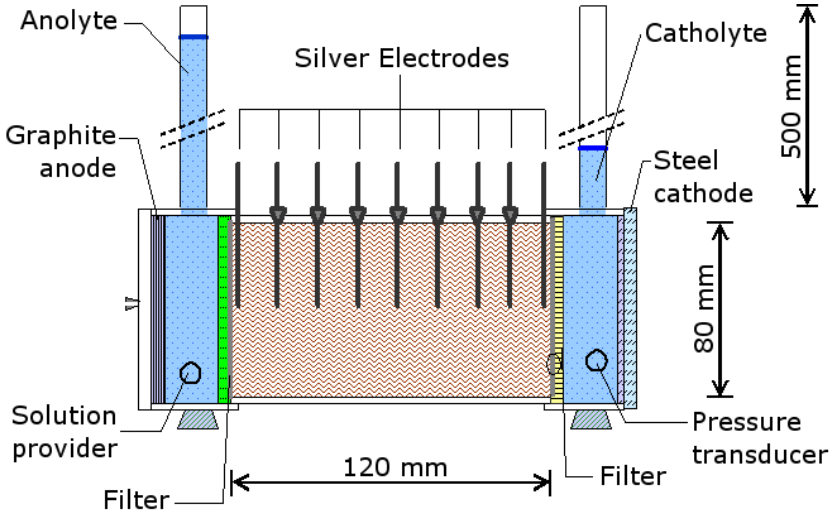

Figure 6.9: Scheme of the electrokinetic filtration test.

Samples were prepared with a 10^{-2} M KCl solution in distilled water, starting from ground air dried material. In order to achieve complete saturation a slurry at one and a half times the liquid limit of the clay was prepared. The preparation was concluded by one dimensionally consolidation of the slurry in different load steps up to a vertical stress of 100 kPa. After preparation the samples were saturated and they had a void ratio of about $e_0 = 0.95$ and a water content $w_0 = 0.347$.

6.3.1 Experimental evidence

Only four of the tests performed by Gabrieli (2010) will be described here. Their duration and measurements performed during or after the elctrokinetic filtration

tests are summarised in Table 6.3. A constant current of 40 mA, corresponding to a current density of 0.8 mA/cm^2, was imposed for about 300 hour. Hydraulic conditions were not fully controlled. At the beginning of the tests a pressure head difference of about 40 cm was set, which tends to decrease during the tests due to the electrosmotic flow. When the pressure head in the two reservoirs reached the same height the anodic reservoir was refilled, while the cathodic one was emptied.

Table 6.3: Summary of the performed tests.

	CBC	Casp_er_01	Casp_er_02	Casp_er_03
Duration (h)	334	331	337	335
Electric potential	⋆	⋆	⋆	⋆
Outflow volume	⋆	⋆	⋆	⋆
pH	⋆	⋆	⋆	⋆
Degree of saturation	⋆	⋆		
Carbonate content	⋆	⋆		
Void ratio	⋆	⋆		

During the tests, voltage was measured locally by means of nine silver chloride electrodes placed into the sample (Figs. 6.10 and 6.11), and the water volume outflow was continuously recorded (figs. 6.12). A 10^{-2} M KCl solution was continuously fed at the anode since the presence of the chlorine ions ensure the stability of the silver probes. In the early stages of the tests electric potential was linear along the samples, meaning that the electrical conductivity was constant. Afterwards the electric potential showed a high drop near the anode. It means that the apparent electrical conductivity decreases near the anode, while in the rest of the samples it remains constant from about 96 h until the end of the tests (fig. 6.10). Initially the outflow volume had a linear increasing rate, then the flow tended to decrease. The refilling-emptying procedure didn't affect the flow rate which keeps linear after the latter procedure. This can be explained by the hydraulic conductivity of the tested soil, which is so low that the contribution of the hydraulic gradient to the net flow is negligible.

At the end of the tests, the samples were dismounted from the cell and cut into slices, and the final values of the pH were determined (fig. 6.13). The pH

was measured by means of paper strips at the boundaries of every slice. Soil pH was very low near the anode, and rapidly increased already at limited distance, reaching high values for the entire cathodic half of the samples. In one of the tests (Casp_er_01), after the paper strips measure, the interstitial fluid was extracted from each slice and its pH was measured with a pH-meter (fig. 6.14). The measures on test Casp_er_01 show the presence of two opposite fronts: an acid front from the anode at about 1 cm distance, and a base front from the cathode penetrated up to the middle of the sample. Since the initial pH was homogeneous along the sample, it means that the base front moves faster than the acid one.

As reported in Table 6.3, for two tests, CBC and Casp_er_01, also the degree of saturation, the carbonate content and the void ratio were determined on each slice (figs. 6.15-6.17). The samples showed a peak of desaturation around 3 cm from the anode. Calcite fraction is very low near the anode, while it is a bit higher than the initial content in the cathodic half of the samples. Distribution of calcite along the samples follows quite well the distribution of the pH.

Systematic development of fractures close to the anode was observed in every test (fig. 6.18). Detaching of the anodic half from the lateral walls of the cell was also observed during the tests.

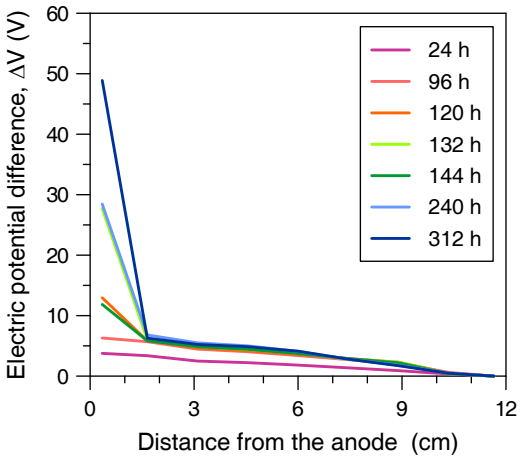

(a) CBC

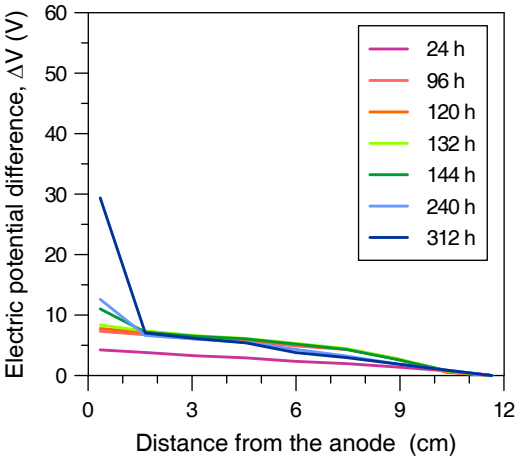

(b) Casp_er_01

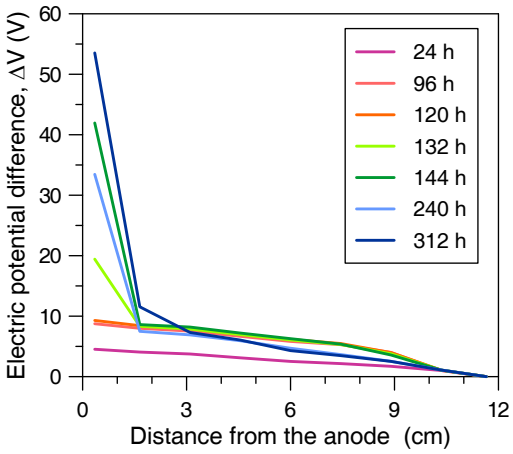

(c) Casp_er_02

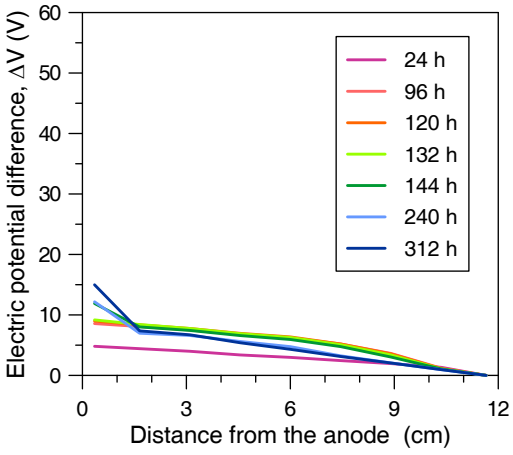

(d) Casp_er_03

Figure 6.10: Isochrones of the electric potential difference.

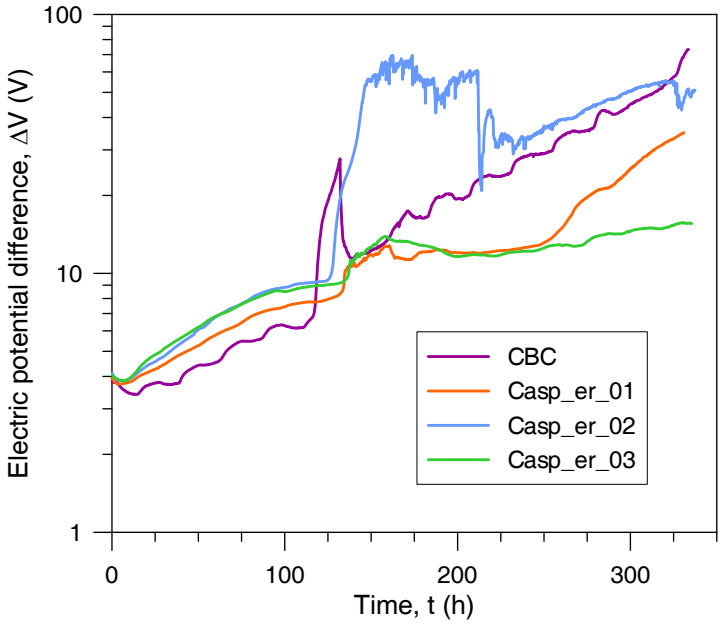

Figure 6.11: Electric potential difference.

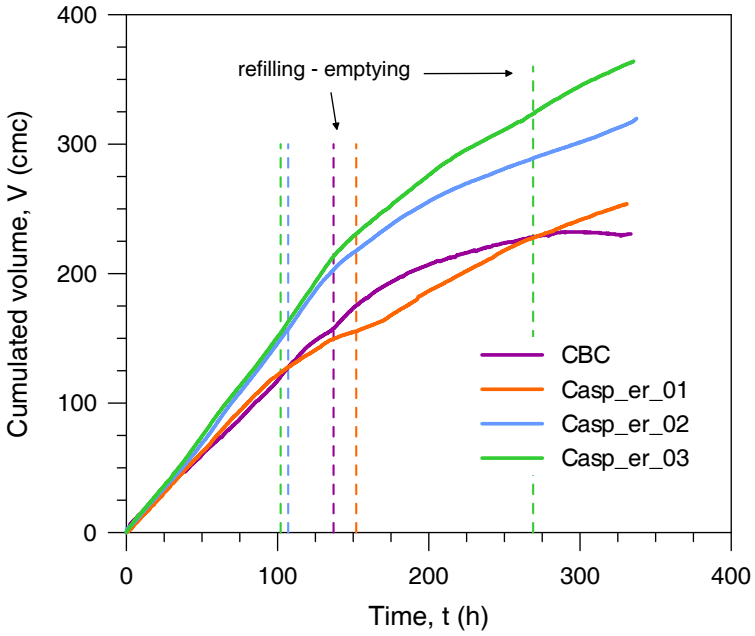

Figure 6.12: Outflow water volume.

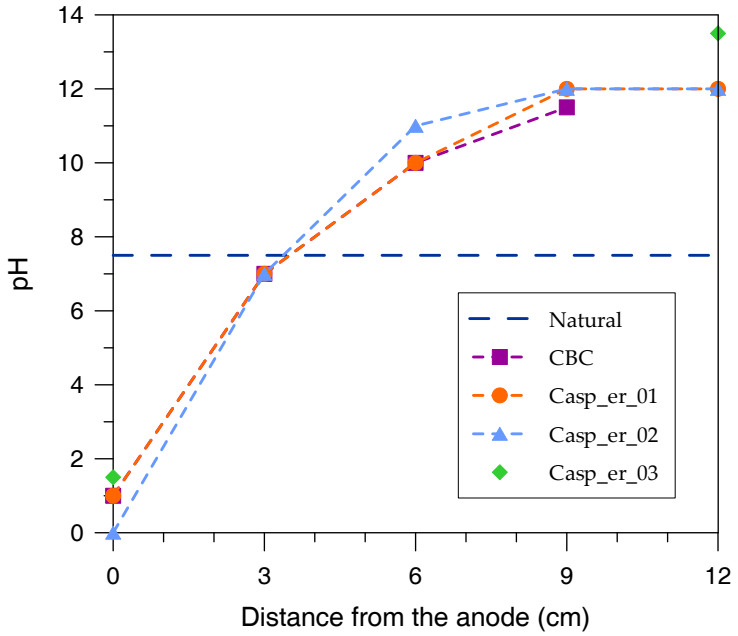

Figure 6.13: pH along the samples at test dismounting.

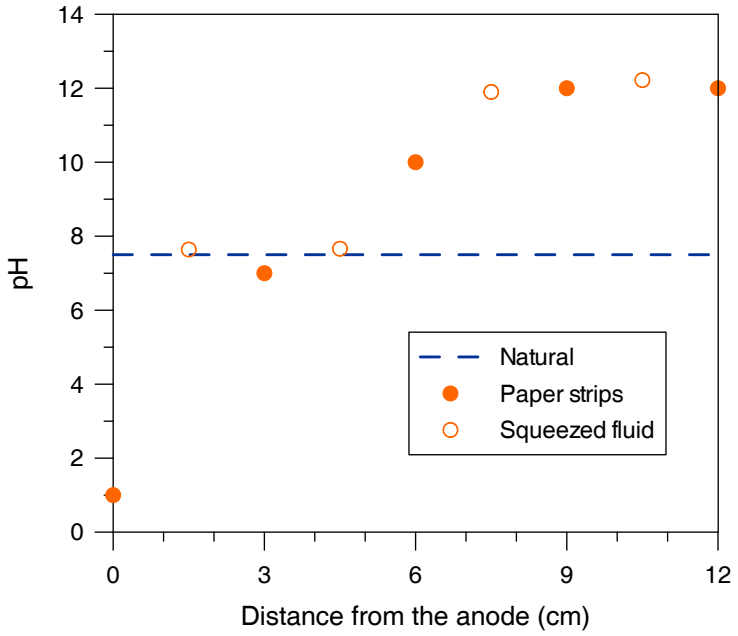

Figure 6.14: Casp_er_01: pH distribution along the sample.

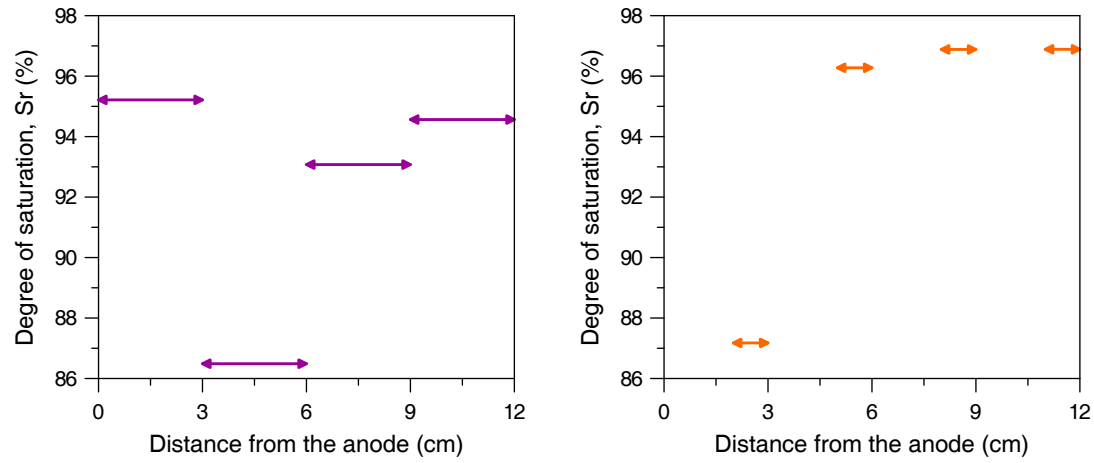

(a) CBC (b) Casp_er_01

Figure 6.15: Degree of saturation along the samples at test dismounting.

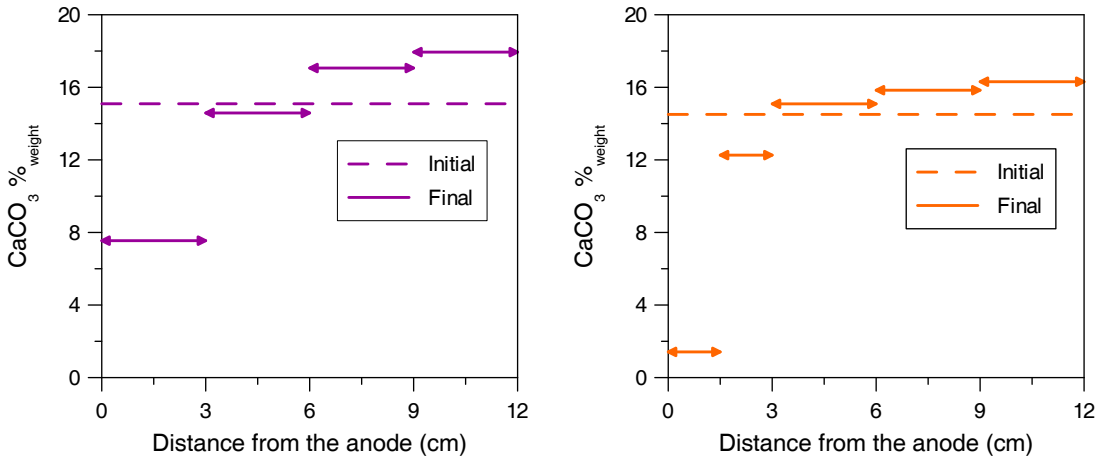

(a) CBC (b) Casp_er_01

Figure 6.16: Final calcite mass fraction along the samples.

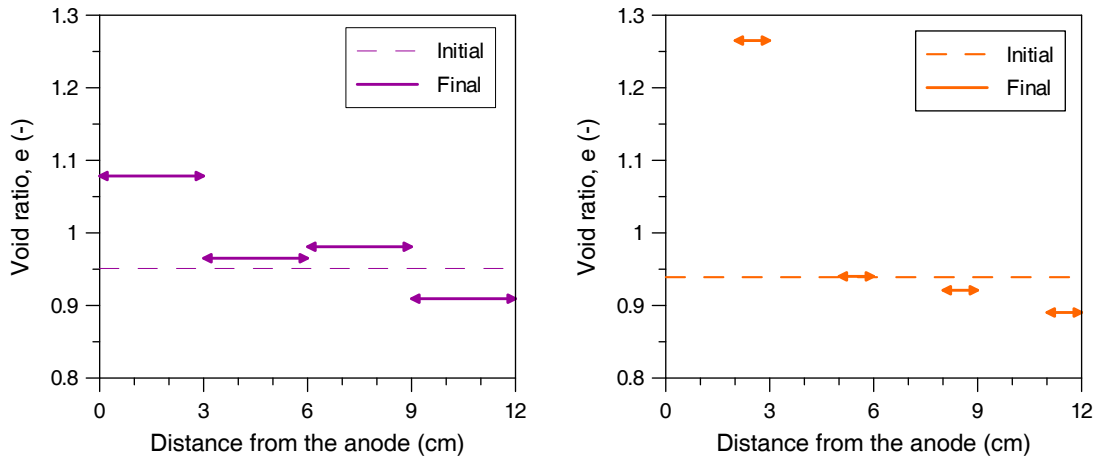

(a) CBC

(b) Casp_er_01

Figure 6.17: Final void ratio along the samples.

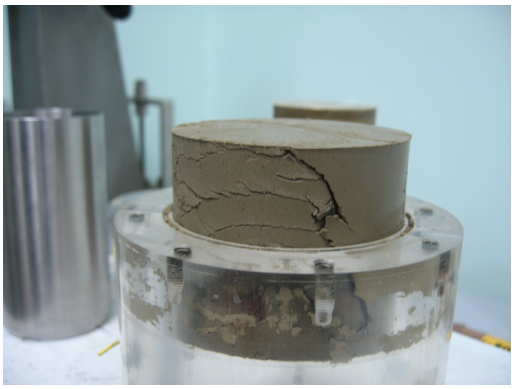

(a) CBC

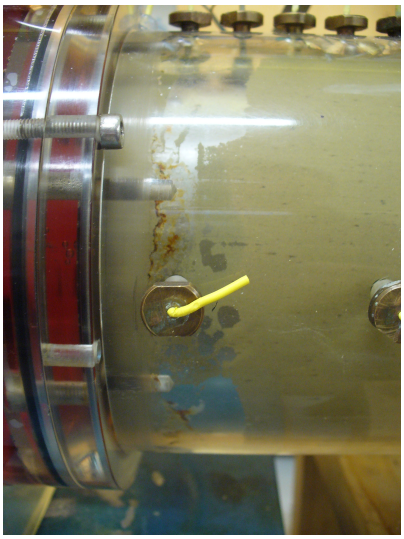

(b) Casp_er_01

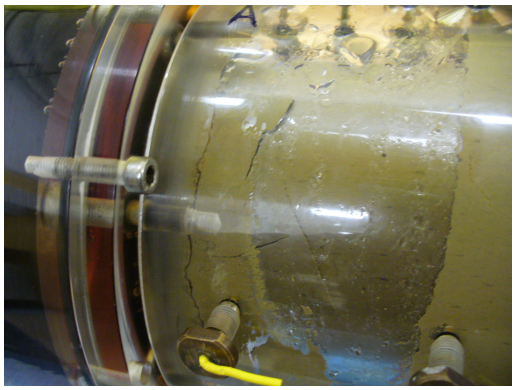

(c) Casp_er_02

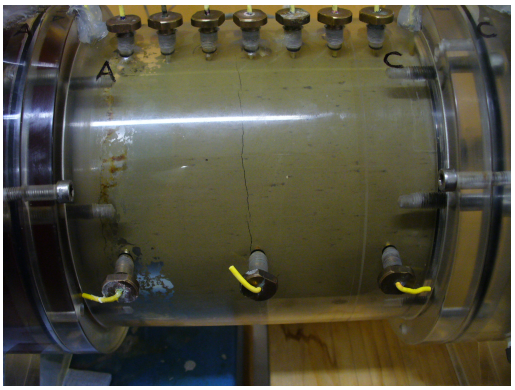

(d) Casp_er_03

Figure 6.18: Fractures observed.

6.3.2 Theoretical interpretation of the experimental results

As discussed in Paragraph 2.1.4, at low pH level the carbonate ion vanishes and calcite has to dissolve to restore its solubility equilibrium. This fact is confirmed by experimental results (Fig. 6.16). The low pH level at the anode increases carbonic acid concentration, so, to restore the equilibrium of CO_2 (2.8), gaseous $CO_{2(g)}$ develops. The consequent high gas pressures, due to the generated $CO_{2(g)}$, tend to desaturate the samples (Fig. 6.15). In the filtration cell the sample cannot expand due to the cell walls constraint, but it's allowed to contract. Desaturation together with high gas pressure may explain the systematic cracks observed close to the anode.

At the opposite side, at high pH levels, carbonates are present only as carbonate ions, so calcite precipitates when calcium ions are in excess to restore its equilibrium. The calcium ions that take part to the precipitation process come from the dissolution process occurring at the anode, which releases carbonate and calcium ions. Calcium ions are transported towards the cathode by convective flux.

6.3.3 A simple quantitative interpretation

Preliminary numerical considerations can be performed before the finite element model is set using a simple chemical model at the REV level. The chemical model is integrated by the numerical procedure developed in Chapter 5. Comparison of the results of this simple model (in the following it will be referred to as *REV model*) with the experimental results allows weighting the respective role of the different chemical species.

Initial concentration

Starting from the measured pH and its definition, $\mathrm{pH} = -\log c_{H^+}$, concentration of hydrogen ions, $c^0_{H^+}$, can be computed. The concentration of hydroxyl is deduced from the water auto ionisation reaction (2.5). The chemical system of carbonates

(Eqs. 2.8-2.10) and the precipitation/dissolution of calcite (Eq. 2.11),

$$
\begin{aligned}
K_h &= \frac{[H_2CO_3^*]}{p_{CO_2}} \\
K_1 &= \frac{[H^+][HCO_3^-]}{[H_2CO_3^*]} \\
K_2 &= \frac{[H^+][CO_3^{2-}]}{[HCO_3^-]} \\
K_s &= [Ca^{2+}][CO_3^{2-}] \,,
\end{aligned}
$$

form a system of four equation with five unknowns ($c^0_{H_2CO_3^*}$, $p^0_{CO_2}$, $c^0_{HCO_3^-}$, $c^0_{CO_3^{2-}}$, $c^0_{Ca^{2+}}$). Electroneutrality of the water phase introduces the constraint to close the system:

$$
2c^0_{Ca^{2+}} + c^0_{H^+} = c^0_{HCO_3^-} + 2c^0_{CO_3^{2-}} + c^0_{OH^-} \,. \tag{6.3}
$$

The initial concentrations of the chemical species, computed from the measured value of pH (7.91), are summarised in Table 6.4.

Table 6.4: Initial concentration of chemical species.

Specie	Concentration
H^{+0}	$1.23 \cdot 10^{-8}$ mol/l
OH^{-0}	$8.128 \cdot 10^{-7}$ mol/l
CO_3^{2-0}	$6.363 \cdot 10^{-6}$ mol/l
HCO_3^{-0}	$1.56 \cdot 10^{-3}$ mol/l
Ca^{2+0}	$7.877 \cdot 10^{-4}$ mol/l
$H_2CO_3^{*0}$	$3.83 \cdot 10^{-5}$ mol/l
$p^0_{CO_2}$	122.6 Pa

The initial solid concentration of calcite was computed from the measured calcite mass fraction by means of Equation (3.35), where the molar mass and the density of calcite are $m_{CaCO_3} = 100$ g/mol and $\rho_{CaCO_3} = 2710$ kg/m^3, respectively. The initial solid concentration $\bar{c}_{CaCO_3} = 2.233$ mol/l was obtained from the measured initial void ratio $e^0 = 0.951$ and calcite mass fraction $f^0_{CaCO_3} = 15.1\%$.

Results

For all reactions a forward reaction rate $k_r^f = 1$ was adopted.

A REV representing the mean values in the first 3 cm thick slice is analysed, as it is the most interesting part of the sample. In this slice there is an inward flux of hydrogen ion due to electrolysis reaction (2.2a):

$$\bar{J}_{H^+} = \frac{j}{F} = 4.146 \cdot 10^{-7} \text{ mol/s} , \tag{6.4}$$

where $j = 40$ mA is the imposed electric current, and $F = 96485.3415$ C/mol is the Faraday's constant.

The final values, after 330 hours, are reported in Table 6.5.

Table 6.5: Results of the Point Volume Model.

Specie	Value
H^+	$0.202 \cdot 10^{-4}$ mol/l
OH^-	$4.937 \cdot 10^{-10}$ mol/l
CO_3^{2-}	$3.068 \cdot 10^{-9}$ mol/l
HCO_3^-	$0.124 \cdot 10^{-2}$ mol/l
Ca^{2+}	1.584 mol/l
$H_2CO_3^*$	0.05 mol/l
p_{CO_2}	1.633 atm

The final pH value is about 4.5, similar to the average between the measurements at the boundaries of the slice (1-7). The final void ratio is 1.20, which is close to the experimental results ($1.1 \div 1.25$) showed in Figure 6.17. The final value of calcite fraction 4% is not too far from the measured values ($7 \div 8\%$).

The change in void ratio estimated by the REV model is due to the dissolution/precipitation of calcite. Thus the final void ratio and the final value of calcite fraction should have the same difference with respect to the measured values. Therefore, the results of void ratio and calcite apparently conflict with each others. The final value of calcite fraction suggests an overestimation of dissolution by the REV model, which is probably due to the absence of the transport process. It means that the dissolution of calcite is not the only cause of change in void ratio, but the

changes in void ratio are also due to the hydro-mechanical strain induced by the desaturation process arising from the dissolution of calcite.

6.3.4 Post-treatment oedometric tests

Six oedometer tests were performed on Scanzano clay at the Soil Mechanics Laboratory of the Politecnico di Milano (Figures 6.19). Four of them were performed on the slices sampled from test CBC in order to analyse the hydraulic and mechanical consequences of the filtration test. In the following the four slices are referred to as: Anode ($0 \div 30$ mm from anode), Anode Center ($30 \div 60$ mm from anode), Cathode Center ($60 \div 90$ mm from anode) and Cathode ($90 \div 120$ mm from anode). Two tests were performed on untreated soil to provide a reference for the behaviour of the natural soil. Samples were subjected to one-dimensional compression increasing the vertical load in steps up to a final value of 1600 kPa. The load steps start from 10 kPa and are increased following a geometric progression (10-25-50-100-200-400-800-1600). Samples were then unloaded following the same loading steps.

The logarithmic compliances λ and κ were estimated by regression in the e-$\log \sigma_v$ plane (Fig. 6.19). The preconsolidation vertical stress was estimated by the Casagrande procedure. The values estimated are summarised in Table 6.6.

Table 6.6: Stiffness.

Sample	λ	κ	σ_v^c
Untreated consolidated	0.308	0.084	61.66
Anode	0.350	0.065	131.1
Anode Center	0.329	0.073	117.9
Cathode Center	0.381	0.009	623.7
Cathode	-	-	-

The estimated values show that the stiffness of the untreated and the anodic half (Anode and Anode Center) are comparable. However the preconsolidation stress of the anodic half is higher than the preconsolidation stress of the untreated sample. The estimated values also show that, along the virgin loading branch, the stiffness of the third sample (Cathode Center) is not much different from the others

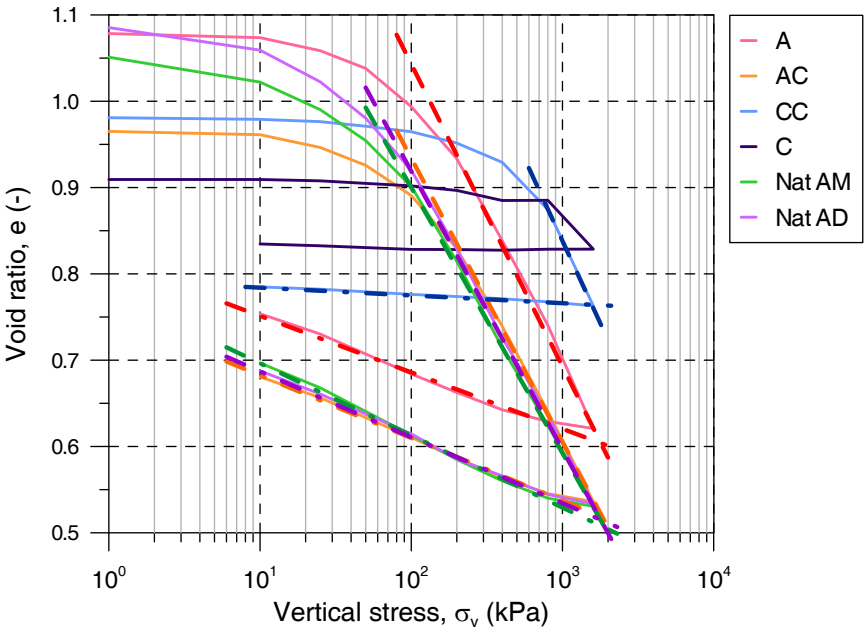

Figure 6.19: Void ratio versus vertical stress. Legend: A = Anode, AC = Anode Center, CC = Cathode Center, C = Cathode, Nat AM = Untreated, Nat AD = Untreated.

but its preconsolidation stress is much higher than the others. This fact supports the idea that the cathodic half eventually presents a cemented matrix, which can be destructurated when the preconsolidation stress is overpassed. However the value for the third sample was estimated using data of only one step (800 – 1600 kPa). Due to its "strange" behaviour, no value for the Cathode sample was estimated.

6.4 A constitutive model for Scanzano clay

The experimental evidence presented in Sections 6.2 and 6.3.4 suggests that an elastoplastic constitutive model is suitable for reproducing the coupled hydro-mechanical unsaturated behaviour of Scanzano Clay. A simplified version of the Romero and Jommi (2008) model will be adopted. Its conceptual bases stem from the proposal by Jommi and di Prisco (1994). The original Romero and Jommi (2008) model was designed to reproduce plastic anisotropic response under wetting-drying cycles. Since the available experimental data do not allow for quantifying possible

anisotropic features, a modified model, with non-associated plastic potential, was adopted instead of the rotating yield function.

The hysteretic retention curve defined in Section 6.1 is introduced in the coupled hydromechanical model, in order to reproduce cyclic wetting and drying paths correctly (Tamagnini, 2004). A hysteretic retention curve will prove to be quite important in modelling the mechanical response of the soil undergoing drying and wetting paths, as the following numerical simulations will demonstrate with reference to the experimental data discussed.

Yield surface

Since the peak strength of overconsolidated clays is described by the Hvorslev envelope (Hvorslev, 1960), it is well known that the yield surface of the modified Cam Clay model (Roscoe and Burland, 1968) overestimates the peak strength of overconsolidated clays. To avoid this problem different yield surfaces were proposed in the past (Banerjee and Stipho, 1979; Lade and Kim, 1988, e.g.). Bigoni and Piccolroaz (2004) proposed a convex yield function which posseses an extreme shape variation in order to fit experimental results. Moreover this yield function is able to approach known yield criteria. The yield surface of the proposed model is defined by just substituting the soil skeleton stress for effective stress in the form of Bigoni and Piccolroaz (2004):

$$f = q^2 - M_f^2 \hat{p}_0^2 (\Phi - \Phi^{m_f})(2(1 - r_f)\Phi + r_f) = 0 \,, \tag{6.5}$$

where $\hat{p}_0$ is the preconsolidation pressure in unsaturated conditions, $\Phi = \hat{p}/\hat{p}_0$, M_f, m_f and r_f are parameters which define the shape of the yield function.

Plastic potential

The plastic potential is described by a similar functionto that adopted for the yield surface, which is defined by means of different parameters:

$$g = q^2 - M^2 (\hat{p}_c^g)^2 (\Phi_g - \Phi_g^{m_g})(2(1 - r_g)\Phi_g + r_g) = 0 \,, \tag{6.6}$$

where M describes the slope of the critical state line. On the critical state line (CSL) $q = Mp$ and dilatancy is null, e.g. $\partial g/\partial \hat{p} = 0$. When adopting the Bigoni and Piccolroaz function to describe the plastic potential the position of the point with null derivative, $\partial g/\partial \hat{p} = 0$, is not assured to be on the $q = Mp$ line. Therefore fixing one of the two parameters governing the shape of the function, m or r, the other parameter could be computed in such a way that the condition $\partial g/\partial \hat{p} = 0$ at $q = Mp$ holds.

Although the assumption of a constant value of M, independent of suction, is still a matter of debate, experimental results presented before (Fig. 6.8) and data from literature (see, e.g., the data collection presented by Nuth and Laloui, 2008) suggest that it can hold true .

The shape of the plastic potential can be determined starting from the stress-dilatancy relationship.

Loading-Collapse

Taking advantage of the suggestion by Gallipoli et al. (2003a), the preconsolidation pressure in unsaturated conditions, $\hat{p}_0$, is defined as the sum of the preconsolidation pressure in saturated conditions, p_0^*, depending on volumetric plastic strains, plus a term also depending on the degree of saturation:

$$\hat{p}_0 = p_0^* \left(1 + b_1 \left(e^{b_2(1-Sr)} - 1\right)\right) \ , \tag{6.7}$$

where b_1 and b_2 are model parameters ruling the dependence of preconsolidation pressure on the degree of saturation. Equation (6.7), together with the expression of WRC, define the so-called *Loading-Collapse* curve.

Hardening

For the evolution of p_0^*, the classical critical state evolution law is adopted:

$$\mathrm{d}p_0^* = \frac{1+e}{\lambda - \kappa} p_0^* \, \mathrm{d}\varepsilon_{vol}^p \ , \tag{6.8}$$

where λ and κ are the elastic-plastic and elastic logarithmic volumetric compliances, respectively, and e is the void ratio.

6.4.1 Calibration of the parameters

Logarithmic Compliance

The isotropic compression stage of saturated triaxial tests (Fig. 6.20) allows to define the *normal compression line* (NCL),

$$v = N - \lambda \log \hat{p} \ , \tag{6.9}$$

and the elastic logarithmic compliance κ with reference to an unloading-reloading cycle. The values $N = 2.535$, $\lambda = 0.1405$ and $\kappa = 0.034$ were determined. As

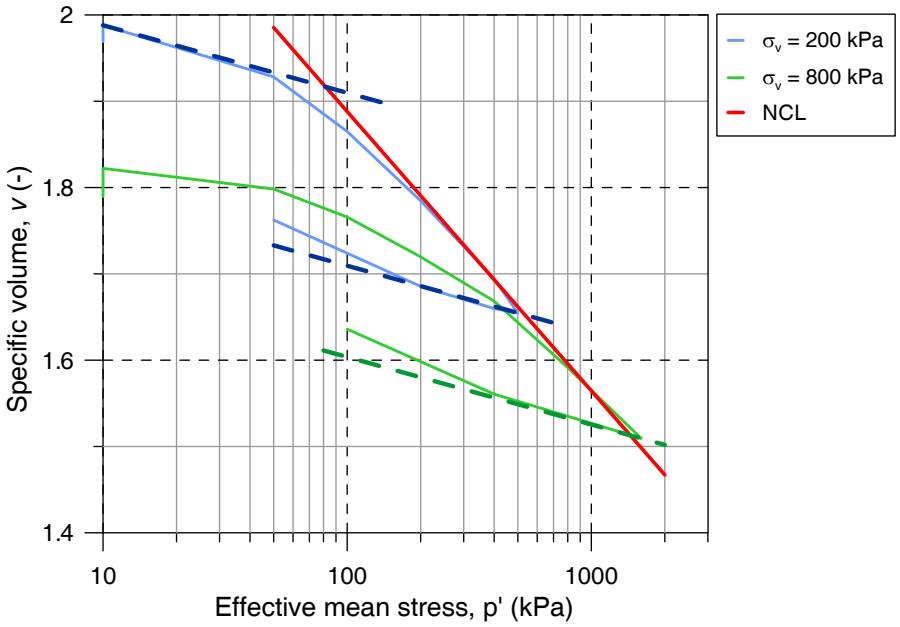

Figure 6.20: Normal compression line.

expected, in the plane $\log \hat{p} - v$ the NCL is parallel to the CSL.

Yield surface and plastic potential shape

The shapes of the yield surface and of the plastic potential were estimated starting from the results of the undrained triaxial tests on the overconsolidated samples

(Fig. 6.4). For each test the yield stress and the dilatancy at yield were estimated (Fig. 6.21). Since for each test the size of the elastic domain is unique, and different from that of the other tests (i.e. in each test the preconsolidation pressure is different from that of the others), yield stresses were normalised to the relevant value of $\hat{p}_c$ at the beginning of the shearing stage. In Table 6.7 the values which best fit the

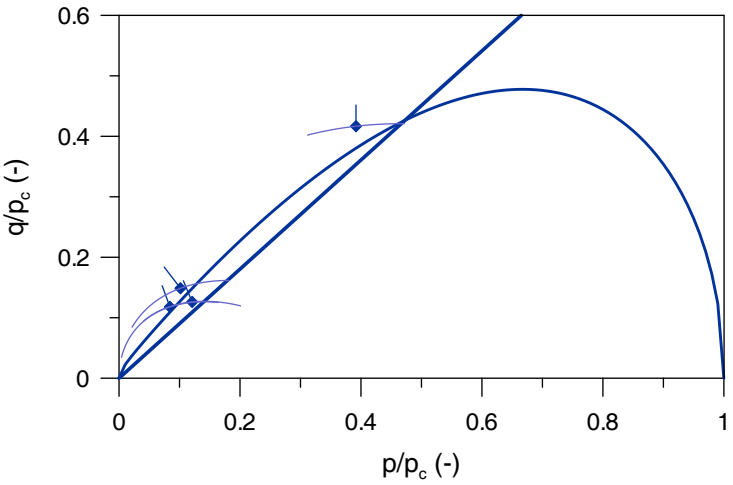

Figure 6.21: Yield surface shape.

experimental data are reported.

Table 6.7: Parameters of yield function and plastic potential.

M_f	m_f	r_f	m_g	r_g
0.95	2.1	0.05	1.6	1.15

Loading-Collapse

Parameters b_1 and b_2 were estimated from the yield vertical stress in the oedometer tests at constant suction:

$$\hat{\sigma}_{v0} = \sigma^*_{v0}\left(1 + b_1\left(e^{b_2(1-Sr)} - 1\right)\right) . \tag{6.10}$$

Parameters b_1 and b_2 of the previous equation are the same of Eq. 6.7 if the assumption of constant earth pressure coefficient, K_0, is introduced. Values which

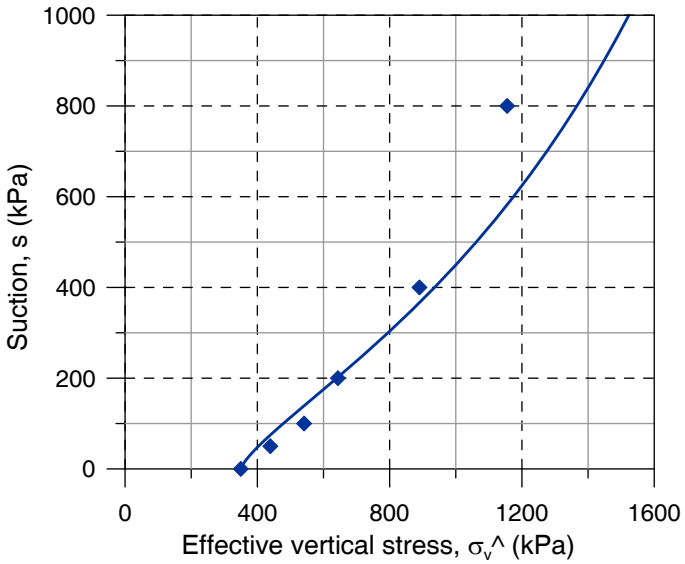

Figure 6.22: Loading-Collapse curve.

best fit experimental data are $b_1 = 25$ and $b_2 = 0.4$, giving the so-called loading-collapse curve depicted in Figure 6.22.

6.4.2 Comparison with experimental results

The constitutive model was implemented within the procedure outlined in Chapter 4. The constitutive equations were integrated by means of an implicit algorithm.

Comparison between experimental data and the numerical results for the oedometer tests at constant suction are presented in Figure 6.23. The model is able to reproduce the re-loading branch, in particular the non linear behaviour in the $\ln p' - e$ plane. Also the value of void ratio at the end of the loading paths are caught reasonably well, although it is overestimated at the lower suction. This may be due to the retention curve adopted, which does not depend on void ratio. At high suction the stiffness is such that the change in void ratio does not affect the water retention curve. At the opposite, at low suction the change in void ratio results in a change in the degree of saturation at constant suction.

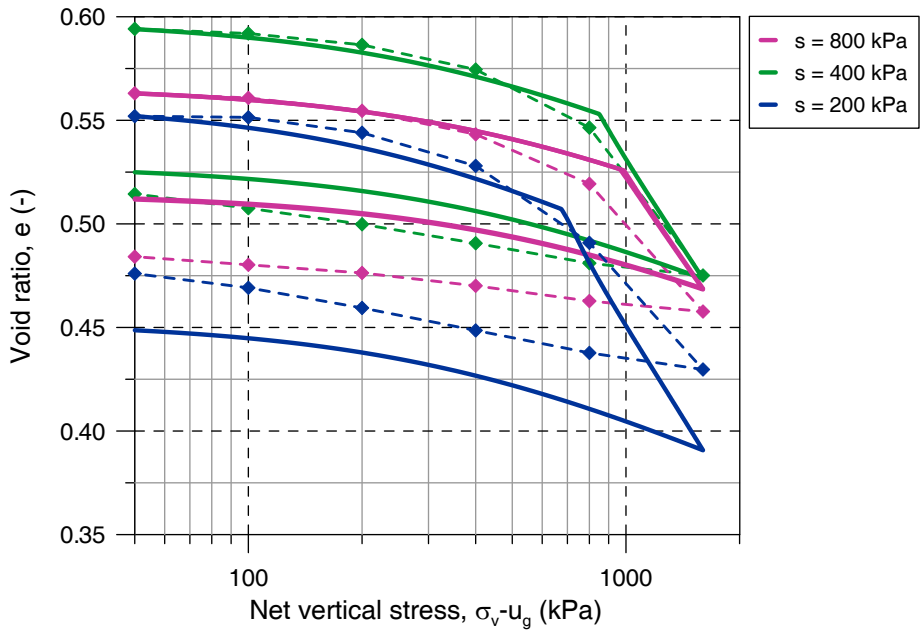

Figure 6.23: Unsaturated oedometric tests.

Comparison between experimental data and the numerical results for undrained triaxial tests is presented in Figures 6.24-6.27. In the same figures, predictions of the proposed model are also compared to those aobtained with a standard modified Cam-Clay model (Roscoe and Burland, 1968).

In Figures 6.24 and 6.25 two of the undrained triaxial tests on normally consolidated samples are shown. The proposed model is able to reproduce both the critical state and the pre-failure response. On the contrary, the modified Cam-Clay model underestimates the deviator stress at critical state and overestimates the increment of the pore pressure.

In Figures 6.26 and 6.27 two of the undrained triaxial tests on overconsolidated samples are shown. The first test (Fig. 6.26) was performed on a lightly overconsolidated sample ($\hat{p}_0 = 100$ kPa, $\sigma_v^{max} = 200$ kPa). The proposed model is able to reproduce the value of the deviator stress at critical state, although it fails in reproducing the pre-failure behaviour (Fig. 6.26a). This fact is due to the choice of constant shear elastic modulus, which does not depend on the confining pressure. The final value of the pore pressure is underestimated, although the qualitative

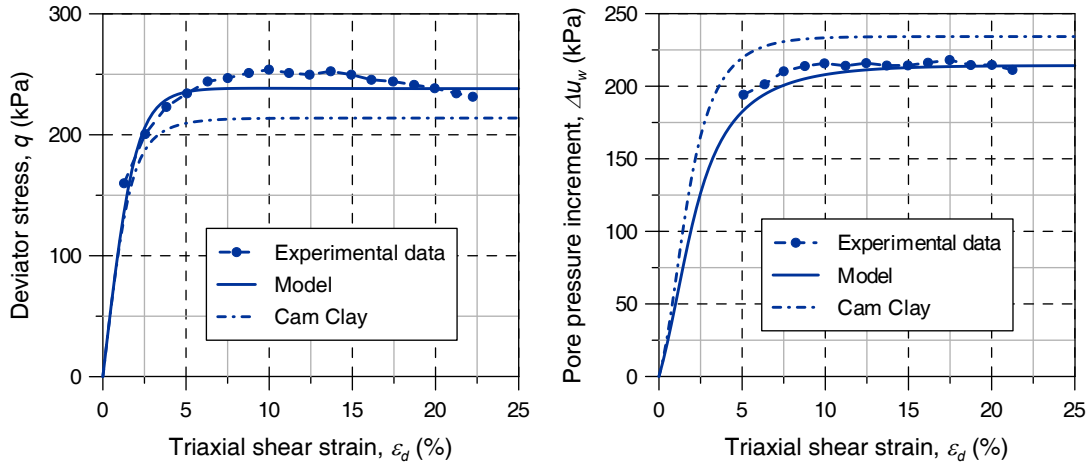

Figure 6.24: Test PR14b

prediction is correct. The second test (Fig. 6.27) was performed on a heavy over-consolidated sample ($\hat{p}_0 = 200$ kPa, $\sigma_v^{max} = 800$ kPa). The results of the numerical simulation confirm the robustness of the proposed model. Even if the qualitative description is not caught as well as in the previous examples, the proposed model is still a great improvement with respect to the modified Cam-Clay model.

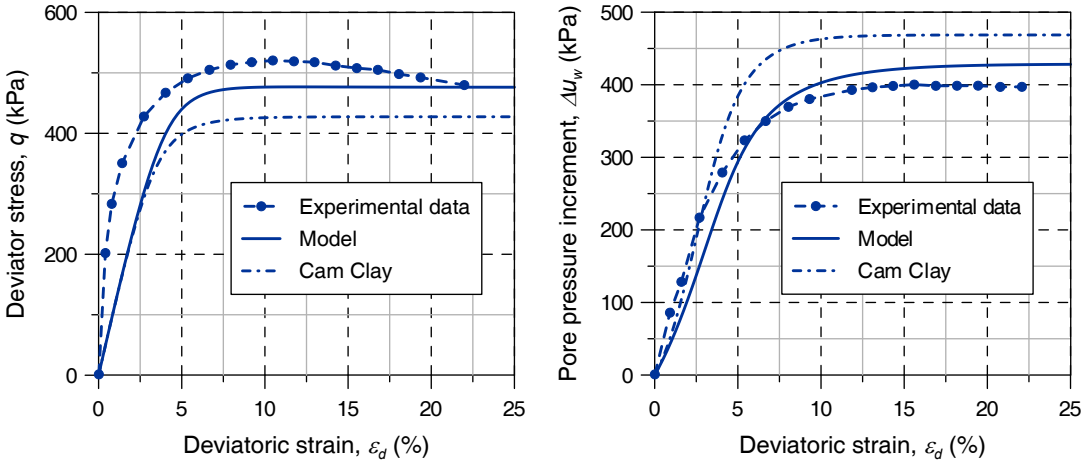

Figure 6.25: Test PR22a

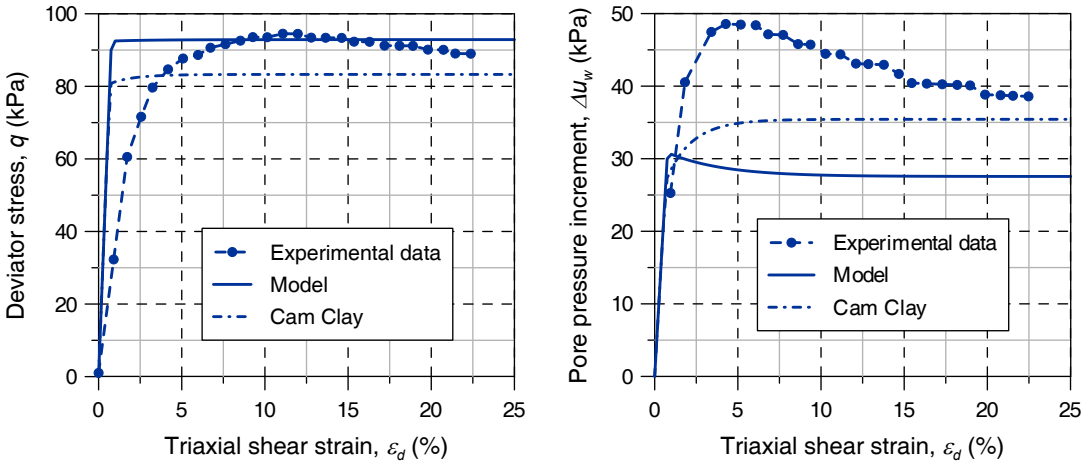

Figure 6.26: Test PR14a

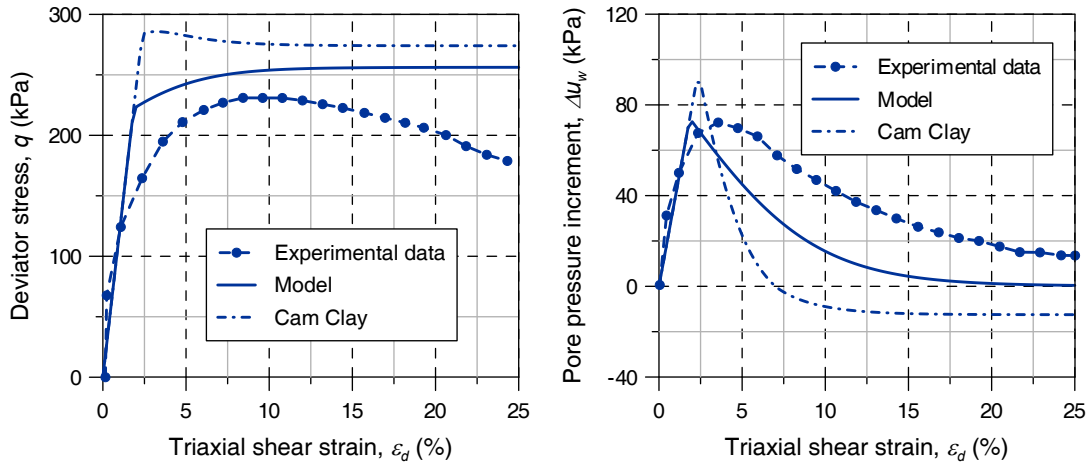

Figure 6.27: Test PR19a

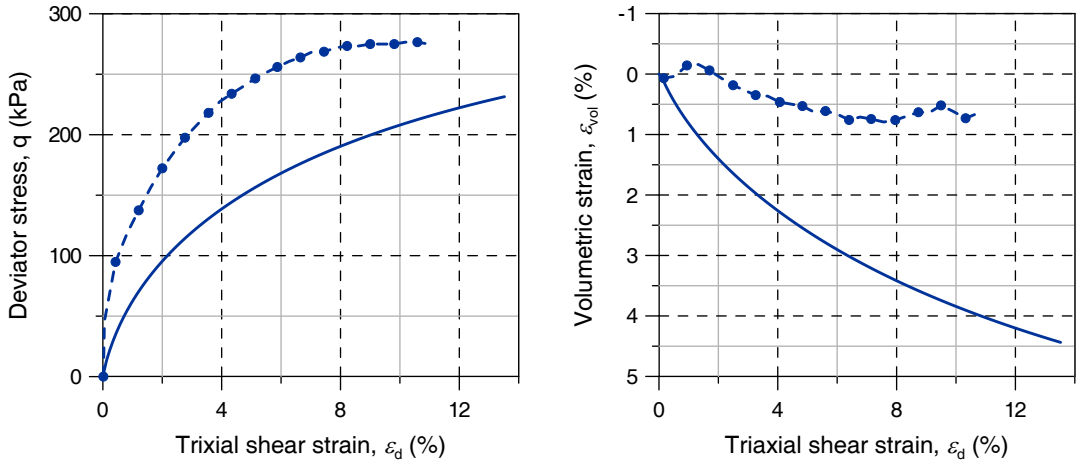

Figure 6.28: Test A3

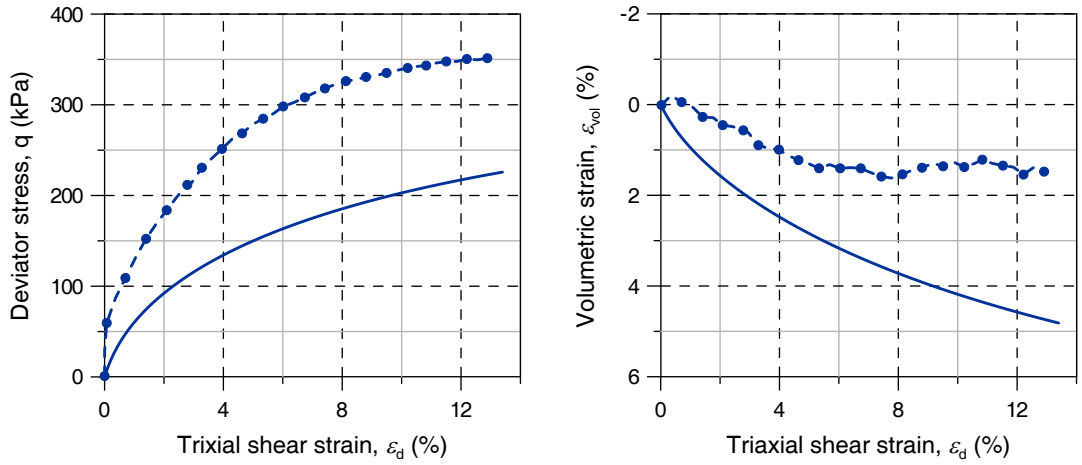

Figure 6.29: Test A7

7 Finite element modelling

In Chapter 3 the equations governing the electrokinetic processes were described. Since they are strongly coupled, numerical methods are mandatory for their solution. The most popular methods for the solution of transient nonlinear problems are the *finite difference* (FD) and the *finite element method* (FEM). In particular the finite element method has demonstrated its suitability for the solution of transient nonlinear problems.

In this Chapter, after a brief review of the available methods to solve the reactive transport problem, the governing equations will be discretised by the finite element method. Finally the results of the numerical model are presented.

7.1 Weak form

The governing equations of the coupled hydro-electro-chemo-mechanical problem have been discussed in Chapter 3 and they are summarised in Table 7.1.

For each balance equation the spaces of trial and test functions are defined. Following standard arguments the weak form of the coupled problem is implemented. Introducing a suitable spatial discretisation of the domain into finite elements, a standard Galerkin FE approximation for the unknown fields $\mathbf{u}$, u_l, c_i, p_i and Φ leads

Table 7.1: Governing equations.

Balance equation		Constitutive equation	
$\frac{\partial n Sr \rho_w}{\partial t} + \nabla \cdot (\rho_w \mathbf{v}_l) = 0$	(3.28)	$\mathbf{v}_l = -\frac{\boldsymbol{\kappa} k_l^{rel}}{\mu_w} (\nabla u_l + \rho_w g \boldsymbol{\delta}_{zx}) - \boldsymbol{k_e} k_e^{rel} \nabla \Phi$	(3.7)
		$Sr = Sr(s)$	(3.40)
$\frac{\partial n Sr c_i}{\partial t} + \nabla \cdot \mathbf{J}_i + nSrR_i = 0$	(3.29)	$\mathbf{J}_i = -\mathbf{D}_i^* \nabla c_i - c_i \frac{\boldsymbol{\kappa} k_l^{rel}}{\mu_w} (\nabla u_l + \rho_w g \boldsymbol{\delta}_{zx})$ $-c_i \left(\boldsymbol{k_e} k_e^{rel} + \mu_i^* \right) \nabla \Phi$	(3.18)
$\frac{\partial (n \rho_i (1 - (1 - h_i) Sr))}{\partial t} + \nabla \cdot \left(\rho_i (\mathbf{v}_g + h_i \mathbf{v}_l) \right) + nSrm_i^{mol} R_i = 0$	(4.10)	$\mathbf{v}_g = -\frac{\boldsymbol{\kappa} k_g^{rel}}{\mu_g} \left(\nabla u_g + \rho_g z \boldsymbol{\delta}_{zx} \right)$	(3.8)
		$\rho_i = \rho_i^0 \frac{p_i}{p_{atm}}$	(3.9)
		$Sr = Sr(s)$	(3.40)
$\frac{\partial \bar{c}_i}{\partial t} + nSrR_i = 0$	(3.34)	No movement	
$\nabla \cdot \mathbf{j} = 0$	(3.37)	$\mathbf{j} = -\sigma^* \nabla \Phi - \sum_{i=1}^{N} z_i F \mathbf{D}_i^* \nabla c_i$	
$\nabla \cdot \hat{\boldsymbol{\sigma}} - \nabla (Sr\, u_l + (1 - Sr) u_g) + \mathbf{b} = 0$	(3.60)	$\boldsymbol{\varepsilon} := -\frac{1}{2} \left(\nabla \mathbf{u} + (\nabla \mathbf{u})^T \right)$	(3.61)
		$\hat{\boldsymbol{\sigma}} = \sigma (\hat{\boldsymbol{\sigma}}, \boldsymbol{\varepsilon})$	(3.62)

to the following matrix form:

$$\dot{\mathbf{S}}_w + \mathbf{K}_w \mathbf{u}_l + \mathbf{G}_w + \mathbf{C}_{we}\mathbf{\Phi} + \mathbf{F}_w = \mathbf{0} \tag{7.1a}$$

$$\dot{\mathbf{S}}_i + \mathbf{D}_i \mathbf{c}_i + \mathbf{M}_i \mathbf{c}_i - \mathbf{V}\mathbf{c}_i + \mathbf{c}_i + \mathbf{R}_i = \mathbf{0} \qquad i = 1, \cdots N_d \tag{7.1b}$$

$$\dot{\mathbf{S}}_i + \mathbf{K}_{ij} \mathbf{p}_j + \mathbf{G}_i + \mathbf{C}_{iw}\mathbf{u}_l + \mathbf{C}_{ie}\mathbf{\Phi} + \mathbf{R}_i + \mathbf{F}_i = \mathbf{0} \qquad i = 1, \cdots N_g \tag{7.1c}$$

$$\dot{\mathbf{S}}_i + \mathbf{R}_i = \mathbf{0} \qquad i = 1, \cdots N_m \tag{7.1d}$$

$$\mathbf{K}_e\mathbf{\Phi} + \mathbf{F}_e = \mathbf{0} \tag{7.1e}$$

$$\mathbf{d} + \mathbf{C}\mathbf{u}_l = \mathbf{0} \tag{7.1f}$$

where $\mathbf{u}$ is the nodal displacement vector, $\mathbf{u}_l$is the nodal pore liquid pressure vector, $\mathbf{c}_i$ is the nodal concentration of the i-th chemical species, $\mathbf{p}_i$ is the nodal gas pressure of the i-th gaseous chemical species and $\mathbf{\Phi}$ is the nodal electric potential vector.

7.2 Time discretisation

In thìtacking time discretisation the following definitions will be used:

- the time step n is bounded by t^n and t^{n+1} and its length is $\Delta t = t^{n+1} - t^n$;
- for a generic function f, f^n denotes its approximation at time t^n;
- given parameter $\theta \in [0, 1]$, the convention $f^{n+\theta} = (1 - \theta)f^n + \theta f^{n+1}$ holds;

7.3 Coupling chemical reactions with transport process

To solve the multicomponent reactive transport problem 'ad hoc" numerical approaches have been proposed because: (i) the reactive transport model involves a large number of variables and, hence, of equations; (ii) because of the nonlinear behaviour due to the nature of the model equations; (iii) because of the coupled nature of the resulting system of equations. The most notable methods are:

- *Direct substitution approach* (DSA);

- *Sequential non-iterative approach* (SNIA);
- *Sequential iterative approach* (SIA);
- *Fully kinetic approach*.

Basically, the various methods can be divided into two groups (Saaltink et al., 2004):

- operator splitting, also called the two-step approach. This group includes the Sequential Iteration Approach and the Sequential Non-Iteration Approach. In these techniques, the mass balance equations of the reactive species are split in two parts and each part is solved separately.
- single-step methods, which include the Direct Substitution Approach and the Global Implicit Approaches. In this group of approaches, the chemical equations are substituted into the transport equations, and the latter are then solved simultaneously, employing Newton-Raphson or Picard schemes. The obvious disadvantage is the need to solve many equations simultaneously, resulting in high computational costs.

In the last decades a large number of scientists compared these approaches (Saaltink et al., 2001; Steefel and MacQuarrie, 1996; Yeh and Tripathi, 1989, among others). As a general rule, the DSA is more robust than the SIA, in the sense that it is less sensitive to time step size, to kinetics or large flux rates than the SIA (Saaltink et al., 2001). Moreover the DSA is the best choice for the simulation of sharp fronts, since the SIA require fine grids and very small time steps to converge. In terms of computational costs the system of equations is much larger for the DSA than for the SIA, tehrefore the DSA may lead to excessive memory requirements for large grids. Moreover the CPU time for the SIA increases linearly up to a large number of nodes, whereas that for the DSA start to grow with an order of 2 from a much smaller number of nodes (Saaltink et al., 2001). This means that for large grids, especially for two- and three-dimensional problems, the DSA tends to be less favourable. A clear advantage of the operator splitting techniques is the possibility of parallel computation (Hundsdorfer and Verwer, 1995). When some components are independent, their transport equations could be uncoupled. Uncoupling allows

to solve them separately, thus reducing the size of DSA systems of equations, and would not cause convergence difficulties, thus reducing the number of iterations for SIA (Molins et al., 2004). Starting from this considerations, Robinson et al. (2000) proposed a selective coupling method that solves separately the transport equations for lightly coupled components (in a SIA fashion) and solves with a monolithic procedure the strongly coupled equations (in a DSA fashion).

It is clear that no method can be considered better than the others in any case. The choice of the solving scheme depends on the problem to be solved. For instance, the SIA may become faster than the DSA for very large but chemically simple problems. In fact, in this case, the two methods tend to require the same number of iterations but the size of the system of equations is much larger for the DSA than for the SIA.

In the following Sections the different methods will be briefly described. In order to clarify the notation, the mass balance equations in the following will be written with reference to saturated conditions and using the transport operator $\mathcal{L}$ for chemical species. For the electrokinetic problem the transport operator is defined as:

$$\mathcal{L}(c_i) := \nabla \cdot (-D_i \nabla c_i + z_i c_i \nabla \Phi + c_i v_l) \, . \tag{7.2}$$

Thus the mass balance equation of each chemical species can be written in compact form as

$$\frac{\partial c_i}{\partial t} + \mathcal{L}(c_i) + R_i = 0 \, . \tag{7.3}$$

7.3.1 Direct substitution approach

As described before, the DSA is the best choice for coupled problems with high non-linearities and sharp fronts.

The basic concepts of the DSA were described in Section 5.4 with reference to REV approach. When the DSA is applied to transport processes the assumption of linear transport operator has to be introduced. This assumption is reasonable when advection due to liquid flow is the predominant transport process of the chemical species. In Section 3.4.4 it has been showed that electrically driven flow of chemical species dominates the transport process in low permeability soils. Thus the DSA

is not suited to problems where the chemical reaction problem is coupled with electrokinetic processes.

7.3.2 Sequential non-iterative approach

At the other extreme from the one-step or global implicit method stands the sequential non-iterative approach (SNIA), also called operator splitting or time splitting approach. In this approach, a single time step consists of a transport step followed by a reaction step using the transported concentrations. Physically, one can think of the method as equivalent to taking part of the contents of one beaker (i.e. one node) and adding it to a second beaker downstream. After this physical process is completed, reactions occur which modify the chemical composition of each of the beakers in the sequence.

Different implementation procedures of this method have been proposed.

Classic formulation

Mathematically, the method can be represented as a two step sequential process consisting of a transport step:

1. first the transport problem is solved

$$\frac{\partial \mathbf{c}^T}{\partial t} + \mathcal{L}(\mathbf{c}^T) = 0 \,, \tag{7.4}$$

   which results are the transported concentrations $\mathbf{c}^T$;

2. the transported concentrations $\mathbf{c}^T$ are the initial conditions of the reaction problem

$$\frac{\partial \mathbf{c}}{\partial t} + R = 0 \,, \tag{7.5}$$

   the solution of which is the converged solution at the end of the step.

Strang splitting

The Strang splitting (Strang, 1968) allows to reduce some of the errors associated with the SNIA approach (Steefel and MacQuarrie, 1996). Basically it is a time-

centered method where the reaction step is solved between two transport steps.

7.3.3 Sequential Iterative Approach

The SIA is a refinement of the SNIA. The SIA iterates between transport and reaction step until they provide the same solution. The solution procedure at the i-th iteration is:

1. first the transport problem is solved taking into account the reaction rates computed from the previous iteration:

$$\frac{\partial \mathbf{c}^{i,T}}{\partial t} + \mathcal{L}(\mathbf{c}^{i,T}) + R^{i-1,R} = 0 \tag{7.6}$$

   which results is $\mathbf{c}^{i,T}$;

2. the reaction problem is solved using the transport term computed before:

$$\frac{\partial \mathbf{c}^{i,R}}{\partial t} + \mathcal{L}(\mathbf{c}^{i,T}) + R^{i,R} = 0 \tag{7.7}$$

   which results is $\mathbf{c}^{i,R}$;

3. the step is solved when $\mathbf{c}^{i,T} = \mathbf{c}^{i,R}$.

7.3.4 Law of mass action

In the analysis presented in the following, the choice was to adopt the pseudo-kinetic approach, based on the law of mass action, which was described already in Section 5.4 with reference to the REV method. The choice seems to be sufficiently general and applicable in a straightforward way to FE models, provided a preliminary sensitivity analysis on the forward and backward reaction rates is performed to evaluate their most convenient numerical values.

7.4 Numerical implementation

The model equations were implemented in the finite element platform COMSOL Multiphysic v3.4 . Linear elements were adopted for the field variables (pore pressures, voltage and species concentrations).

Time integration was performed using a fifth order, variable step-size, implicit backward differentiation formula.

The one dimensional model of the 12 cm long specimen consists of 300 elements, equally spaced. The analysis models the evolution of an electrokinetic filtration test for a duration of 300 hours.

No stabilisation techniques of the numerical procedure were adopted.

7.4.1 Initial conditions

In Section 6.3.3 the initial concentration of the chemical species in aqueous solution was calculated starting from the initial measured pH. Values are reported in Table 6.4.

7.4.2 Boundary conditions

Constant electric current density was imposed at the anodic boundary, while a null potential was assumed at the cathode:

$$j_c^{an} = 0.8 \text{ mA/cm}^2 \tag{7.8a}$$

$$\Phi^{cat} = 0 \text{ V} \tag{7.8b}$$

Though hydraulic conditions are not constant during the test, a constant water pressure of 5 kPa was imposed at both the anodic and the cathodic boundaries:

$$u_w^{an} = 5 \text{ kPa} \tag{7.9a}$$

$$u_w^{cat} = 5 \text{ kPa} \tag{7.9b}$$

As for the chemical species that partecipate to the carbonic acid system ($H_2CO_3^*$, HCO_3^-, CO_3^{2-}, Ca^{2+}), in light of the fact that no relevant contribution is given

by hydraulic gradients as already demonstrated, no inward flux was allowed at the anodic boundary, while at the cathode they may be transported outwards by convection due to the liquid phase flow:

$$j_i^{an} = 0 \text{ mol/l s} \tag{7.10a}$$

$$j_i^{cat} = c_i v_w \tag{7.10b}$$

Since calcite is a solid specie, it will no be transported. No boundary conditions are needed for calcite.

Water electrolysis can be modelled by an inward flux of H^+ at the anode and of OH^- at the cathode (Eqs. 2.2). Faraday's laws of electrolysis relates the quantity of a substance altered at an electrode during electrolysis to the quantity of electricity transferred at that electrode. Ffor water electrolysis it reads

$$j_{H^+,OH^-} = \frac{j_c \eta}{F} , \tag{7.11}$$

where η is the efficiency of the electrolysis.

No inward flux was allowed at the anodic boundary for the hydroxyl, while at the cathode the hydrogen ion may be transported outflow by convection due to the liquid phase flow.

In the filtration cell the outer cell and side plates confine the sample. The sample cannot expand due to the cell walls constraint, but in principle, contraction is not constrained. Mathematically this condition could be written

$$\begin{cases} u = 0 & \text{if } \dot{\varepsilon} < 0 \\ \sigma = 0 & \text{if } \dot{\varepsilon} \geq 0 \end{cases} . \tag{7.12}$$

Since this is a "stiff" boundary condition (i.e. it is not simple to impose), the simple boundary condition

$$u = 0 \tag{7.13}$$

is assumed. This condition leads to the onset of traction strain when the sample contracts. Adopting linear elasticity, traction strain are accompanied by traction stresses which are unrealistic, but which can help in explaining the observed cracks.

Table 7.2: Properties of chemical species.

Specie	D $[m^2\,s^{-1}]$	u $[m^2\,s^{-1}\,V^{-1}]$	z [-]	m $[g\,mol^{-1}]$
H^+	$9.31 \cdot 10^{-9}$	$3.63 \cdot 10^{-7}$	+1	1
OH^-	$5.264 \cdot 10^{-9}$	$2.05 \cdot 10^{-7}$	−1	17
HCO_3^-	$1.185 \cdot 10^{-9}$	$4.615 \cdot 10^{-8}$	−2	61
CO_3^{2-}	$9.579 \cdot 10^{-10}$	$7.46 \cdot 10^{-8}$	−2	60
Ca^{2+}	$7.909 \cdot 10^{-10}$	$.16 \cdot 10^{-8}$	+2	40
$CaCO_3$	-	-	-	100
CO_2	-	-	-	40

7.5 Parameters estimation

Relevant properties of the chemical species considered in the model are reported in Table 7.2.

Absolute hydraulic permeability is $5.1 \cdot 10^{-17}$ m^2 . The hydraulic relative permeability was assumed to depend on the degree of saturation via a power law of the type:

$$k_w^{rel} = Sr^{b_w} \ . \tag{7.14}$$

A value of $b_w = 3$ was assumed for the relative hydraulic permeability of Scanzano clay. Consistently with the previous choice for water, a power law was adopted also to describe the relative permeability of gas

$$k_g^{rel} = (1 - Sr)^{b_w} \ . \tag{7.15}$$

A value of $2 \cdot 10^{-9}$ $m^2/V\,s$ for the absolute electro-osmotic permeability was estimated by Gabrieli et al. (2008b). The relative electro-osmotic permeability was estimated starting from experimental results of electrokinetic filtration tests performed on unsaturated specimens in the as-compacted state (Fig. 7.1). Their experimental data suggest that also the electro-osmotic permeability may be assumed to depend on the degree of saturation via a power law:

$$k_e^{rel} = Sr^{b_e} \ , \tag{7.16}$$

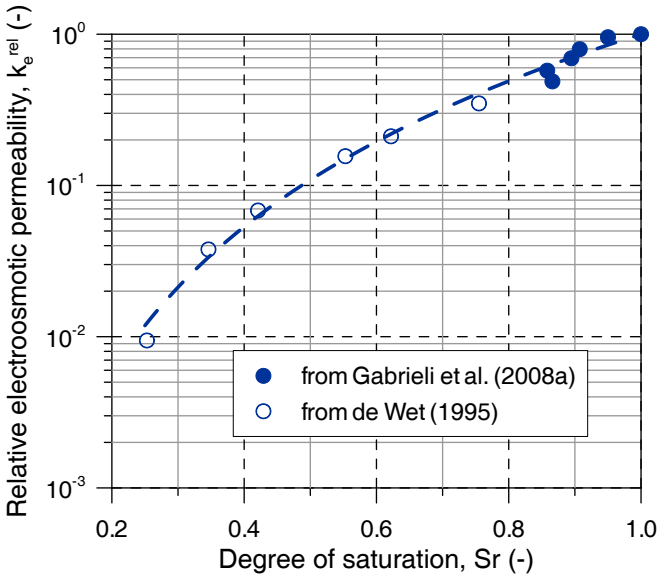

Figure 7.1: Relative electro-osmotic permeability

with the value of $b_e = 3.2$ for the exponential.

The water retention curve estimated in Section 6.1 was adopted to relate the degree of saturation to the difference between the CO_2 gas and the water pressures, $s := u_g - u_w$ (Fig. 6.1).

The mechanical tests performed on Scanzano clay (Chapter 6) suggest a value of 3000 kPa for the oedometer modulus.

7.6 Results

The total amount of water transported by the electrochemical process is depicted in Figure 7.2. The comparison between numerical prediction of outflow and experimental data show good agreement. It is interesting to note that the calculated outflow is slightly greater than the inflow one, indicating that a desaturation process is taking place during the treatment. This fact agrees with the experimental observation, which indicates that at test dismounting the samples are slightly desaturated. The time evolution of computed water saturation is represented in Figure 7.3. The numerical simulation predicts a desaturation process reaching the cathodic bound-

ary after 20 hours. Afterwards, a desaturation pattern starting from the anodic boundary and reaching a minimum in correspondence of a sort of advancing front may be appreciated.

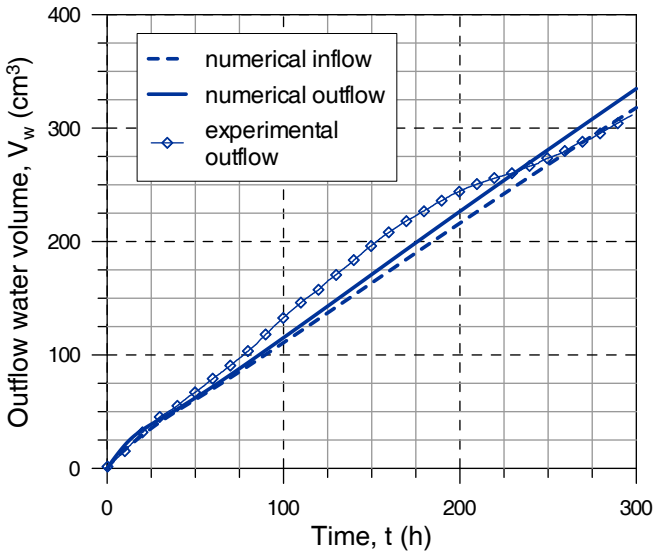

Figure 7.2: Outflow water volume: comparison between experimental data and numerical results.

The degree of saturation is uniquely linked to the suction via the water retention curve. Since in this problem the only gaseous specie is CO_2 in the following suction will be identified with the capillary pressure, defined as the difference between the CO_2 gas pressure and the water pressure. The time evolution of the two pressures is presented in Figure 7.4 and Figure 7.5.

The water pressure initially decreases near to the anodic boundary and increases close to the cathodic one. After few hours, the trend is reverted and all the sample is subjected to a negative pore water pressure, which presents an advancing minimum correspondent to the minimum saturation degree. It is worth noting that Esrig (1968) demonstrated that no excess pore pressure should develop if drainage is allowed at both electrodes (Fig. 2.4b). Nonetheless in the formulation by Esrig, gas pressure was not taken into account, nor the possible onset of desaturation. The latter factors, considered herein, promote heterogeneities along the sample, which in turn are responsible for the development of pore pressure changes. In

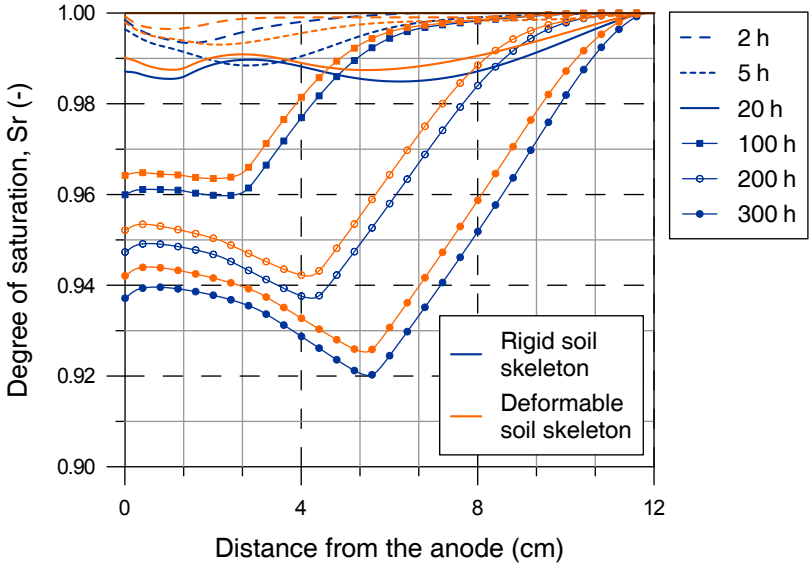

Figure 7.3: Isochrones of the degree of saturation: numerical predictions.

fact CO_2 gas pressure increases monotonically with time, starting from the anodic region, and penetrating into the sample.

The CO_2 pressure arises as a result of calcite dissolution. The comparison between the values of calcite mass fraction at test dismounting and the numerical results is reported in Figure 7.6. It can be observed that the experimental trend is very well caught, in spite of the differences in space, due to time shifting. A parallel inspection of the isochrones for calcite mass fraction and for pH, reported in Figure 7.7, suggests that calcite dissolution is appreciated when the pH reaches a value of about 3.5. For this pH value, if local chemical equilibrium is imposed disregarding gas transport, more severe CO_2 pressures than those calculated numerically are expected (Airoldi et al., 2009). It is worth noting that although the pH trend is caught correctly, there is a difference between the experimental and the measured data both on the anodic and on the cathodic side. In particular at the anodic side the pH increases, after reaching its minimum, where calcite vanishes. This fact may be explained by the presence of further buffering capacity of the soil due to other minerals than calcite, which was not taken into account in this model. The further buffering capacity may also explain the difference between the experimental and the numerical degree of saturation. The gas generated from the dissolution of

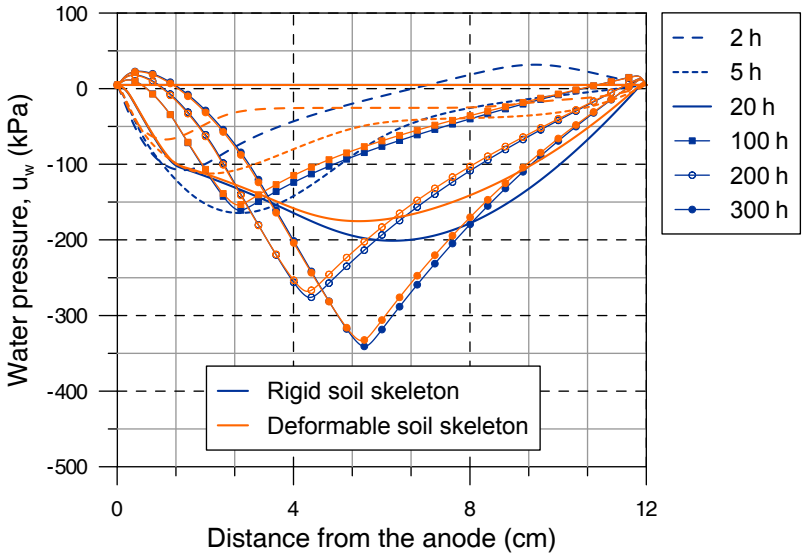

Figure 7.4: Isochrones of the water pressure: numerical predictions

minerals not taken into account increases the gas pressure contributing to sample desaturation.

Finally, the evolution of water and gas pressures are influenced not only by the chemical reactions, but also by their mass conservation laws. In particular the soil skeleton compressibility influences their values (Figs. 7.4 and 7.5). Even if equilibrium of the chemical species depends on the degree of saturation, it seems that the differences in water and gas pressures due to soil skeleton compressibility do not influence the chemical species concentration (Fig. 7.7).

The evolution of the pressure gradients in space and time guarantees the water mass conservation and counterbalance the effect of non-uniform electroosmotic transport. The electrical conductivity evolves continuously with ions concentrations (Fig. 7.8), governing the electric potential isochrones (Fig. 7.9).

When the samples were dismounted from the filtration cell, fractures were observed in the region near the anode (Fig. 6.18). This is consistent with the calculated effective stress distribution (Fig. 7.10), which presents a traction peak at 3 cm from the anode. Since soil has no tensile strength the predicted tractions cannot be sustained, an fractures, like those observed, may be opened.

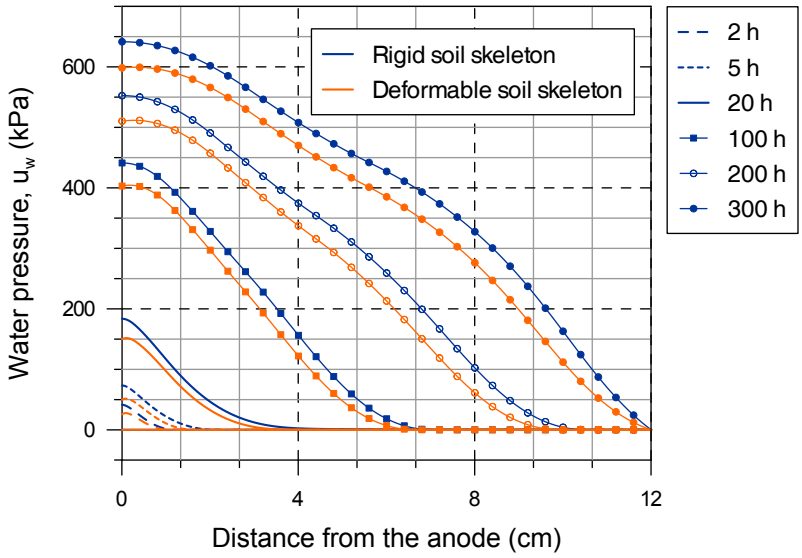

Figure 7.5: Isochrones of the CO_2 pressure: numerical predictions.

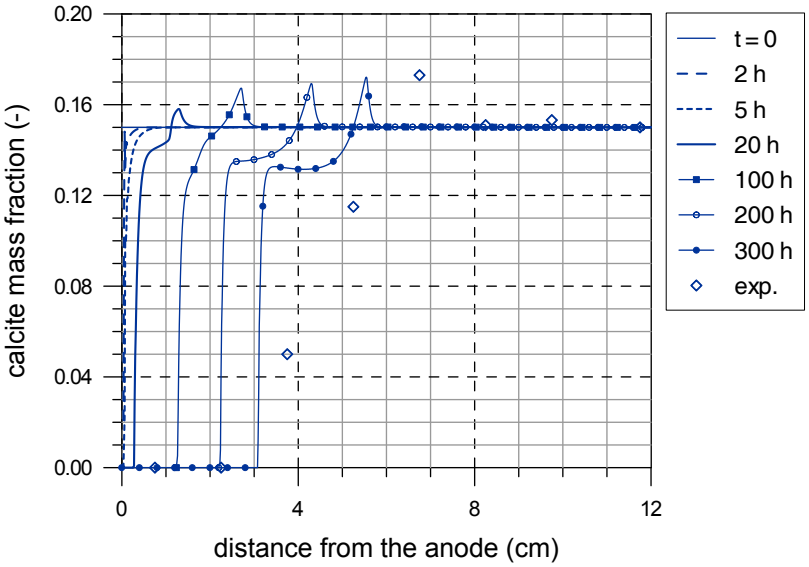

Figure 7.6: Numerical isochrones for calcite mass fraction and experimental data at test dismounting.

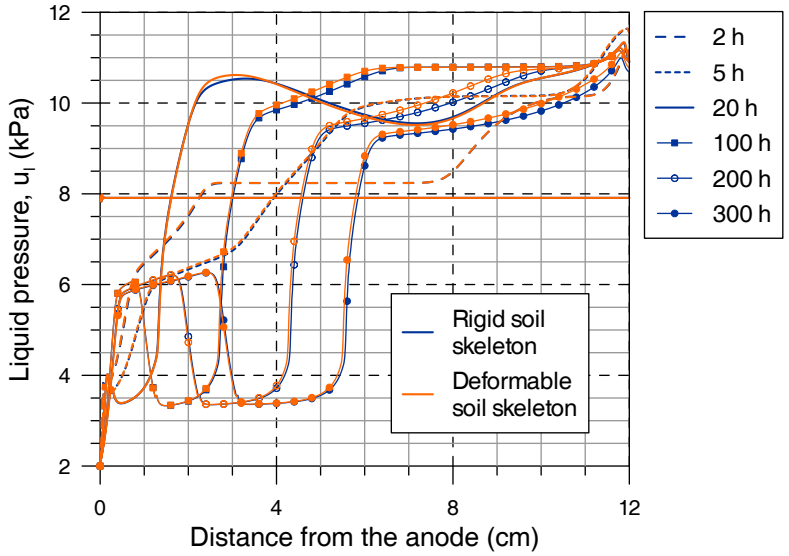

Figure 7.7: Numerical isochrones for pH and experimental data at test dismounting.

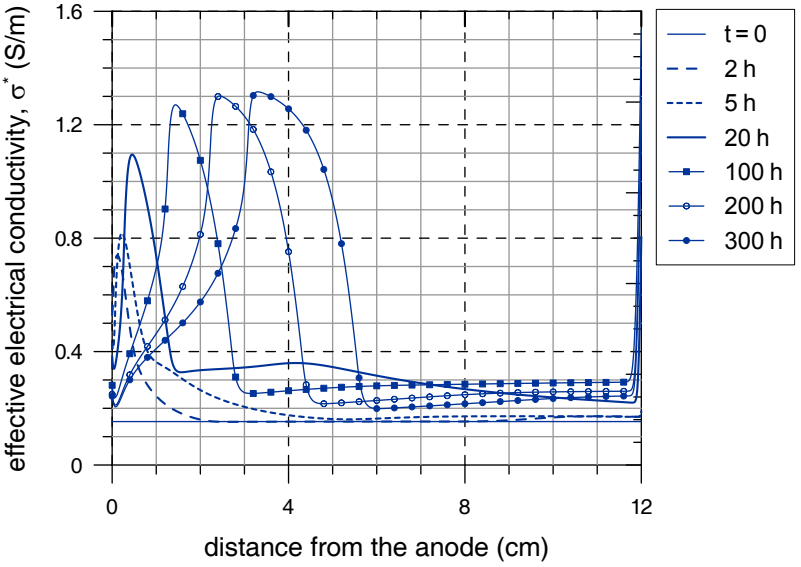

Figure 7.8: Isochrones for the apparent electrical conductivity: numerical predictions.

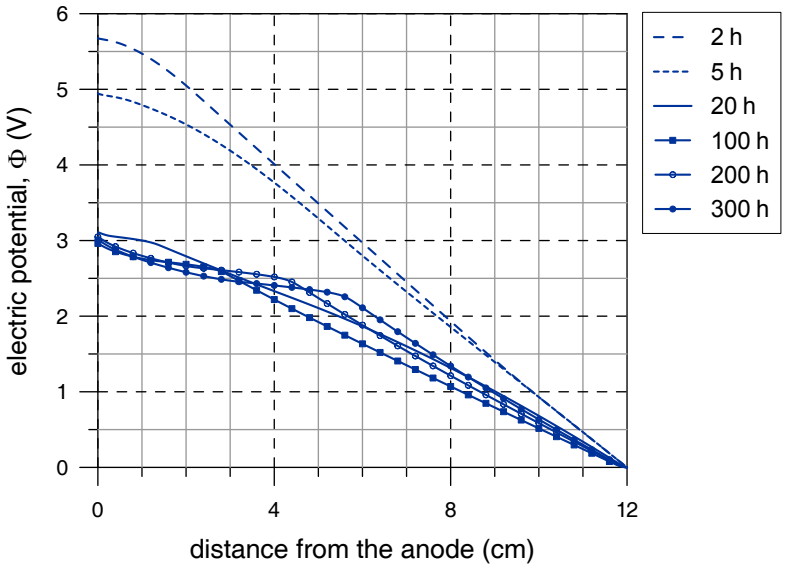

Figure 7.9: Isochrones for the electric potential, referred to the value at the cathode: numerical predictions.

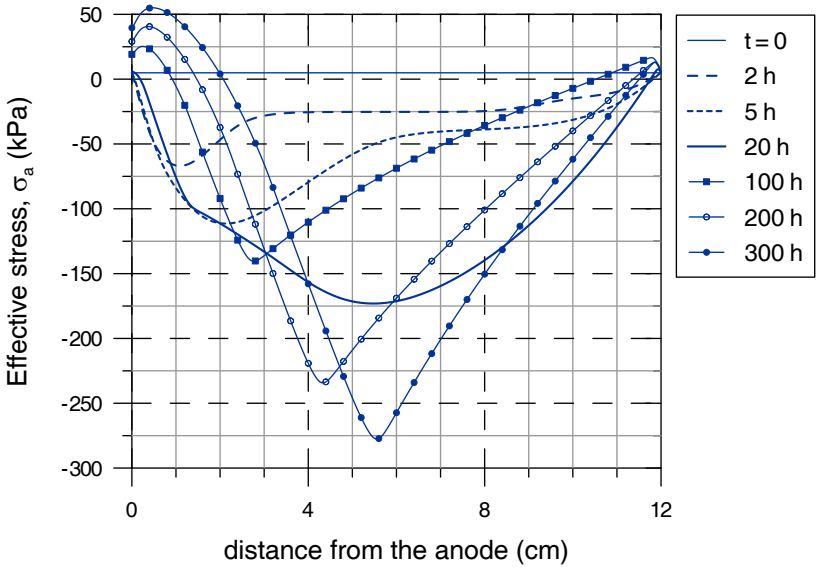

Figure 7.10: Effective stress: numerical predictions.

8

Conclusions

A numerical study on a natural clay subjected to electrokinetic treatment was presented. Scanzano clay is the natural clay adopted. The numerical study was performed using both numerical procedures outlined in Chapters 4-5 and the finite element method in Chapter 7.

A numerical procedure at the REV level for the integration of elastic–plastic hydro–mechanical constitutive laws for unsaturated soils along typical loading path was presented. This class of algorithm at the REV level are usually called constitutive drivers. At difference to previous works, the proposed driver allows for developing numerical integration routines for the constitutive equations, ready for their straightforward implementation in finite element codes.

An elastoplastic constitutive model for unsaturated soils was presented. Development of this model arises from the concepts established by Jommi (2000). The proposed model introduces few more parameters with respects to a classical model like Cam-Clay. Calibration of the model's parameters is mainly based on the results of standard laboratory tests. With respects to a standard Cam-Clay model the formulation proposed better matches the behaviour of overconsolidated clays and the behaviour in unsaturated conditions. The additional parameters for unsaturated states can be estimated from the results of oedometric tests at constant suction.

The constitutive model was implemented into the proposed numerical constitutive driver by means of an implicit algorithm. Numerical predictions were compared

to experimental results of a previous study performed by Rosone (2011). The proposed constitutive model catches pretty well experimental results. In particular the model can predict the values of the peak of the deviator stress of triaxial tests and the development of pore pressures.

A numerical procedure at the REV level for the integration of chemical reactions was presented. By means of this numerical procedure the importance of the carbonates system in the electrokinetic filtration tests performed by Gabrieli (2010) was confirmed. In fact calcite dissolution seems to be the main reason for the buffering capacity of Scanzano clay and for the desaturation process occurring during the experimental tests and observed at test dismounting. However the numerical results suggested that a description of the hydro-mechanical load and of transport processes are essential to reproduce void changes, hence the deformational response of the soil.

A finite element model for the electrokinetic problem was then presented. The finite element model confirms the theoretical guess and the results of the numerical procedure at the REV level. Carbonate equilibrium reactions have a definite impact on the overall behaviour in electrokinetic filtration tests. In particular the finite element model suggests that the observed desaturation process is mainly due to calcite dissolution in the acid environment. However the numerical results for pH and for the degree of saturation also suggest that other minerals than calcite might be responsible for the buffering capacity of Scanzano clay.

The role of the hydro-mechanical process was investigated. The description of hydro-mechanical behaviour has a definite impact on the results of the finite element model. In particular the onset of the observed fracture occurring at the anodic side can be predicted adopting a simple linear elastic behaviour of the solid phase.

The work presented herein is complemented by the following papers, in which some of the topics tackled are discussed in more details:

- Tamagnini, C., Jommi, C. and Cattaneo, F. (2010). A model for coupled electro-hydro-mechanical processes in fine grained soils accounting for gas generation and transport. *Anais da Academia Brasileira de Ciências*, 82(1):1-25.

- Cattaneo, F., Della Vecchia, G. and Jommi, C. (2011). A driver for the inte-

gration of coupled hydro-mechanical constitutive laws for unsaturated soils. In *Unsaturated Soils - Proceedings of 5th International Conference on Unsaturated Soils, Barcelona, Spain, 6-8 September*, Alonso and Gens editors, Taylor and Francis Group, London, pages 1017-1023.

- Jommi, C., Cattaneo, F. and Romero, E. (2008). Anisotropic deformational behaviour of collapsible compacted soils: experimental evidence and modelling. In *Deformational Characteristics of Geomaterials - Proceedings of 4th International Symposium on Deformation Characteristics of Geomaterials, Atlanta, Georgia, USA, 22-24 September*, Burns, Mayne and Santamarina editors, pages 605-612.

- Cattaneo, F., Della Vecchia, G. and Jommi, C. (2010). A note on integration algorithms for unsaturated soils constitutive models in the framework of elastoplasticity with generalised hardening. In *Numerical Methods in Geotechnical Engineering - Proceedings of 7th European Conference on Numerical Methods in Geotechnical Engineering (NUMGE 2010), Trondheim, Norway, 2-4 June*, Benz, T. and Nordal, S. editors, pages 319–324.

- Cattaneo, F., Jommi, C. and Musso, G.(2010). A numerical model for the electrokinetic treatment of natural soils with calcite. In *Numerical Methods in Geotechnical Engineering- Proceedings of 7th European Conference on Numerical Methods in Geotechnical Engineering (NUMGE 2010), Trondheim, Norway, 2-4 June*, Benz, T. and Nordal, S. editors, pages 275–280.

- Cattaneo, F. and Jommi, C. (2012). A note on the Newton-Raphson algorithm for FE analysis of electro-chemo-hydraulic problems in unsaturated soils. Submitted for the publication in the proceedings of the *2nd european conference on unsaturated soils (E-UNSAT 2012)*, 20-22 june, Napoli.

References

Aagaard, P. and Helgeson, H. C. (1982). Thermodynamic and kinetic constraints on reaction rates among minerals and aqueous solutions; I, theoretical considerations. *American Journal of Science*, 282(3):237–285. 81

Acar, Y. B. and Alshawabkeh, A. N. (1993). Principles of electrokinetic remediation. *Environmental Science Technology*, 27(13):2638–2647. 3, 7, 8, 13, 25

Acar, Y. B. and Alshawabkeh, A. N. (1996). Electrokinetic remediation. I: Pilot-scale tests with lead-spiked kaolinite. *Journal of Geotechnical Engineering*, 122(3):173–185. 8

Acar, Y. B., Alshawabkeh, A. N., and Gale, R. J. (1993). Fundamentals of extracting species from soils by electrokinetics. *Waste Management*, 13(2):141–151. 24

Airoldi, F., Jommi, C., Musso, G., and Paglino, E. (2009). Influence of calcite on the electrokinetic treatment of a natural clay. *Journal of Applied Electrochemistry*, 39(11):2227–2237. 133

Airò Farulla, C., Battiato, A., and Ferrari, A. (2011). The void ratio dependency of the retention behaviour for a compacted clay. In *Unsaturated Soils*, Alondo, E. E. and Gens, A. S., editors, volume 1. Taylor & Francis Group, London. 42, 86

Airò Farulla, C., Ferrari, A., and Romero, E. (2007). Hydro-mechanical behaviour of compacted scaly clay during controlled-suction testing. In *2nd International Conference on Mechanics of Unsaturated Soils, Weimar, Germany, Mar 7-9*, Schanz, T., editor, pages 345–354. Springer-Verlag, Berlin. 86

Airò Farulla, C. and Jommi, C. (2005). Suction controlled wetting–drying cycles on a compacted scaly clay. In *Proceedings on Internation Conference on Problematic Soils GEOPROB 2005, Famagusta*, Bilsel, H. and Nalbantoglu, Z., editors, volume 1, pages 229–237. Eastern Mediterranean University Press. 86

Alshawabkeh, A. N. (2001). Basics and applications of electrokinetic remediation. Handouts Prepared for a Short Course at the Federal University of Rio de Janeiro, 19-20 November 2001. 45

Alshawabkeh, A. N. and Acar, Y. B. (1996). Electrokinetic remediation. II: Theoretical model. *Journal of Geotechnical Engineering*, 122(3):186–196. 32

Alshawabkeh, A. N., Yeung, A. T., and Bricka, M. R. (1999). Practical aspects of in-situ electrokinetic extraction. *J. Environ. Eng.*, 125(1):27–35. 25

Appelo, C. A. J. and Postma, D. (2005). *Geochemistry, Groundwater and pollution, second Edition*. Balkema, Rotterdam. 14

Atkins, P. (1982). *Physical Chemistry*. Oxford University Press. 33

Banerjee, P. K. and Stipho, A. S. (1979). An elasto-plastic model for undrained behaviour of heavily overconsolidated clays. *International Journal for Numerical and Analytical Methods in Geomechanics*, 3(1):97–103. 110

Bardet, J. P. and Choucair, W. (1991). A linearized integration technique for incremental constitutive equations. *International Journal for Numerical and Analytical Methods in Geomechanics*, 15(1):1–19. 56, 57

Bear, J. (1972). *Dynamics of Fluids in Porous Media*. Dover, New York. 43, 44

Bear, J. and Cheng, A. H. D. (2010). *Modeling Groundwater Flow and Contaminant Transport*. Springer. 3, 42

Bethke, C. M. (1996). *Geochemical Reaction Modeling: Concepts and Applications*. Oxford University Press, New York. 46

Bigoni, D. and Piccolroaz, A. (2004). Yield criteria for quasibrittle and frictional materials. *International Journal of Solids and Structures*, 41(11-12):2855–2878. 110, 111

Bishop, A. W. and Wesley, L. D. (1975). A hydraulic triaxial apparatus for controlled stress path testing. *Géotechnique*, 25(4):657–670. 89

Bjerrum, L., Moum, J., and Eide, O. (1967). Application of electro-osmosis to a foundation problem in a norwegian quick clay. *Géotechnique*, 17:214–235. 16

Borja, R. I. (1991). Cam-clay plasticity, part II: Implicit integration of constitutive equation based on a nonlinear elastic stress predictor. *Computer Methods in Applied Mechanics and Engineering*, 88(2):225–240. 51

Borja, R. I. (2004). Cam-clay plasticity. part V: A mathematical framework for three-phase deformation and strain localization analyses of partially saturated porous media. *Computer Methods in Applied Mechanics and Engineering*, 193(48-51):5301–5338. 61

Borja, R. I. and Lee, S. R. (1990). Cam-clay plasticity, part I: Implicit integration of elasto-plastic constitutive relations. *Computer Methods in Applied Mechanics and Engineering*, 78(1):49–72. 57, 61, 67

Borja, R. I., Tamagnini, C., and Amorosi, A. (1997). Coupling plasticity and energy-conserving elasticity models for clays. *Journal of Geotechnical and Geoenvironmental Engineering*, 123(10):948–957. 51

Brooks, A. N. and Corey, A. T. (1966). Properties of porous media affecting fluid flow. *Journal of Irrigation and Drainage Division, ASCE*, 92:61–87. 44

Bruell, C. J., Segall, B. A., and Walsh, M. T. (1992). Electroosomotic removal of gasoline hydrocarbons and tce from clay. *Journal of Environmental Engineering*, 118(1):68–83. 23

Buijs, P., Van Diemen, A., and Stein, H. (1994). Efficient dewatering of water-works sludge by electroosmosis. *Colloids and Surfaces A: Physicochemical and Engineering Aspects*, 85(1):29–36. 8

Calabresi, G., Pane, V., Rampello, S., and Tamagnini, C. (1992). A proposal to evaluate the effectiveness of soft consolidation techniques for the permanent stabilisation of the tower of Pisa. Technical report, Università di Roma La Sapienza, DISG. 16

Casagrande, L. (1949). Electro-osmosis in soils. *Géotechnique*, 1(3):159–177. 16, 30

Casagrande, L., Wade, N., Wakely, M., and Loughney, R. (1981). Electro-osmosis projects, British Columbia, Canada. In *Proceedings of the Tenth International Conference on Soil Mechanics and Foundation Engineering, Stockholm 15–19 June*, volume 3. Balkema, Rotterdam. 16

Chappel, B. A. and Burton, P. L. (1975). Electro-osmosis applied to unstable embankment. *Journal of the geotechnical Engineering division, ASCE*, 108(GT8):733–740. 16

Davis, J. A. and Kent, D. B. (1990). Surface complexation modeling in aqueous geochemistry. In *Mineral-Water Interface Geochemistry*, Hochella, M. F. and White, A. F., editors, volume 23, pages 177–260. 46

de Wet, M. (1995). Electro-kinetics, infiltration and unsaturated flow. In *Unsaturated Soils*, Alonso, E. and Delage, P., editors, volume 1, pages 283–291. A.A. Balkema, Rotterdam.

Esrig, M. I. (1968). Pore pressures, consolidation and electrokinetics. *Journal of the soil mechanics and foundations division ASCE*, 94(SM4):899–921. 7, 16, 17, 132

Fetzer, C. A. (1967). Electro-osmosis stabilization of West Branch dam. *Journal of the Soil Mechanics and Foundation Division, ASCE*, 93(SM4):85–106. 16

Finzi, D. and Veder, C. (1962). Stabilizzazione di una frana mediante infissione di elettrodi nel piano di scivolamento. *Rivista italiana di geotecnica*, 5:2–8. 16

Gabrieli, L. (2010). *Complicating Features of Electrokinetic Treatments In Natural Soils*. PhD thesis, Politecnico di Torino. 96, 140

Gabrieli, L., Jommi, C., Musso, G., and Romero, E. (2008a). Electrokinetic treatment of a natural silt in saturated and unsaturated conditions. In *Thermo-Hydromechanical and Chemical coupling in Geomaterials and Applications: Proceedings of the 3rd International Symposium GeoProc 2008*, Shao, J.-F. and Burlion, N., editors, London. Wiley. 20, 22

Gabrieli, L., Jommi, C., Musso, G., and Romero, E. (2008b). Influence of electroosmotic treatment on the hydro-mechanical behaviour of clayey silts: preliminary experimental results. *Journal of Applied Electrochemistry*, 38(7):1043–1051. 14, 20, 130

Gallipoli, D., Gens, A., Sharma, R., and Vaunat, J. (2003a). An elasto-plastic model for unsaturated soil incorporating the effects of suction and degree of saturation on mechanical behaviour. *Géotechnique*, 53(1):123–136. 51, 111

Gallipoli, D., Wheeler, S. J., and Karstunen, M. (2003b). Modelling the variation of degree of saturation in a deformable unsaturated soil. *Géotechnique*, 53(1):105–112. 42, 45, 57

Gent, D. B., Bricka, R. M., Alshawabkeh, A. N., Larson, S. L., Fabian, G., and Granade, S. (2004). Bench- and field-scale evaluation of chromium and cadmium extraction by electrokinetics. *Journal of Hazardous Materials*, 110(1-3):53–62. 8

Hamir, R. B., Jones, C. J. F. P., and Clarke, B. G. (2001). Electrically conductive geosynthetics for consolidation and reinforced soil. *Geotextiles and Geomembranes*, 19(8):455–482. 16

Hansen, H. K., Ottosen, L. M., Kliem, B. K., and Villumsen, A. (1997). Electrodialytic remediation of soils polluted with Cu, Cr, Hg, Pb and Zn. *J. Chem. Technol. Biotechnol.*, 70(1):67–73. 8

Helmholtz, H. (1879). Studien über elektrische Grenzschiehten. *Wiedemanns Annalen d. Physik.*, 7:137. 10

Ho, S. V., Athmer, C., Sheridan, P. W., Hughes, B. M., Orth, R., McKenzie, D., Brodsky, P. H., Shapiro, A., Thornton, R., Salvo, J., Schultz, D., Landis, R., Griffith, R., and Shoemaker, S. (1999a). The lasagna technology for in situ soil remediation. 1. small field test. *Environmental Science & Technology*, 33(7):1086–1091. 8

Ho, S. V., Athmer, C., Sheridan, P. W., Hughes, B. M., Orth, R., McKenzie, D., Brodsky, P. H., Shapiro, A. M., Sivavec, T. M., Salvo, J., Schultz, D., Landis, R., Griffith, R., and Shoemaker, S. (1999b). The lasagna technology for in situ soil

remediation. 2. large field test. *Environmental Science & Technology*, 33(7):1092–1099. 8

Hundsdorfer, W. and Verwer, J. (1995). A note on splitting errors for advection-reaction equations. *Applied Numerical Mathematics*, 18(1-3):191–199. 124

Hvorslev, M. J. (1960). Physical components of the shear strength of saturated clays. In *Proceedings ASCE Research Conference on the Shear Strength of Cohesive Soils*, pages 169–273, Boulder, CO. 110

Jakobsen, K. P. and Lade, P. V. (2002). Implementation algorithm for a single hardening constitutive model for frictional materials. *International Journal for Numerical and Analytical Methods in Geomechanics*, 26(7):661–681. 61, 66

Jommi, C. (2000). Remarks on the constitutive modelling of unsaturated soils. In *Experimental evidence and theoretical approaches in unsaturated soils*, Tarantino, A. and Mancuso, C., editors, pages 139–153. Balkema, Rotterdam. 50, 57, 139

Jommi, C. and di Prisco, C. (1994). Un semplice approccio teorico per la modellazione del comportamento meccanico di terreni granulari parzialmente saturi (in italian). In *Il ruolo dei fluidi nei problemi di ingegneria geotecnica*, pages 167–188, Mondovì, Italy. 51, 109

Jones, C. J. F. P., Glendinning, S., Huntley, D. T., and Lamont-Black, J. (2006). Soil consolidation and strengthening using electrokinetic geosynthetics - concept and analysis. In *Proceedings of the 8th International Conference on Geosynthetics (8ICG), Yokohama, Japan, 18–22 Semptember*, Kuwano, J. and Koseki, J., editors. Milpress, Rotterdam. 16

Kawai, K., Kato, S., and Karube, D. (2000). The model of water retention curve considering effects of void ratio. In *Unsaturated Soils for Asia, proc. 1st asian conf. on unsaturated soils*, Rahardjo, H., Toll, D. T. G., and Leong, E. C., editors, pages 329–334. 42

Kim, S. O., Moon, S. H., and Kim, K. W. (2000). Enhanced electrokinetic soil remediation for removal of organic contaminants. *Environmental Technology*, 21(4):417–426. 8

Kirkner, D. J. and Reeves, H. (1988). Multicomponent mass transport with homogeneous and heterogeneous chemical reactions: Effect of the chemistry on the choice of numerical algorithm 1. Theory. *Water Resources Research*, 24(10):1719–1729. 46

Kohgo, Y. (2008). A hysteresis model of soil water retention curves based on bounding surface concept. *Soils and Foundations*, 48(5):633–640. 43

Lade, P. and Kim, M. (1988). Single hardening constitutive model for frictional materials ii. yield critirion and plastic work contours. *Computers and Geotechnics*, 6(1):13–29. 110

Lageman, R. (1993). Electroreclamation. applications in the netherlands. *Environmental Science & Technology*, 27(13):2648–2650. 8

Lageman, R., Pool, W., and Seffinga, G. (1989a). Electro-reclamation: theory and practice. *Chemistry and Industry*, 18:585–590. 3, 8

Lageman, R., Pool, W., and Seffinga, G. (1989b). Theory and practice of electro-osmosis. In *Forum on Innovative Hazardous Waste Treatment Technologies: Domestic and International. Atlanta, Georgia, 19–21 June.*, pages 57–76. EPA Report EPA/540/2-89/056. 22

Langmuir, D. (1997). *Aqueous Environmental Geochemistry*. Prentice-Hall, Inc., Upper Saddle River, NJ. 46

Lasaga, A. C. (1981). Rate laws of chemical reactions. In Lasaga, A. C. and Kirkpatrick, R. J., editors, *Reviews in Mineralogy*, volume 8, chapter 1, pages 1–68. Mineralogical Society of America. 80

Lasaga, A. C. (1984). Chemical kinetics of water-rock interactions. *J. Geophys. Res.*, 89(B6):4009–4025. 80, 81

Li, A., Cheung, K. A., and Reddy, K. R. (2000). Cosolvent-enhanced electrokinetic remediation of soils contaminated with phenanthrene. *J. Environ. Eng.*, 126(6):527–533. 8

Li, Y.-H. and Gregory, S. (1974). Diffusion of ions in sea water and in deep-sea sediments. *Geochimica et Cosmochimica Acta*, 38(5):703–714. 32

Lichtner, P. C. (1985). Continuum model for simultaneous chemical reactions and mass transport in hydrothermal systems. *Geochimica et Cosmochimica Acta*, 49(3):779–800. 46

Lomizé, G. M., Netushil, A. V., and Rzhanitzin, B. A. (1957). Electro-osmosis processes in clayey soils and dewatering during excavation. In *Proceedings of the Fourth International Conference on Soil Mechanics and Foundation Egineering, London 12–24 August*, volume 1. Buttherworths Scientific Publications, London. 16

Mascia, M., Palmas, S., Polcaro, A. M., Vacca, A., and Muntoni, A. (2007). Experimental study and mathematical model on remediation of Cd spiked kaolinite by electrokinetics. *Electrochimica Acta*, 52(10):3360–3365. 8

Mayer, K. U., Frind, E. O., and Blowes, D. W. (2002). Multicomponent reactive transport modeling in variably saturated porous media using a generalized formulation for kinetically controlled reactions. *Water Resources Research*, 38(9):1174–. 80

Miller, G. A., Khoury, C. N., Muraleetharan, K. K., Liu, C., and Kibbey, T. C. G. (2008). Effects of soil skeleton deformations on hysteretic soil water characteristic curves: Experiments and simulations. *Water Resources Research*, 44:W00C06–. 43

Mitchell, J. K. and Soga, K. (2005). *Fundamentals of soil behavior*. Wiley, 3rd edition. 9, 10, 11, 15, 27, 29

Molins, S., Carrera, J., Ayora, C., and Saaltink, M. W. (2004). A formulation for decoupling components in reactive transport problems. *Water Resources Research*, 40(10):W10301–. 77, 125

Morel, F. M. M. and Hering, J. G. (1993). *Principles and Applications of Aquatic Chemistry*. John Wiley. 80

Morris, D. V., Hillis, S., and Caldwell, J. A. (1985). Improvement of sensitive clay by electroosmosis. *Canadian Geotechnical Journal*, 22:17–24. 7

Musso, G. (2000). *Electrokinetic phenomena in soils*. PhD thesis, Politecnico di Torino. 96

Narasimhan, B. and Sri Ranjan, R. (2000). Electrokinetic barrier to prevent subsurface contaminant migration: theoretical model development and validation. *Journal of Contaminant Hydrology*, 42(1):1–17. 22

Ng, C. W. W. and Pang, Y. W. (2000). Influence of stress state on soil-water characteristics and slope stability. *Journal of Geotechnical and Geoenvironmental Engineering*, 126(2):157–166. 42

Nuth, M. and Laloui, L. (2008). Advances in modelling hysteretic water retention curve in deformable soils. *Computers and Geotechnics*, 35(6):835–844. 43, 45, 57, 111

Onsager, L. (1931). Reciprocal relations in irreversible processes. I. *Phys. Rev.*, 37(4):405–. 29

Ortiz, M. and Popov, E. P. (1985). Accuracy and stability of integration algorithms for elastoplastic constitutive relations. *International Journal for Numerical Methods in Engineering*, 21(9):1561–1576. 61

Pamukcu, S. and Wittle, K. J. (1992). Electrokinetic removal of selected heavy metals from soil. *Environmental Progress*, 11(3):241–250. 3

Quarteroni, A., Sacco, R., and Saleri, F. (2007). *Numerical Mathematics*. Springer, second edition. 59, 63

Raats, M. H. M., van Diemen, A. J. G., Lavèn, J., and Stein, H. N. (2002). Full scale electrokinetic dewatering of waste sludge. *Colloids and Surfaces A: Physicochemical and Engineering Aspects*, 210(2-3):231–241. 8

Reddy, K. R., Adams, J. A., and Richardson, C. (1999). Potential technologies for remediation of brownfields. *Practice Periodical of Hazardous, Toxic, and Radioactive Waste Management*, 3(2):61–68. 3, 4

Reddy, K. R. and Parupudi, U. S. (1997). Removal of chromium, nickel and cadmium from clays by *in-situ* electrokinetic remediation. *Journal of Soil Contamination*, 6(4):391–407. 23, 24

Reuss, F. F. (1809). Sur un nouvel effet de l'électricité galvanique. *Mémoires de la Société Impériale des Naturalistes de Moscou*, 2:327–337. 7

Rittirong, A., Shang, J. Q., Mohamedelhassan, E., Ismail, M. A., and Randolph, M. F. (2008). Effects of electrode configuration on electrokinetic stabilization for caisson anchors in calcareous sand. *Journal of Geotechnical and Geoenvironmental Engineering*, 134(3):352–365. 16

Robinson, B. A., Viswanathan, H. S., and Valocchi, A. J. (2000). Efficient numerical techniques for modeling multicomponent ground-water transport based upon simultaneous solution of strongly coupled subsets of chemical components. *Advances in Water Resources*, 23(4):307–324. 125

Romero, E., , Gens, A., and Lloret, A. (1999). Experimental aspects and interpretation of suction controlled swelling pressure tests. In *XI Panamerican Conference on Soil Mechanics and Geotechnical Engineering. 08-12 August 1999, Foz do Iguassu, Brazil. Associacao Brasileira de Mecanica dos Solos e Engenharia Geotécnica*, pages 292–935. 44

Romero, E., Della Vecchia, G., and Jommi, C. (2011). An insight into the water retention properties of compacted clayey soils. *Géotechnique*, 61(4):313–328. 45, 57

Romero, E. and Jommi, C. (2008). An insight into the role of hydraulic history on the volume changes of anisotropic clayey soils. *Water Resources Research*, 44:–. 51, 109

Roscoe, K. H. and Burland, J. B. (1968). On the generalized stress- strain behaviour of wet clay. In *Engineering Plasticity*, Heyman, J. and Leckie, F. A., editors, pages 535–609. Cambridge University Press, Cambridge, England. 110, 115

Rosone, M. (2011). *Resistenza a taglio di un'argilla a scaglie compattata non satura*. PhD thesis, Università degli studi *Mediterranea* di Reggio Calabria. 90, 140

Saaltink, M., Battle, F., Ayora, C., Carrera, J., and Olivella, S. (2004). Retraso, a code for modeling reactive transport in saturated and unsaturated porous media. *Geologica Acta*, 2(3):235–251. 80, 124

Saaltink, M. W., Ayora, C., and Carrera, J. (1998). A mathematical formulation for reactive transport that eliminates mineral concentrations. *Water Resources Research*, 34(7):1649–1656. 77, 78, 80

Saaltink, M. W., Carrera, J., and Ayora, C. (2001). On the behavior of approaches to simulate reactive transport. *Journal of Contaminant Hydrology*, 48(3-4):213–235. 124

Shackelford, C. D. and Daniel, D. E. (1991). Diffusion in saturated soil. I: Background. *Journal of Geotechnical Engineering*, 117(3):467–484. 32

Shackelford, C. D. and Jefferis, S. A. (2000). Geoenvironmental engineering for in situ remediation. In *GeoEng 2000, International Conference on Geotechnical and Geological Engineering, Melbourne, Australia, Nov. 19–24*, volume 1, pages 126–185. Technomic Publ, Lancaster, PA, USA. 1, 2, 3, 4

Shapiro, A. P. and Probstein, R. F. (1993). Removal of contaminants from saturated clay by electroosmosis. *Environmental Science Technology*, 27(2):283–291. 3

Simo, J. C. and Taylor, R. L. (1985). Consistent tangent operators for rate-independent elastoplasticity. *Computer Methods in Applied Mechanics and Engineering*, 48(1):101–118. 60

Sloan, S. W. (1987). Substepping schemes for the numerical integration of elastoplastic stress-strain relations. *International Journal for Numerical Methods in Engineering*, 24(5):893–911. 57, 61, 66

Sloan, S. W., Abbo, A. J., and Sheng, D. (2001). Refined explicit integration of elastoplastic models with automatic error controls. *Engineering Computations*, 18(1/2):121–194. 61, 64, 67

Smoluchowski, M. (1914). Elektrische endosmose und strömungstruöme. In *Handbuch der Elektrizität und des Magnetismus*, Graetz, L., editor, volume 2, page 366. J. A. Barth, Leipzig. 10

Steefel, C. I. and MacQuarrie, K. T. B. (1996). Approaches to modeling of reactive transport in porous media. *Reviews in Mineralogy and Geochemistry*, 34(1):85–129. 80, 81, 124, 126

Stoer, J. and Bulirsch, R. (2002). *Introduction to Numerical Analysis*. Springer, third edition. 66

Strang, G. (1968). On the construction and comparison of difference schemes. *SIAM Journal on Numerical Analysis*, 5(3):506–517. 126

Stumm, W. and Morgan, J. J. (1995). *Aquatic Chemistry: Chemical Equilibria and Rates in Natural Waters*. John Wiley and Sons, New York. 46

Su, J. Q. and Wang, Z. (2003). The two-dimensional consolidation theory of electro-osmosis. *Géotechnique*, 53(8):759–763. 17

Talesnick, M. and Frydman, S. (1990). The preparation of hollow cylinder specimens from undisturbed tube samples of soft clay. *Geotechnical Testing Journal*, 13(3):243–249. 8

Tamagnini, C., Castellanza, R., and Nova, R. (2002). A generalized backward euler algorithm for the numerical integration of an isotropic hardening elastoplastic model for mechanical and chemical degradation of bonded geomaterials. *International Journal for Numerical and Analytical Methods in Geomechanics*, 26(10):963–1004. 51, 61, 67

Tamagnini, C., Jommi, C., and Cattaneo, F. (2010). A model for coupled electro-hydro-mechanical processes in fine grained soils accounting for gas generation and transport. *Anais da Academia Brasileira de Ciências*, 82:169–193. 20

Tamagnini, R. (2004). An extended cam-clay model for unsaturated soils with hydraulic hysteresis. *Géotechnique*, 54(3):223–228. 51, 110

Tarantino, A. and Tombolato, S. (2005). Coupling of hydraulic and mechanical behaviour in unsaturated compacted clay. *Géotechnique*, 55(4):307–317. 42

Topp, G. C. (1971). Soil water hysteresis in silt loam and clay loam soils. *Water Resources Research*, 7(4):914–920. 43

van Genuchten, M. T. (1980). A closed-form equation for predicting the hydraulic conductivity of unsaturated soils. *Soil Sci Soc Am J*, 44(5):892–898. 44, 87

Vanapalli, S. K., Fredlund, D. G., and Pufahl, D. E. (1999). The influence of soil structure and stress history on the soil-water characteristics of a compacted till. *Géotechnique*, 49(2):143–159. 44

Vanuat, J., Gens, A., and Jommi, C. (1997). A strategy for numerical analysis of the transition between saturated and unsaturated flow conditions. In *Numerical Models in Geomechanics - NUMOG VI*, Pietruszczak, P., editor, pages 297–302. Balkema. 40, 60

Viggiani, C. and Squeglia, N. (2003). Electro-osmosis to stabilise the leaning tower of Pisa. *Rivista Italiana di Geotecnica*, 1:29–37. 16

Virkutyte, J., Sillanpää, M., and Latostenmaa, P. (2002). Electrokinetic soil remediation – critical overview. *The Science of The Total Environment*, 289(1-3):97–121. 1

Wan, T.-Y. and Mitchell, J. K. (1976). Electro-osmosis consolidation of soils. *Journal of the geotechnical Engineering division, ASCE*, 102(GT5):473–491. 7, 17, 19

Wieczorek, S., Weigand, H., Schmid, M., and Marb, C. (2005). Electrokinetic remediation of an electroplating site: design and scale-up for an in-situ application in the unsaturated zone. *Engineering Geology*, 77(3-4):203–215. 8

Yeh, G. T. and Tripathi, V. S. (1989). A critical evaluation of recent developments in hydrogeochemical transport models of reactive multichemical components. *Water Resources Research*, 25(1):93–108. 46, 124

Yeung, A. T. (1994). Electrokinetic flow processes in porous media and their applications. In Corapcioglu, M. Y., editor, *Advances in porous media*, volume 2, pages 309–396. Elsevier Science. 9

Yeung, A. T. and Mitchell, J. K. (1993). Coupled fluid, electrical and chemical flows in soil. *Géotechnique*, 43(1):121–134. 22, 28

Yuan, C. and Weng, C.-h. (2003). Sludge dewatering by electrokinetic technique: effect of processing time and potential gradient. *Advances in Environmental Research*, 7(3):727–732. 8

A

Derivatives of the driver governing equations

- $\dfrac{\partial \Delta \sigma_{ij}}{\partial \Delta \varepsilon_{hk}}$

From definition of the total stress increment (Eq. 4.5)

$$\frac{\partial \Delta \sigma_{ij}}{\partial \Delta \varepsilon_{hk}} = \frac{\partial \Delta \hat{\sigma}_{ij}}{\partial \Delta \varepsilon_{hk}} + (u_l^{n+1} - u_g^{n+1})\delta_{ij}\frac{\partial Sr^{n+1}}{\partial \Delta \varepsilon_{hk}} \tag{A.1}$$

since $\hat{\sigma}_{ij}^{n+1} := \hat{\sigma}_{ij}^{n} + \Delta\hat{\sigma}_{ij}$ it follows that

$$\frac{\partial \hat{\sigma}_{ij}}{\partial \Delta \varepsilon_{hk}} = \frac{\partial \Delta \hat{\sigma}_{ij}}{\partial \Delta \varepsilon_{hk}} + \frac{\partial \Delta \hat{\sigma}_{ij}}{\partial \Delta Sr}\frac{\partial \Delta Sr}{\partial \Delta \varepsilon_{hk}} \tag{A.2}$$

the first term on the RHS is the tangent consistent modulus. So the derivative of the total stress increment respect to strain increment is:

$$\frac{\partial \Delta \sigma_{ij}}{\partial \Delta \varepsilon_{hk}} = \frac{\partial \Delta \hat{\sigma}_{ij}}{\partial \Delta \varepsilon_{hk}} + \left((u_l^{n+1} - u_g^{n+1})\delta_{ij} + \frac{\partial \Delta \hat{\sigma}_{ij}}{\partial \Delta Sr}\right)\frac{\partial \Delta Sr}{\partial \Delta \varepsilon_{hk}} \tag{A.3}$$

- $\dfrac{\partial \Delta \sigma_{ij}}{\partial \Delta u_l}$

From definition of the total stress increment (Eq. 4.5), taking into account

that $u_l^{n+1} = u_l^n + \Delta u_l$:

$$\frac{\partial \Delta \sigma_{ij}}{\partial \Delta u_l} = \left((u_g^{n+1} - u_l^{n+1}) \frac{\partial Sr^{n+1}}{\partial \Delta u_l} + Sr^{n+1} \right) \delta_{ij} + \frac{\partial \Delta \hat{\sigma}_{ij}}{\partial \Delta Sr} \frac{\partial \Delta Sr}{\partial \Delta u_l} \tag{A.4}$$

the derivative of the final degree of saturation could be wrote in terms of increments:

$$\frac{\partial Sr^{n+1}}{\partial \Delta u_l} = \frac{\partial (Sr^n + \Delta Sr)}{\partial \Delta u_l} = \frac{\partial \Delta Sr}{\partial \Delta u_l} \tag{A.5}$$

Usually retention curve is wrote as a function of suction s, from the definition of suction $s := u_g - u_l$:

$$\frac{\partial \Delta Sr}{\partial \Delta u_l} = -\frac{\partial \Delta Sr}{\partial \Delta s} \tag{A.6}$$

so the derivative of total stress increment to the liquid pressure is:

$$\frac{\partial \Delta \sigma_{ij}}{\partial \Delta u_l} = \left(-(u_g^{n+1} - u_l^{n+1}) \frac{\partial \Delta Sr}{\partial \Delta s} + Sr^{n+1} \right) \delta_{ij} - \frac{\partial \Delta \hat{\sigma}_{ij}}{\partial \Delta Sr} \frac{\partial \Delta Sr}{\partial \Delta s} \tag{A.7}$$

- $\dfrac{\partial \Delta \sigma_{ij}}{\partial \Delta u_g}$

  For the same consideration took into account in the development of the derivative of the total stress increment respect to the liquid pressure, the derivative of the total stress increment respect to the gas pressure is:

$$\frac{\partial \Delta \sigma_{ij}}{\partial \Delta u_g} = \left((u_l^{n+1} - u_g^{n+1}) \frac{\partial \Delta Sr}{\partial \Delta s} - Sr^{n+1} \right) \delta_{ij} + \frac{\partial \Delta \hat{\sigma}_{ij}}{\partial \Delta Sr} \frac{\partial \Delta Sr}{\partial \Delta s} \tag{A.8}$$

- $\dfrac{\partial \Delta m_w}{\partial \Delta \varepsilon_{hk}}$

  From Equation (4.8)

$$\frac{\partial \Delta m_w}{\partial \Delta \varepsilon_{hk}} = \frac{\partial n^{n+1}}{\partial \Delta \varepsilon_{hk}} Sr^{n+1} \rho_w^{n+1} + n^{n+1} \frac{\partial \Delta Sr}{\partial \Delta \varepsilon_{hk}} \rho_w^{n+1} \tag{A.9}$$

Void ratio at increment $n+1$ is

$$e^{n+1} = e^n - (1 - e^n) \Delta \varepsilon_{vol} \tag{A.10}$$

taking into account the relation between porosity and void ratio, the derivative of porosity respect to strain increment is

$$\frac{\partial n^{n+1}}{\partial \Delta \varepsilon_{hk}} = -\frac{1}{(1+e^n)(1-\Delta \varepsilon_{vol})^2}\delta_{hk} \tag{A.11}$$

- $\frac{\partial \Delta m_w}{\partial \Delta u_l}$

$$\frac{\partial \Delta m_w}{\partial \Delta u_l} = n^{n+1}\left(\frac{\partial \Delta Sr}{\partial \Delta u_l}\rho_w^{n+1} + Sr^{n+1}\frac{\partial \rho_w^{n+1}}{\partial \Delta u_l}\right) \tag{A.12}$$

From Equation (4.9)

$$\frac{\partial \rho_w^{n+1}}{\partial \Delta u_l} = \rho_w^0 \exp\frac{u_l^{n+1}-u_l^0}{B_w}\frac{1}{B_w} = \frac{\rho_w^{n+1}}{B_w} \tag{A.13}$$

Substituting Equation (A.13) into Equation (A.12), finally

$$\frac{\partial \Delta m_w}{\partial \Delta u_l} = n^{n+1}\rho_w^{n+1}\left(\frac{Sr^{n+1}}{B_w} - \frac{\partial \Delta Sr}{\partial \Delta s}\right) \tag{A.14}$$

- $\frac{\partial \Delta m_w}{\partial \Delta u_g}$

$$\frac{\partial \Delta m_w}{\partial \Delta u_g} = n^{n+1}\frac{\partial \Delta Sr}{\partial \Delta u_g}\rho_w^{n+1} = n^{n+1}\frac{\partial \Delta Sr}{\partial \Delta s}\rho_w^{n+1} \tag{A.15}$$

- $\frac{\partial \Delta m_a}{\partial \Delta \varepsilon_{hk}}$

$$\frac{\partial \Delta m_a}{\partial \Delta \varepsilon_{hk}} = -(1-h)\frac{\partial \Delta Sr}{\partial \Delta s}\rho_a^{n+1} + (1-(1-h)Sr^{n+1})\frac{\partial n^{n+1}}{\partial \Delta \varepsilon_{hk}}\rho_a^{n+1} \tag{A.16}$$

- $\frac{\partial \Delta m_a}{\partial \Delta u_l}$

$$\frac{\partial \Delta m_a}{\partial \Delta u_l} = (1-h)\frac{\partial \Delta Sr}{\partial \Delta s}n^{n+1}\rho_a^{n+1} \tag{A.17}$$

- $\dfrac{\partial \Delta m_a}{\partial \Delta u_g}$

$$\frac{\partial \Delta m_a}{\partial \Delta u_g} = -(1-h)\frac{\partial \Delta Sr}{\partial \Delta u_g} n^{n+1} \rho_a^{n+1} + (1-(1-h)Sr^{n+1}) n^{n+1} \frac{\partial \rho_a^{n+1}}{\partial \Delta u_g} \tag{A.18}$$

Air density depends from gas pressure (Eq. (4.13)):

$$\rho_a^{n+1} = \rho_a^0 \frac{u_g^{n+1} + p_{atm}}{u_g^0 + p_{atm}} \quad \Rightarrow \quad \frac{\partial \rho_a^{n+1}}{\partial \Delta u_g} = \frac{\rho_a^0}{u_g^0 + p_{atm}} \tag{A.19}$$

Substituting Equation (A.19) the derivative of air mass respect to gas pressure increment becomes:

$$\frac{\partial \Delta m_a}{\partial \Delta u_g} = -(1-h)\frac{\partial \Delta Sr}{\partial \Delta s} n^{n+1} \rho_a^{n+1} + (1-(1-h)Sr^{n+1}) n^{n+1} \frac{\rho_a^0}{u_g^0 + p_{atm}} \tag{A.20}$$